2020

BIMETALLIC NANOPARTICLES INTEGRATED MEMBRANES FOR GROUNDWATER REMEDIATION: SYNTHESIS, CHARACTERIZATION AND APPLICATIONS

Hongyi Wan
University of Kentucky, hongyi.wan@uky.edu
Digital Object Identifier: https://doi.org/10.13023/etd.2020.065

STUDENT AGREEMENT:

I represent that my thesis or dissertation and abstract are my original work. Proper attribution has been given to all outside sources. I understand that I am solely responsible for obtaining any needed copyright permissions. I have obtained needed written permission statement(s) from the owner(s) of each third-party copyrighted matter to be included in my work, allowing electronic distribution (if such use is not permitted by the fair use doctrine) which will be submitted to UKnowledge as Additional File.

I hereby grant to The University of Kentucky and its agents the irrevocable, non-exclusive, and royalty-free license to archive and make accessible my work in whole or in part in all forms of media, now or hereafter known. I agree that the document mentioned above may be made available immediately for worldwide access unless an embargo applies.

I retain all other ownership rights to the copyright of my work. I also retain the right to use in future works (such as articles or books) all or part of my work. I understand that I am free to register the copyright to my work.

REVIEW, APPROVAL AND ACCEPTANCE

The document mentioned above has been reviewed and accepted by the student's advisor, on behalf of the advisory committee, and by the Director of Graduate Studies (DGS), on behalf of the program; we verify that this is the final, approved version of the student's thesis including all changes required by the advisory committee. The undersigned agree to abide by the statements above.

Hongyi Wan, Student

Dr. Dibakar Bhattacharyya, Major Professor

Dr. Steve Rankin, Director of Graduate Studies

BIMETALLIC NANOPARTICLES INTEGRATED MEMBRANES FOR GROUNDWATER REMEDIATION: SYNTHESIS, CHARACTERIZATION AND APPLICATIONS

DISSERTATION

A dissertation submitted in partial fulfillment of the
requirements for the degree of Doctor of Philosophy in the
College of Engineering
at the University of Kentucky

By
Hongyi Wan

Lexington, Kentucky

Director: Dr. Dibakar Bhattacharyya, Professor of Chemical Engineering

Lexington, Kentucky

2020

ABSTRACT OF DISSERTATION

BIMETALLIC NANOPARTICLES INTEGRATED MEMBRANES FOR GROUNDWATER REMEDIATION: SYNTHESIS, CHARACTERIZATION AND APPLICATIONS

The detoxification of chlorinated organics from groundwater, such as trichloroethylene (TCE), tetrachloroethylene (PCE), polychlorinated biphenyl (PCB) and carbon tetrachloride (CTC), is a challenging area. Reductive dechlorination has been investigated using iron and iron-based nanoparticles, such as bare Fe, sulfidized Fe (S-Fe) and palladized Fe (Pd-Fe). However, issues including particle agglomeration, difficulties in recycling and particle leaching have been reported to hinder the application and wide usage of these techniques. The integration of nanoparticles and membranes can address these issues because of the large surface area, stability, and the potential for versatile functionalities. In this study, commercial polyvinylidene difluoride (PVDF) microfiltration membranes were functionalized with poly (acrylic acid) (PAA) or poly (methacrylic acid) (PMAA). The functionalization allows the in-situ generation of iron-based nanoparticles through ion-exchange and reduction processes. These membranes were then tested for the removal of chlorinated organics from synthetic and site groundwater.

Both the PAA and PMAA functionalization showed a responsive behavior in water flux through membranes. The deprotonation of carboxyl groups ($-COOH \rightarrow -COO^-$) makes PAA or PMAA become hydrophilic when pH > pKa. Membrane permeability was decreased by 5-30 folds when pH increases from 2.3 to 10.5. PAA and PMAA are anionic polymers in the water at neutral and basic pH, which can capture metal cations for the in-situ synthesis of metallic nanoparticles through a reduction reaction. Uniform Pd-Fe particles with a size of 17.1 ± 4.9 nm were quantified throughout the pores of membranes using a developed focused ion beam cross-sectioning method. The reactive particles incorporated membranes presented over 96% degradation of 3,3',4,4',5-pentachlorobiphenyl (PCB-126) in less than 15 s residence time in passing through the membrane domains.

Roles of Pd fractions, particle compositions and water parameters (pH and temperature) in degradation were evaluated using 2-chlorobiphenyl (PCB-1) as a model compound. The H_2 evolution (Fe corrosion in water) was quantified with various Pd coverages on the Fe surface. H_2 can be activated by catalytic Pd for the hydrodechlorination reaction. However, insufficient H_2 production was observed under the higher Pd coverage (>10.4%, corresponding to 5.5 wt%), resulting in the hindrance of dechlorination. Pd

fractions from 0.5 wt% to 5.5 wt% (1.0% to 10.4% Pd coverage) yielded higher dechlorination performance. In addition, Pd-Fe bimetallic nanoparticles showed an18-fold mass normalized reaction rate (k_{mass}) than that of isolated Pd and Fe nanoparticles.

The investigation of nanoparticles' intrinsic properties and PCB degradation guided the application of the Pd-Fe nanoparticles incorporated membranes in the treatment of contaminated groundwater. Cooperating with Arcadis Us Inc. (a global environmental consulting firm), the contaminant groundwater was obtained from a hazardous waste site in Louisville, KY. In a single pass of Pd-Fe-PMAA-PVDF membranes (0.5 wt% Pd), chlorinated organics in groundwater sample, such as TCE (177 ppb) and CTC (35 ppb), were degraded to 16 and 0.3 ppb, respectively, at 2.2 seconds of residence time. The surface area normalized reaction rate (k_{sa}) in the treatment of the groundwater followed the order of CTC (0.101 $Lm^{-2}min^{-1}$)> TCE (0.034 $Lm^{-2}min^{-1}$)> PCE (0.017 $Lm^{-2}min^{-1}$)> chloroform (0.002 $Lm^{-2}min^{-1}$). A long-term study showed less than 5% CTC and 20% PCE remained in a continuous flow through the membranes within the first 5 h (equivalent of 42 L/m^2 treatment of water). A significant decrease in degradation performance was found after 36 h continuous flow (equivalent of 299 L/m^2 treatment of water), which the reactivity of incorporated nanoparticles was recovered through regeneration using $NaBH_4$. As expected, the on-site technology evaluation also showed effective remediation of the groundwater samples at the similar residence time of the degradation tests in the lab: less than 0.1% CTC, 12% TCE and 18% TCE remained at a residence time of 2.4 seconds. Successful regeneration and reuse of the reactive membranes were also achieved on-site. Analysis of typical samples was also validated by an environmental testing lab (Eurofins TestAmerica, Inc). The on-site remediation evaluation and the studies of regeneration/reuse enhance the optimization of the reactive membrane systems for the potential to scale up.

Alternatives of Pd-Fe were studied in the solution phase to understand the fundamentals. S-Fe were prepared, after the synthesis of precursor Fe^0 nanoparticles (spherical, ~35 nm radius), for the long-term study of CTC. Pd-Fe (0.3 mol% Pd) increased the degradation rate by 20-fold (k_{sa} = 0.580 $Lm^{-2}min^{-1}$) compared to that of Fe while S-Fe presented a greater lifetime (deactivated after 17 days of aging). During the aging process, Fe core was converted to FeOOH and Fe_3O_4/γ-Fe_2O_3 which deactivated the particles. The restoration of Fe^0 was achieved using $NaBH_4$ (400 mol%), which regenerated Fe and Pd-Fe nanoparticles. Even though the Fe core was also restored for S-Fe, the formed FeS_x layers (FeS, FeS_2) disappeared. The results suggest that S-Fe extends the longevity of Fe, but the loss of FeS_x makes S-Fe eventually perform like Fe in terms of CTC degradation.

KEYWORDS: Reactive Membrane, Groundwater Remediation, Long-term Study, Advanced Characterization, Chloro-organics Removal, Regeneration.

Hongyi Wan

(Name of Student)

02/10/2020

Date

BIMETALLIC NANOPARTICLES INTEGRATED MEMBRANES FOR GROUNDWATER REMEDIATION: SYNTHESIS, CHARACTERIZATION AND APPLICATIONS

By

Hongyi Wan

Dr. Dibakar Bhattacharyya
Director of Dissertation

Dr. Steve Rankin
Director of Graduate Studies

02/10/2020
Date

ACKNOWLEDGMENTS

It is my great pleasure to express my thanks to my advisor Prof. Dibakar Bhattacharyya. You brought me enormous interests in the research of the membrane field the first time we met. With a long and warm handshake, you introduced the recent progresses of the field and the amazing achievements from your lab. Honesty, I probably understood only 10% of what you said at that time, but I always remember the spirit and the enthusiasm you presented about the science and the kindness you shared with people. Undoubtedly, I will keep the spirit in my upcoming career and the most important the way how you respect others. You have never blamed us and always on our side. Thank you to provide us opportunities to attend domestic and international conferences. It is fascinating to share research findings and thoughts of life, politics, and sports with people from different generations and distinct regions of the world. Also, you and Gail Bhattacharyya (a very kind and brave person) always support us like your child. I will always cherish the great memories with you two like a family.

I would also like to thank Prof. Lindell Ormsbee, Prof. John Balk and Prof. Barbara Knutson to serve as my defense committee and to provide visions that guided and challenged my thinking. Thanks, Prof. Sridhar Sunderam for serving as my outsider examiner. To Prof. Ormsbee, I am very impressed that you have vast knowledge about hazardous waste sites and treatment methods. We had great times on the campus, in the field, and at Superfund annual conferences. You are a tough man who was not defeated by the surgery. Also, you do have a cool cowboy hat. To Prof. John Balk, I am so grateful we have such an awesome Electron Microscopy Center (EMC). It is not just about the sessions of material characterization, it allows us to understand the mechanism of the

instruments and to train our students as independent users. Your personality motivates us. To Prof. Barbara Knutson, I am glad you were the teacher of our thermodynamic class. You were always patient to our questions and I have never fallen asleep during this class. This understanding of thermodynamic plays a vital role in my research work. To Prof. Sridhar Sunderam, I appreciate that you show many interests in the aspects of fluid and transport during my defense. We also had a great talk after the dissertation.

I enjoy the research atmosphere and daily life at the University of Kentucky (UK). Most of the resources and instruments are opening to our students. Thanks to, Prof. Isabel Escobar, Prof. Yang-Tse Cheng, Prof. Thomas Dziubla, Prof. Zach Hilt, Prof. Steve Rankin, and Prof. Fuqian Yang, for allowing me to use the advanced instruments. Especially, I appreciate Prof. Isabel Escobar for the valuable suggestions in research and my presentation. The Caipirinha, you suggested in the conference in Brazil, became one of my favorite cocktails. A special thanks to the UK EMC center and ERTL lab. Dr. Dali Qian and Dr. Nicolas Briot are great material scientists. We had a great time working together. Thanks, Dr. Azin Akbari and Jillian Cramer to provide support and train me on how to use the instruments. For ERTL lab, thanks to, John May, Tricia Coakley, and Megan Combs, for providing excellent services in analysis and for training me as an independent user. It is glad that I can train other students on how to use the instruments like the way you guys trained me. John May, I am impressed by how well you understand the EPA protocols and how efficiently you solve our issues. We always have nice conversations about travel, basketball, and golf during the process of data storage.

I am grateful for being a part of our productive and diverse research group. We celebrate every year for Prof. DB's birthday at FPAT 7th floor and of course, it is

alcohol-free. I will always remember the smile of each of you guys: Dr. Li Xiao, Dr. Minghui Gui, Dr. Sebastian Hernandez, Dr. Andrew Colburn, Dr. Rupam Sarma, Dr. Priyesh Wagh, Dr. Sneha Chede, John Cravens, Nathan Puckett, Madison Sloan, Conor Sprick, Dr. Ashish Aher, Anthony Saad, Michael Detisch, Saiful Islam, Francisco Leniz, Xiaobo Dong, Joyner Eke, and Dr. Yuxia Ji. It is also great to work with undergrads Paul Lee, Victoria Claus, Rollie Mills, Vogler Ronald, and Cassandra Porter.

Ashish and I always worked together at late night for proposal writing and hung out to grab a pizza. We drove from Orlando to Key West and celebrated with a cup of vodka before bed. You taught me Hindi and Indian songs (thank you, धन्यवाद). Anthony is a guy with lots of talents in soccer, golf and business (do I miss something?). You invited me to UK basketball games and our seats were just two rows behind the players. We went oyster tours several times both in Boston and Orlando. I know it was painful to help me check grammar mistakes line by line. Saiful is always like a big brother to me. You told me "happy wife, happy life". We had great talks about family, politics, and research. I am always impressed by the high-quality artworks you made for the figures. It is my pleasure to work with you for three published papers. Mike is a guy with good tastes in music and alcohol. We had a great karaoke night after we both obtained awards in the NAMS meeting. Dr. Hernandez has an insightful understanding of polymer science. We had a great time at the conference in Puerto Rico. You taught me how to iron a shirt and Spanish of course! Dr. Gui is such a patient person who helps me get my hands wet in the field of membrane science. I wish you and your family have a great life in Boston area. Dr. Colburn is very supportive. You are a role model to show me what leadership means.

Xiaobo Dong is a very awesome team-player. I am always impressed by your energy and motivation. You are a competitive marathon runner and you always fight injustice.

It is my honor to be a member of our UK Superfund center. This center is not just about the research of health issues and environmental protection but also involves lots of community engagements. I am glad I had the opportunity to visit local residences in the Appalachian region. Thanks, Prof. Bernhard Henning and Prof. Zack Hilt for the suggestions of my career and research. Thanks, Prof. Kelly Pennell to help us in technology translation. I would also like to thank Jennifer Moore and Emily Koyagi to save us from all the paper works. Besides, I would like to share my best respects to the extremely responsible staff from the Department of Chemical and Material Engineering: Bruce Cole, Marlene Spurlock, Joshua Duruttya, Amy Terry, Paula Mcgee, Mellissa Witt, and Chelsea Hansing. Thank you, Nick Cprek, for helping me design and build a mobile membrane setup. It is my luck to have very responsible DGS, that is Prof. Thomas Dziubla and Prof. Steve Rankin. I would also like to show my respects to our helpful department chairs over the past few years: Prof. Douglas Kalika and Prof. Thomas Dziubla.

It is great I had the chance to bring our test unit to an actual hazardous waste site. Thanks for the collaboration with Arcadis US Inc, especially to the practical suggestions from Dr. Matthew Schnobrich and Todd Brooks. Thanks, Lucy Pacholik and Tahiya Tarannum for the sampling on-site and the economic estimation.

It is my pleasure that my family always on my side. I would like to thank Xin Wan and Yuan Liu who raise me up and support me for my education. Thanks my parents-in-law, Nianjun Chen and Guili Shen, who brought up such a lovely and independent girl Jialin Chen. Even though my wife Jialin and I have stayed in different countries for five

years, she always respects my work and supports me whenever I am depressed in this long journey. We both have the dream to explorer the majesty of the natural and the world with our hands together. We have had the chance to see the world from different planes, that is we had experience in both skydiving and diving. My grandmother is the one I want to share my progress the most. That was the first time I know what the heartbreak is when she staggered along in the ferry to another world.

In the end, I would like to say a thank you to Kobe Bryant. Even though we have never met in person, you taught me to fight back all the pains, failures and critics. I have decided to adopt the motto, “you can do anything you want to if you really want it”, when I first watch you play against Phoenix Suns in 2006 playoffs. Rest in peace, the legend.

This research is supported by the NIEHS-SRP grant P42ES007380. Partial support is also provided by the NSF KY EPSCoR grant (Grant no: 1355438). A special thanks to Solecta Inc, for providing full-scale membranes for our research.

TABLE OF CONTENTS

LIST OF TABLES

LIST OF FIGURES

CHAPTER 1. INTRODUCTION

1.1 Overview

Remediation of toxic chlorinated organic compounds in groundwater continues to be challenging. Various nanoscale zerovalent iron (nZVI) based nanoparticles have been studied and applied in the reductive degradation of chlorinated organic compounds, such as trichloroethylene (TCE), carbon tetrachloride (CTC) and polychlorinated biphenyls (PCBs). However, some issues were revealed in the application of nZVI based nanoparticles, such as leaching, agglomeration and recycle. The integration of nanoparticles and polymeric membranes shows the potential in addressing these issues because of the large surface area, stability and the versatile functionalities of membrane domains. Therefore, the purpose of this work is to select proper nZVI based nanoparticles as well as membrane domains for the design of reactive nanoparticles incorporated membrane system for the treatment of chlorinated organic compounds in groundwater.

1.2 Background

1.2.1 Chlorinated organic compounds

Chlorinated organic compounds (COCs), such as TCE, CTC and PCBs, were widely used as pharmaceuticals, plastics, and organic solvents [1]. However, due to their high toxicity, chemical persistence and prevalence in the environment, COCs in groundwater, soil and sludge are of global concern [1, 2]. Once entering the environment, COCs will accumulate in the water, air and biosphere. The bio-magnification of some COCs (such as PCB, chlorophenol, and trichloroethylene) in the food chain and water can eventually cause harm to human health [3, 4].

1.2.2 Reductive dechlorination using nZVI method

Conventional degradation methods, such as physical adsorption, bioremediation, incineration and landfill disposal, either requires large energy consumption or needs long reaction period [5-9]. Therefore, a reductive dechlorination treatment method using bulk zerovalent iron has been studied [10, 11]. Due to the large specific surface area, nanoscale zerovalent iron nanoparticles (nZVI) have also been studied to increase the reactivity [7, 12]. The mass normalized rate constant of nZVI (k_m = 1.6 $L*h^{-1}g^{-1}$) was reported to be 3-4 orders of magnitude higher than that of bulk ZVI [13, 14]. Li et al. reported the core-shell model of nZVI (Figure 1.1), where the oxidized shell (iron oxides/hydroxides) provides adsorption sites for the formation of chemical complex and the Fe^0 core serves as an electron donor to offer the reducing power for the remediation of environmental contaminants [15]. For instance, the reductive dechlorination of TCE is illustrated in equation 1.1-1.3 [16]. In addition to COCs [17-21], nZVI has been applied in the treatment of other water contaminants, such as dyes [22-25] and heavy metals [26-29].

$$Fe^0 \rightarrow Fe^{2+} + 2e^- \quad (1.1)$$

$$TCE + n \cdot e^- + m \cdot H^+ \rightarrow products + 3Cl^- \quad (1.2)$$

$$2H^+ + 2e^- \rightarrow H_2 \uparrow \quad (1.3)$$

However, the large specific surface area also has site effects. It makes nZVI susceptible to oxidation by dissolved oxygen and water, which leads to the formation of iron oxides or even iron-based suspensions. The aggregation of synthesized particles leads to a formation of bulky micro-scale particles, which decreases the reaction rate. Both iron oxidation and nanoparticle aggregation reduce the reactivity of nZVI nanoparticles, thus hindering wide scale implementation. Many studies have been conducted to prevent

agglomeration and improve their stability, such as using carboxymethyl cellulose as a stabilizer and using other chelators to bind metal ions. [30-34].

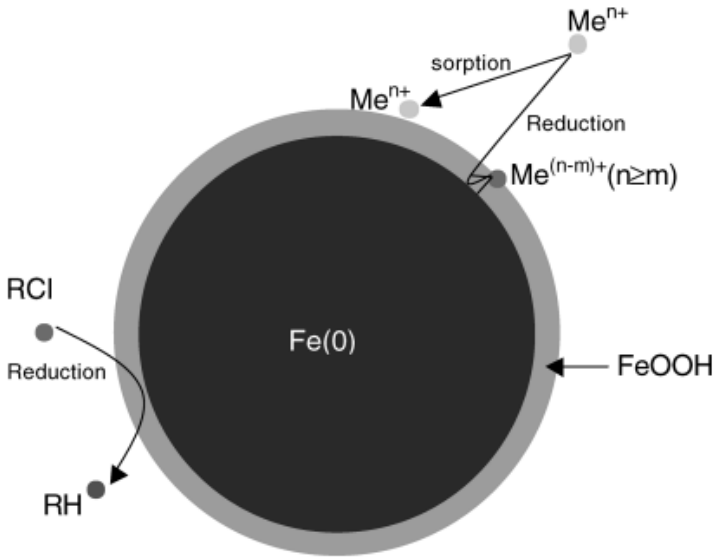

Figure 1.1 The core shell model of nZVI. The Fe^0 serve as an electron donor to provide reducing power for the remediation reaction. The shell is made of iron oxides/hydroxides (nZVI oxidiation). The shell provides adsorption sites to increase the local concentration of contaminants (figure was adapted with permission from Critical Reviews in Solid State and Materials Sciences, Li et al., 2006).

1.2.3 Synthesis and optimization of nZVI based nanoparticles

In industrial, as filling materials in permeable reactive barrier (PBR), more than 200 ZVI-PBRs have been settled worldwide by 2014 [35]. However, the long-term performance of nZVI has been reported limited to water corrosion ($Fe^0 + 2H_2O \rightarrow Fe^{2+} + 2OH^- + H_2$) and subsequently oxidation/surface passivation in groundwater system [36-38]. Field tests using subsurface injection method also revealed some obstacles including particle agglomeration and lack of mobility [39, 40].

Both physical and chemical countermeasures were studied including various stabilizers/porous media [41-49] as well as bimetallic (Ni, Pd) [50-52] or sulfidized nZVI-based nanoparticles [37, 53, 54]. The stabilizers, such as carboxymethyl cellulose (CMC), could well disperse the particle and even control the size of formed particles (<100 nm) [30, 54]. Incorporating nanoparticles with membrane filters has been reported to prevent the leaching of Fe and easily regenerate the Fe based particles: less than 2 % nanoparticles were leaked after an equivalent of 179 L/m^2 flow pass through the membrane [55]. More important, the versatile formation of Fe-based nanoparticles, such as palladized (Pd-Fe) or sulfidized Fe (S-Fe), grants new functionalities in reactivity and longevity. Pd-Fe and bare Fe have different mechanisms in dechlorination reaction. Incorporating Pd as a catalyst, the Pd-Fe nanoparticles activate the produced H_2 (water corrosion of Fe) to atomic hydrogen for hydrodechlorination reaction (Figure 1.2) [51, 56, 57], which enhances the reaction rate and can effectively dechlorinate recalcitrant chlorinated aromatic hydrocarbons, such as polychlorinated biphenyl, 2,4,6-trichlorophenol and 2,4-dichlorophenol [57-59]. (Table 1.1). Rather than activation of produced H_2 for hydrodechlorination, the H_2 evolution is an undesirable side reaction when using both bare

Fe or S-Fe for reductive dechlorination. For S-Fe, the formation of FeS_x (mackinawite, greigite and pyrite) shell on Fe nanoparticles blocks the H_2 evolution from water corrosion of Fe^0 (Figure 1.3) [53, 60], which overall extends the longevity of bare Fe (10-30 days) and presents a higher usage of Fe in dechlorination (better electron selectivity) [61, 62] as well as increases reaction rate [63, 64].

Table 1.1 Recent studies of Pd-Fe bimetallic particles in the treatment of chlorinated organic compounds.

Contaminant	Pd/Fe material	Reference
Chlorinated phenols	Pd-Fe-Fe_3O_4 nanohybrids with multi-walled carbon nanotubes as supporting matrix (3 gL^{-1} Pd/Fe with 0.2 wt% Pd)	[65]
	Iron powder (5-8 um)/Pd (0.17-0.75 wt% Pd) entrapped in alginate beads inside fluidized bed	[66]
	Pd-Fe modified graphene, prepared by the hummers oxidation method and bimetallic co-deposition method	[67]
Polychlorinated biphenyl	Pd-Fe (around 20 nm) in-situ synthesized in PVDF-PAA membrane (with 1.3 wt% Pd)	[50]
	Bare and carboxymethyl cellulose-coated Pd-Fe, EDTA enhances the reactivity of bare Pd-Fe in saline water	[68]
Trichloroethylene	nZVI/Pd (1 gL^{-1} Pd/Fe with 1.5 wt% Pd)	[51]
	Fe/C/Pd composite, carbon nanotubes with ZVI on the inner surface and Pd NPs on the outer surface.	[69]
Carbon tetrachloride	Pd-Fe NPs (50-150 nm) on graphene sheet, showed higher longevity than pure Pd/Fe after five times degradation	[70]

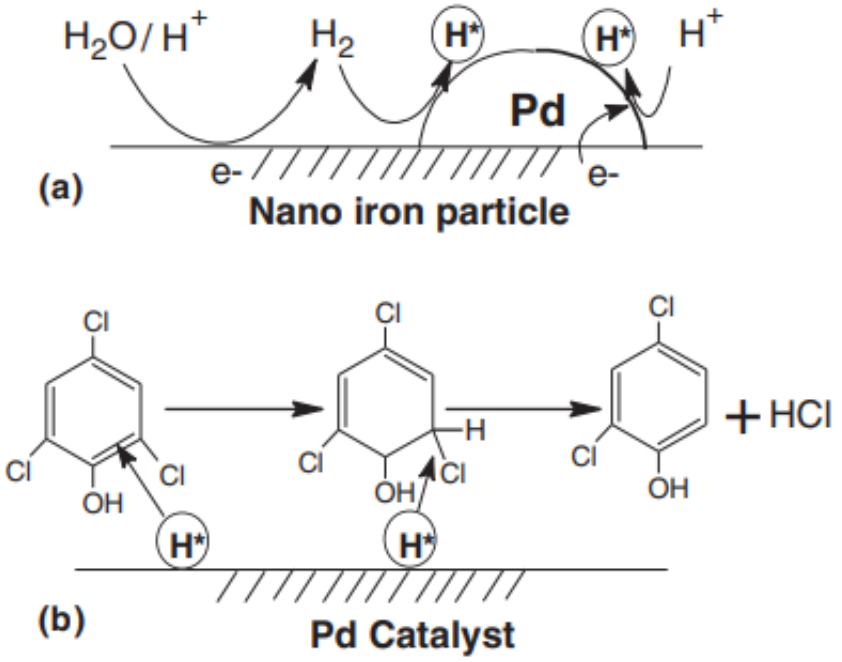

Figure 1.2 Schematic of the proposed mechanism of catalytic hydrodechlorination using palladized Fe nanoparticles. 2,4,6-trichlorophenol was used as a model compound. (a) the formation of atomic hydrogen and (b) hydrodechlorination reaction on the surface of Pd (figure (a) and (b) were adapted with permission from Separation and Purification Technology, Zhou et al., 2010).

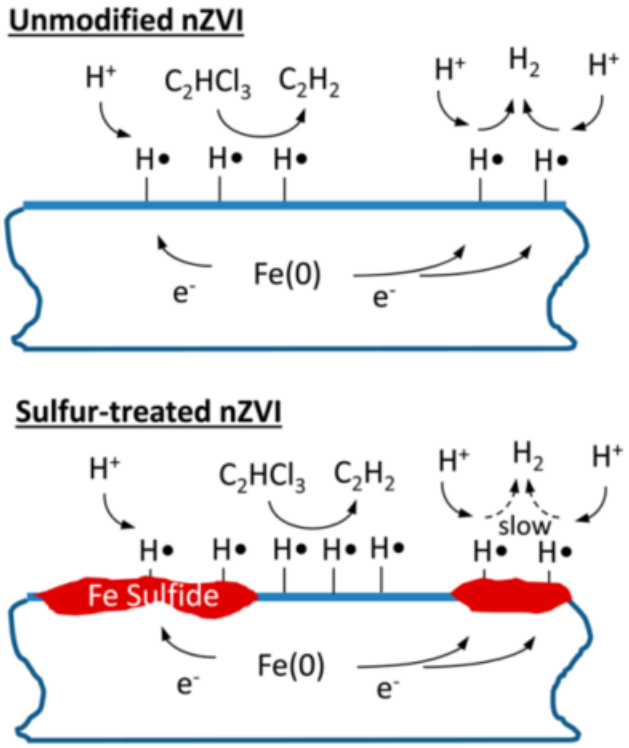

Figure 1.3 Schematic of different dechlorination mechanisms using bare Fe and sulfidized-Fe nanoparticles (figure was adapted with permission from Environmental Science & Technology, Han et al., 2016).

1.2.4 Integration of reactive nanoparticles with membrane domains

Without an appropriate platform, the Fe-based nanoparticles method faces difficulties with recycling and reuse (discussed in section 1.2.1). The integration of nanoparticles and polymeric membranes can address some of these issues because of the large surface area, stability and the potential for versatile functionalities of membrane domains [71, 72].

Understanding the properties of nanoparticles on and underneath the membrane surface is important for investigation of particle reactivity, anti-bacterial properties and effects on membrane hydrophilicity [73-75]. Normal SEM preparation techniques (sectioning, fracturing) usually alter the structure of the region of interest, resulting in the characterization of damaged surfaces. Consequently, proper observation of nanoparticle properties, such as size, distribution, configuration and composition, can only be observed on a membrane's surface or external sides rather than deep inside the membrane pores. Energy-dispersive X-ray spectroscopy (EDS) can be used to prove the existence of metal nanoparticles on both pores and surfaces of the membranes [73]. However, the size and configuration of particles inside the pores of membranes are not able to clearly observed in the EDS. In contrast, cross-sectioning the membranes using focused ion beam (FIB) technique prevents mechanical deformation of the membrane and can provide a clean, smooth surface for nanoparticles characterization [76, 77].

1.2.5 Membrane classification and application

Generally speaking, membrane is a thin barrier which selectively separates particles, ions and molecules. In the area of water treatment, membranes are normally classified based on the pore size. The classification mainly includes microfiltration (MF),

ultrafiltration (UF), nanofiltration (NF) and reverse osmosis (RO) membranes [78]. Warsinger et al. summarized the applications and molecular weight cut-off (MWCO) of these four types of membranes in Figure 1.4 [79]. Since a larger driven force is needed for the membranes with smaller pores, MF/UF membranes have been widely used in the wastewater treatment to save energy and cost. Conventional materials for the fabrication of MF/UF membranes are also summarized in Table 1.2 [79] (reported by Warsinger et al.).

Besides the breakthroughs in membrane fabrication methods and advances in various separation applications over the past decade [80-86] , membrane technologies have been extended to the area of adsorption, fuel cell and catalytic applications [87-89]. The incorporation of metals, non-metallic inorganic substances and enzymes into membrane systems have provided catalytic functions and allowed for applications in chemical synthesis and water treatment as well as a reduction in membrane fouling [90-96]. In water treatment, catalytic membranes show great potential in the remediation of contaminated water by oxidation or reduction methods [97-99]. They also provide an effective treatment technology with a small footprint and low energy cost [100].

Table 1.2 Conventional materials for fabrication of MF/UF membranes (Table was adapted with permission from Progress in Polymer Science, Warsinger et al., 2018).

Material	Acronym	Most common use	Advantages	Disadvantages
Polysulfone	PSU	MF/UF	Good mechanical strength, chemically resistant	
Polyether sulfone	PES	MF/UF	Rigid, compaction resistant, very permeable,	
Polyacrylonitrile	PAN	MF/UF	oxidant tolerant, narrow pore size distribution	
Polyvinylidiene fluoride	PVDF	MF/UF	Very oxidant tolerant, chlorine resistant	Broader pore size distribution
Polyethylene	PE	MF/UF (uncommon)	High resistance to organic solvents, low cost, oxidant tolerant	Poor thermal properties, Weaker fouling resistance
Polypropylene	PP	MF/UF (uncommon)	High resistance to organic solvents, decent mechanical strength	Low fouling resistance, not oxidant tolerant
Polyvinyl chloride	PVC	MF/UF (occasionally)		Poor thermal stability, not oxidant tolerant
Cellulose acetate	CA	RO, MF/UF	Renewable source	Low permeability (RO)
Polyamide	PA	RO (TFC active layer), NF, MF/UF (occasionally)	Small pores, excellent rejection, selectivity	Relatively impermeable/dense

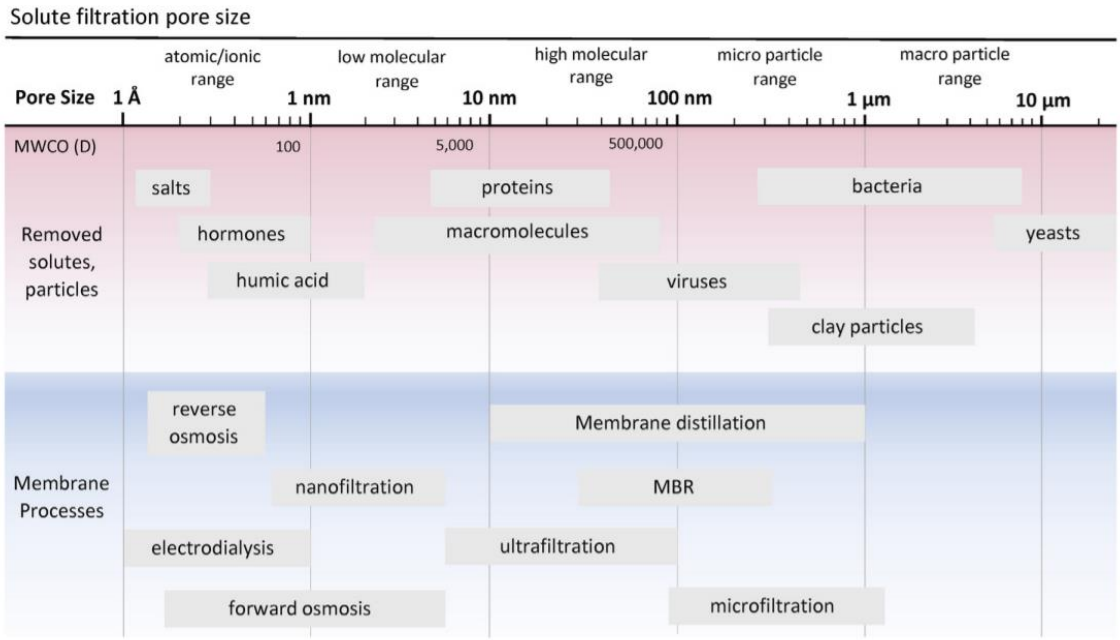

Figure 1.4 Membrane pore size, molecular weight cut-off (MWCO) and applications of typical membrane processes. (figure was adapted with permission from Progress in Polymer Science, Warsinger et al., 2018).

1.2.6 In-situ preparation of nanoparticles in the pores of membranes

Compared to the conventional method to synthesis mixed matrix membranes, in-situ synthesis of nanoparticles inside the pores of membranes provides better dispersion and stability of incorporated nanoparticles [101-104]. Various types of particle precursors, inorganic or polymeric micro/nanoparticles, have been studied as well as the in-situ synthesis metal nanoparticles at different stages of membrane synthesis processes. Li et al. summarized the four major types of in-situ preparation methods in Figure 1.5 [104]. In sol-gel process, the inorganic precursors underwent polycondensation reactions and then the nanostructure of nanoparticles incorporated polymeric membrane matrix was formed during the process of solidification [105]. For in situ chemical reduction method, nanoparticles were formed through redox reactions. Metal cations were firstly mixed in the membrane casting solution or adsorbed on the pores of membranes. Reducing agent was then added to formed less aggregated metallic nanoparticles [75, 106]. Ion-exchange method involves the ion-exchange between the anion from precursor (such as $ZrOCl_2$) and the hydroxyl groups in anion exchangers. Dispersive M-O-M (M refers to Ag, Zr, et al.) units were then formed during the formation of casting solution [107, 108]. Rather than inorganic precursors, in situ polymer reaction uses polymeric micro/nanoparticles enhances the compatibility of formed particle-membranes system, as well as the selectivity and particle loading. Polymeric micro/nanoparticles, such as polyethylenimine and polydopamine, were in-situ cross-linked or polymerized in the casting solution [109, 110].

Among the reported integration methods (which include sol-gel process, particle deposition, in situ reduction, ion-exchange and in situ polymer reaction [104, 111-114]), a combination of ion-exchange method using carboxyl groups (-COOH) and in situ reduction

method has been shown to prevent the aggregation and control the particle size. It can also effectively capture metal ions after the dissolution/corrosion of metallic particles, which shows the potential to prevent the leaching of metal ions and particles [115-117].

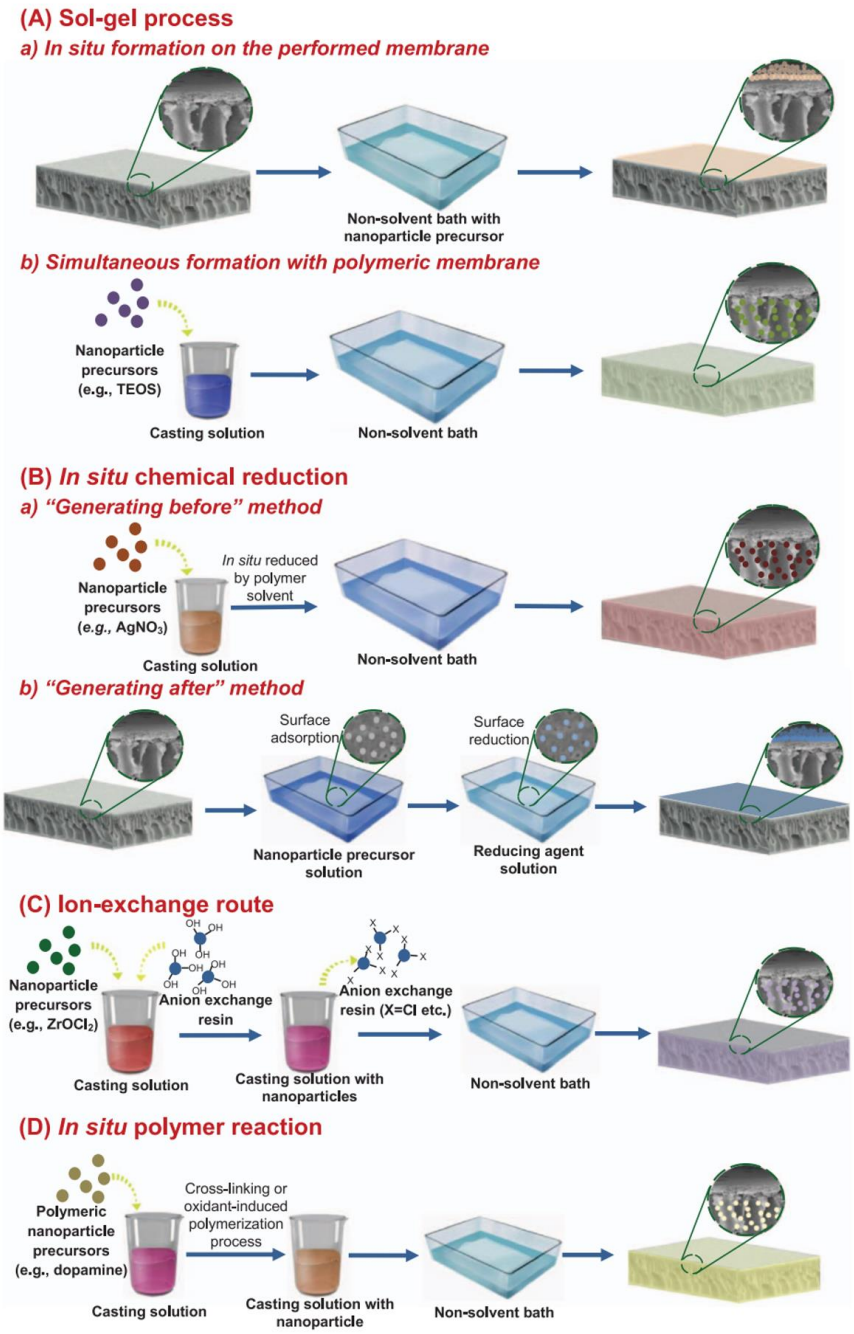

Figure 1.5 Schematic of in-situ synthesis methods of nanoparticles incorporated membranes. (a) sol-gel process; (b) in situ chemical reduction; (c) Ion-exchange method and (d) in situ polymer reaction (figure (a) to (d) were adapted with permission from Journal of Membrane Science, Li., 2017).

1.2.7 Responsive PAA/PMAA hydrogels in membrane functionalization

Polyvinylidene fluoride (PVDF) membranes, due to their excellent chemical resistance and mechanical properties, are largely used in microfiltration and ultrafiltration processes. Functionalized PVDF membranes can be used in advanced water separation and environmental remediation with surface modification (e.g., immobilized nanomaterials [118], dip coating [119], layer by layer assembly [120], and surface grafting [121]) and development of various membranes (e.g., blend membranes [122], thin film nanocomposite membranes [123] and electrospinning membranes [124]).

Poly(acrylic acid) (PAA) and poly(methacrylic acid) (PMAA) have been wildly used as hydrogel. The side chains, with carboxyl groups (-COOH), of PAA and PMAA can lose protons at neutral or base solution (when pH > pKa of polymers). This makes carboxyl groups convert to anion $–COO^-$, which can be used to capture metal cations. Therefore, PAA functionalized PVDF membranes along with novel ion-exchange and in-situ reduction processes for Pd-Fe particle incorporation have been reported for the treatment of chlorinated organic compounds [46, 47, 72, 125]. Carboxylate groups from PAA can ion-exchange with metal cations and the captured metal cations can be converted to metallic nanoparticles (in-situ) through adding reducing agent ($NaBH_4$). These carboxylate groups also prevent the leaching of produced metal ion (i.e., recapture by ion exchange) and nanoparticle aggregation [126]. Tunable membrane pores can be achieved by changing environmental pH through ionization of carboxylate groups from PAA [127, 128].

To scale up the synthesis of reactive membranes, additional process optimizations need to be performed. Although acrylic acid (vapor pressure: 0.004 bar at 20 ℃) is used in

many industries, methacrylic acid, an alternative with similar chemical structure and less volatile nature (vapor pressure: 0.00093 bar at 20℃), was also used as a monomer in this study to introduce carboxyl groups in commercial PVDF membranes.

1.2.8 Challenges

The integration of reactive Fe based nanoparticles (Pd-Fe, Ni-Fe and iron oxide) and polymeric membrane domains has been reported [71, 72, 129]. However, the complex porous structure of membrane matrix limits the understanding of particle properties inside the pores of membrane. Particle size and density distribution are important for derivation of reaction rate constant and simulation of degradation performance. Thus it is important to quantify particle properties throughout the membrane pores.

In addition to the difficulties in characterization, the potential environmental risks of using nZVI based nanoparticles as well as the cost of materials should also be considered. Potential risks of nZVI in environmental exposure, bioaccumulation and transformation have been reported [130-132]. Strategies need to apply to prevent the leaching of nZVI based nanoparticles during the treatment processes as well as to recycle the injected nanoparticles from aquifer, groundwater and soil. Meanwhile, noble metal palladium (catalyst) is 1.5-fold the price of gold (~$2500/ounce, Jan 2020). Small amount of incorporated Pd (0.5 wt% of Fe) means a 30-50% increases in the cost of membrane synthesis. Therefore, the optimal reactive membrane needs to prevent the leaching of incorporated nanoparticles as well as shows the feasibility in recycle and reuse.

Alternative of Pd-Fe nanoparticles needs to be evaluated. Sulfidized-Fe has drawn a wide attention because of its advantages in longevity and ease of synthesis [37, 133]. However, more practical concerns should be emphasized when incorporating reactive

nanoparticles in the membrane domains. Commercial MF/UF membrane is usually a thin film with thickness of 50-200 μm. The degradation period is controlled by the time the contaminant species pass through the pores of membranes. This means the higher the flux through the reactive membranes, the less the degradation time of the incorporated reactive nanoparticles to the contaminants. To effectively remediate groundwater in a pump and treat system, reactive nanoparticles should have greater degradation rate towards the contaminants.

CHAPTER 2. RESEARCH OBJECTIVES

The overall objective is to develop a functionalized membrane platform for in-situ synthesis of bimetallic nanoparticles for catalytic reactions and to evaluate reactive membrane systems in water treatment. To achieve the objective, advanced materials characterization was conducted to enhance the understanding of particle size and distribution into the membranes. The degradation study of polychlorinated biphenyls (PCBs) was further extended to the remediation of a mixture of toxic chlorinated organics from groundwater.

The schematic of objectives is summarized in Figure 2.1. In details, three types of nZVI based nanoparticles, i.e., bare Fe, Pd-Fe and S-Fe were studied to evaluate particle morphology/composition and reactivity during long-term degradation of model compound carbon tetrachloride (CTC). Since Pd-Fe nanoparticles present the greater degradation rate and successful regeneration, polyacrylic acid (PAA) or polymethacrylic acid (PMAA) functionalized polyvinylidene fluoride (PVDF) membranes were synthesized to incorporated the Pd-Fe nanoparticles in the membrane platform to prevent leaching and agglomeration. The further investigation of intrinsic properties of nanoparticles with model compound (2-chlorobiphenyl, PCB-1 and 3,3',4,4',5-pentachlorobiphenyl, PCB-126) guided the application of the Pd-Fe nanoparticles incorporated PMAA (or PAA)-PVDF membranes in the treatment of contaminated groundwater. The groundwater samples were collected from an industrial site and the groundwater contains a mixture of chlorinated aliphatic hydrocarbons, such as trichloroethylene, tetrachloroethylene and carbon tetrachloride (in 10-1000 ppb range). The six toxic chlorinated organic compounds we have been studied in this dissertation are belongs to three types: chlorinated methanes,

chlorinated ethylenes and polychlorinated biphenyls. Their chemical structures are summarized in Figure 2.2. Furthermore, the objectives of this research are divided into three categories as below:

Fe-based nanoparticles synthesis and optimization

- Investigating the differences in morphology/composition of Fe, S-Fe and Pd-Fe nanoparticles under various preparation conditions using TEM and EDS
- Understanding the effects of particle properties (morphology/elemental composition) on the degradation rate of CTC (model compound)
- Evaluation of particle longevity and regeneration in the long-term study of CTC degradation
- Understanding the changes of particle morphology and composition during the long-term studies
- Investigation of the optimal Pd fraction loadings and particle compositions (palladized-Fe versus isolated Pd and Fe) by quantifying H_2 production and corresponding dechlorination performance

Membrane functionalization and characterization

- Development of the optimal membrane platforms for ion-exchange with metal cations for in-situ synthesis of metallic nanoparticles, and establishing flux responsive behavior
- Quantification of the size and distributions of incorporated Pd-Fe nanoparticles across the entire membrane pores

Groundwater treatment

- Effective remediation of the contaminated groundwater samples using the Pd-Fe functionalized membranes and conducting kinetic studies of contaminants
- Investigating the long-term stability and performance of the reactive nanoparticles incorporated membranes
- Evaluation of the degradation performance and nanoparticle properties after the regeneration process
- Evaluation of the performance of reactive membranes for on-site groundwater treatment.

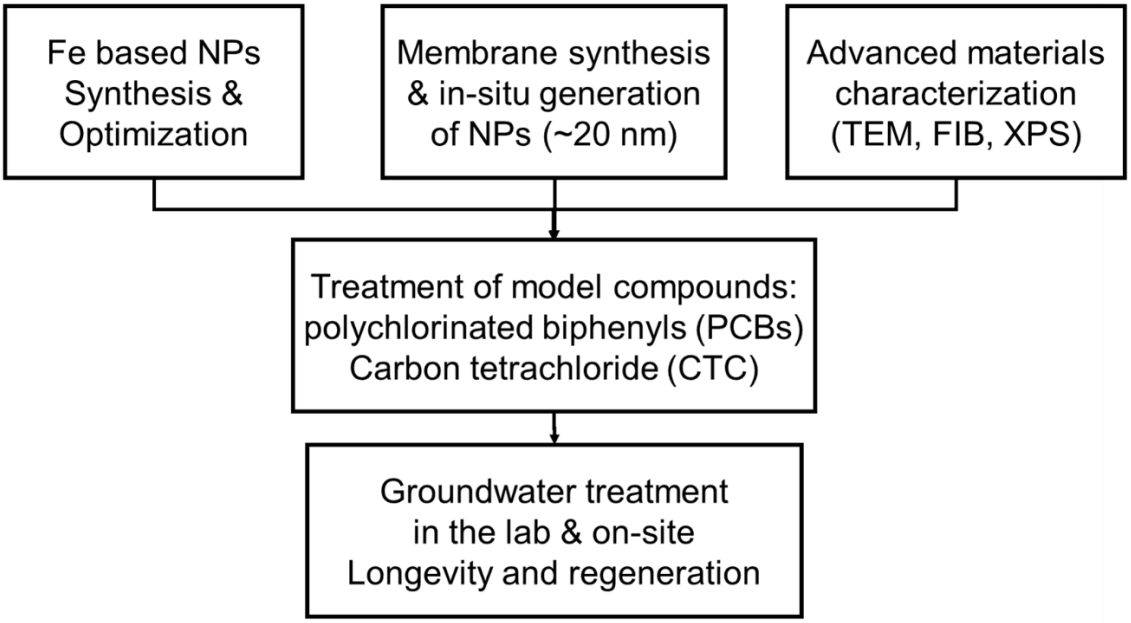

Figure 2.1 Schematic of objectives of synthesizing reactive nanoparticles incorporated membranes for groundwater remediation.

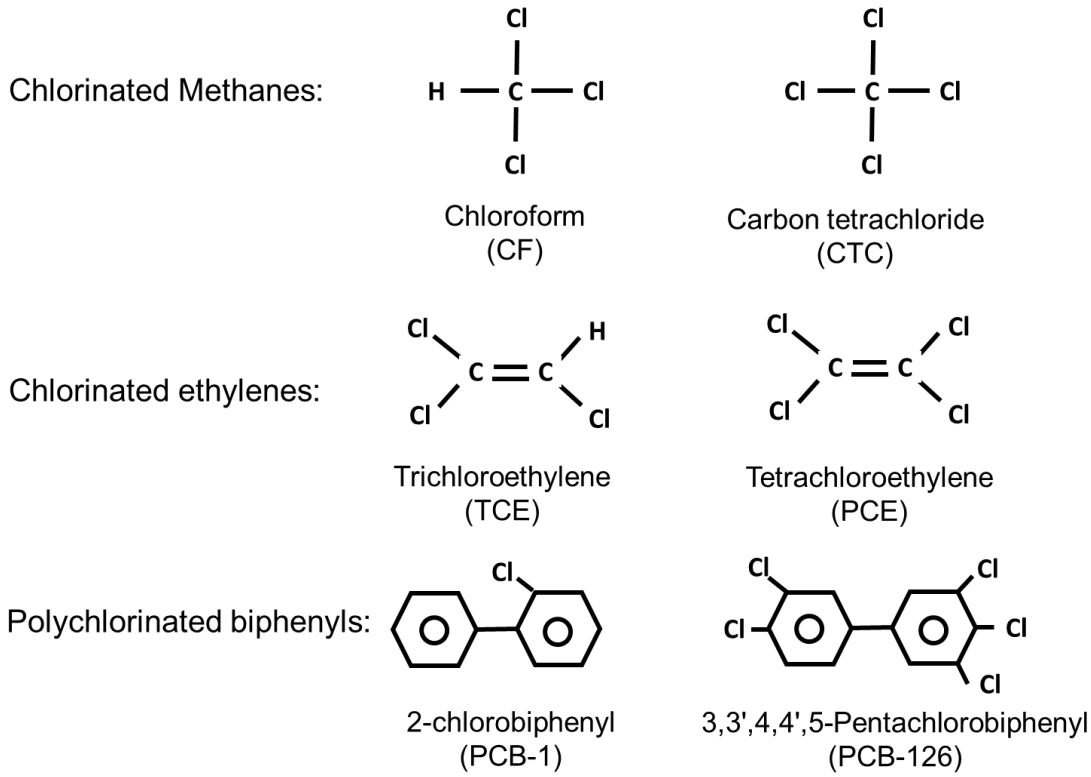

Figure 2.2 Chemical structures of toxic chlorinated organics we have been studied in this dissertation.

CHAPTER 3. EXPERIMENTAL SECTION

3.1 Introduction

This chapter presents all the chemicals, materials and instruments used in the synthesis, characterization and application aspects of this research. Details of membrane functionalization and nanoparticle synthesis are also illustrated. The instruments used in characterization of membrane morphology and nanoparticle properties are discussed, such as scanning electron microscopy (SEM), focused ion beam (FIB), transmission electron microscopy (TEM), energy-dispersive X-ray spectroscopy (EDS), X-ray diffraction (XRD), X-ray photoelectron spectroscope (XPS) and Fourier-transform infrared spectroscopy (FTIR). The analysis methods conducted for the measurement of various organics and metal ions are recorded, including gas chromatography-mass spectrometry (GC-MS), inductively coupled plasma optical emission spectroscopy (ICP-OES) and gas chromatography-thermal conductivity detector (GC-TCD).

3.2 Materials

The following chemicals were used as received: sodium hydroxide (1 M), sulfuric acid (0.5 M), hexanes (>99%), anhydrous sodium sulfate, ferric chloride hexahydrate, ferrous sulfate and ferrous chloride tetrahydrate were obtained from Fisher Scientific. Sodium borohydride (99.99%), sodium carboxymethyl cellulose (CMC) (Mw~90k), potassium tetrachloropalladate (II) (98%), acrylic acid (99%), biphenyl_d10 (99 atom % D), sodium sulfide, trichloroethylene (99.5%), naphthalene_d8 (99 atom % D), PAA powder (M_W = 2000), and tetrachloroethylene (>99%) were purchased from Sigma-Aldrich. PVDF powder was purchased from Polysciences, Inc. Potassium persulfate (98%), N,N'-methylenebisacrylamide (NNMA, 99%) and methacrylic acid (99.5%, stabilized) were

received from Acros Organics. Nitric acid (AR select ACS) was ordered from Macron Fine Chemicals. 2-chlorobiphenyl (PCB-1) (> 97%), 3,3',4,4',5-pentachlorobiphenyl (PCB-126) (> 97%, neat), biphenyl (> 97%, neat) and their analytical solutions (100 ppm in hexane) were obtained from Ultra Scientific. The analytical standard of a mixture of halo-alkanes (DWM-540-1, 200 ppb in methanol for all) was also purchased from Ultra Scientific. Ethanol (200 proof) was bought from EMD Millipore Corporation. Iron (III) chloride hexahydrate (98%) was ordered from Alfa Aesar. Full scale PVDF 700 microfiltration membranes were obtained from Solecta, Inc. DVPP04700 membranes were purchased from Millipore. Deoxygenated water was obtained by purging N_2 into deionized ultra-filtered (DIUF) water for 60 minutes.

3.3 Synthesis of Fe based nanoparticles in an aqueous phase

3.3.1 Synthesis of bare Fe, S-Fe and Pd-Fe with 30 vol% ethanol

Fe^0 particles (precursor) were synthesized in aqueous ethanol (30 vol%) using a borohydride reduction method. The sulfidized Fe (S-Fe) and palladized Fe (Pd-Fe) nanoparticles were prepared after the synthesis of the Fe^0. DI water and ethanol were deoxygenated by purging the N_2 for 1 h before the synthesis. With a mechanical stirrer at a speed of 100 rpm, 0.48 g $FeCl_3$ $6H_2O$ (0.035 M) were dissolved into 50 ml aqueous ethanol (30 ml ethanol) in a 3-neck round bottom flask. At a titration rate of 5 ml/min, 50 ml $NaBH_4$ (0.140 M) solution was drop-wise delivered to the flask and to reduce the dissolved Fe^{3+} to form Fe^0 nanoparticles as the following reaction (3.1):

$$4Fe^{3+} + 3BH_4^- + 9H_2O \rightarrow 4Fe^0 \downarrow + 3H_2BO_3^- + 12H^+ + 6H_2 \uparrow \qquad (3.1)$$

The reduction of 1 mol Fe^{3+} requires 0.75 mol borohydride. Excess borohydride (400 mol% of Fe^{3+}) was added to achieved a complete conversion of Fe^0 nanoparticles.

After titration of $NaBH_4$ solution, the Fe suspension was mixed for another 30 min to consume excess $NaBH_4$. The Fe suspension was then separated using magnet. The nanoparticles were washed three times with water and ethanol, separately. Finally, the nanoparticles were stored in a 200 proof ethanol solution to prevent oxidation.

The post preparation methods of S-Fe and Pd-Fe nanoparticles were adapted from literature [18, 134]. All the preparations were conducted in 8 ml vials with no head space left in the vials to prevent the oxidation of Fe. For the synthesis of S-Fe, the prepared Fe^0 nanoparticles were added in Na_2S $9H_2O$ solution (S/Fe = 0.2 or 2 in atomic fraction) for 10 min sonication and the suspensions was then placed on an orbit shaker (300 rpm). For the preparation of Pd-Fe bimetallic nanoparticles, the synthesized Fe^0 nanoparticles were added in K_2PdCl_4 solution for reaction on an orbit shaker at 300 rpm. The prepared nanoparticles were then washed three times with ethanol and were stored in a 200 proof ethanol solution for further studies.

The synthesis of S-Fe:

$$Fe^0 + 2H_2O \rightarrow Fe^{2+} + 2OH^- + H_2 \uparrow \quad (3.2)$$

$$Na_2S + H_2O \rightarrow 2Na^+ + HS^- + OH^- \quad (3.3)$$

$$Fe^{2+} + 2HS^- \rightarrow FeS + H_2S \uparrow \quad (3.4)$$

The synthesis of Pd-Fe:

$$Fe^0 + PdCl_4^{2-} \rightarrow Pd + Fe^{2+} + 4Cl^- \quad (3.5)$$

For better XRD signals, Pd-Fe (2.5 mol%) particles were prepared just for characterization. To evaluate reactivity, $FeS_{mackinawite}$ was synthesized by directly mixing Na_2S solution into $FeCl_2$ solution (Na_2S is 200 mol% of $FeCl_2$). The formed $FeS_{mackinawite}$

particle was separated using centrifuge (6000 rpm). The particle was washed three times with DI water and then dried in vacuum without heating.

3.3.2 Pd-Fe nanoparticle prepared using sodium carboxymethylcellulose

A 500 ppm ferrous iron solution (ferrous sulfate heptahydrate) was made with 0.5 wt% sodium carboxymethylcellulose (CMC). The solution was transferred into 8 ml vials which were shaken at 500 rpm. After purging N_2 for 15 min, excess $NaBH_4$ solution (400 mol% of Fe) was added to form Fe nanoparticles. The N_2 bubbling continued for another 30 min to consume the excess $NaBH_4$ and also prevent the oxidation of iron nanoparticles. K_2PdCl_4 solution was then added to form Pd coating on the surface of Fe. In addition to Pd-Fe, isolated Fe and Pd nanoparticles were also synthesized. Instead of being reduced on the Fe surface, Pd nanoparticles was synthesized following the same procedures as the synthesis of ZVI. Pd nanoparticles were then mixed with the suspension of Fe nanoparticles.

3.4 Development of reactive PVDF membrane systems

3.4.1 In-situ polymerization of AA or MAA inside PVDF membrane pores

Commercial PVDF microfiltration membranes, due to their durability and chemical resistance, were selected as the membrane domain for further functionalization. Carboxyl groups were introduced into the pores of PVDF membranes by in-situ polymerizing acrylic acid (AA) or methacrylic acid (MAA). The conventional dip-coating method requires immersing the base membrane into the monomer solution before the polymerization. However, the residual of monomer tends to form a top layer on the membrane surface, which blocks the membrane pores and decreases membrane permeability. To diminish the formation of the top layer, a pass-through method was used in this study. The PVDF

membranes were firstly placed in a Büchner funnel with a Büchner flask connected (Figure 3.1). Monomer solution (20 ml acrylic acid, 1 mol % ammonium persulfate as initiator, 1 mol % NNMA as cross-linker and 30 ml deoxygenated water) was drawn through the membrane by vacuum suction (0.17 bar vacuum). The permeate monomer solution was then collected and drawn through the membrane three times to wet the membrane pores. The excess monomer solution remaining on the membrane surface was swept away using a stream of nitrogen gas. For polymerization reaction, glass plates were used to sandwich the membrane before transferring it into an oven at 70 ℃ for 1 h in vacuum (since O_2 is an inhibitor of the reaction). After polymerization, PAA functionalized membranes were washed three times with DI water and then ethanol. Membranes were then dried for weight gain measurement.

This pass-through functionalization method is conducted in an environmentally benign water-based system, which prevents the formation of the top layer on the membrane surface (block membrane pores). In addition, different types of monomer were also considered. Although acrylic acid (vapor pressure: 400 Pa at 20 ℃) is wildly used in many industries, methacrylic acid (MAA), an alternative with similar chemical structure and less volatile nature (vapor pressure: 93 Pa at 20 ℃), was used as a monomer to decrease the exposure of volatile organic compounds. The functionalization of PMAA was conducted as the same pass-through method as the PAA. MAA monomer solution contains 7.5 ml methacrylic acid, 1 mol % potassium persulfate as initiator, 1 mol % NNMA as cross-linker and 40 ml deoxygenated water. The polymerization was conducted into an oven at 80 ℃ for 1 h in vacuum (Figure 3.2).

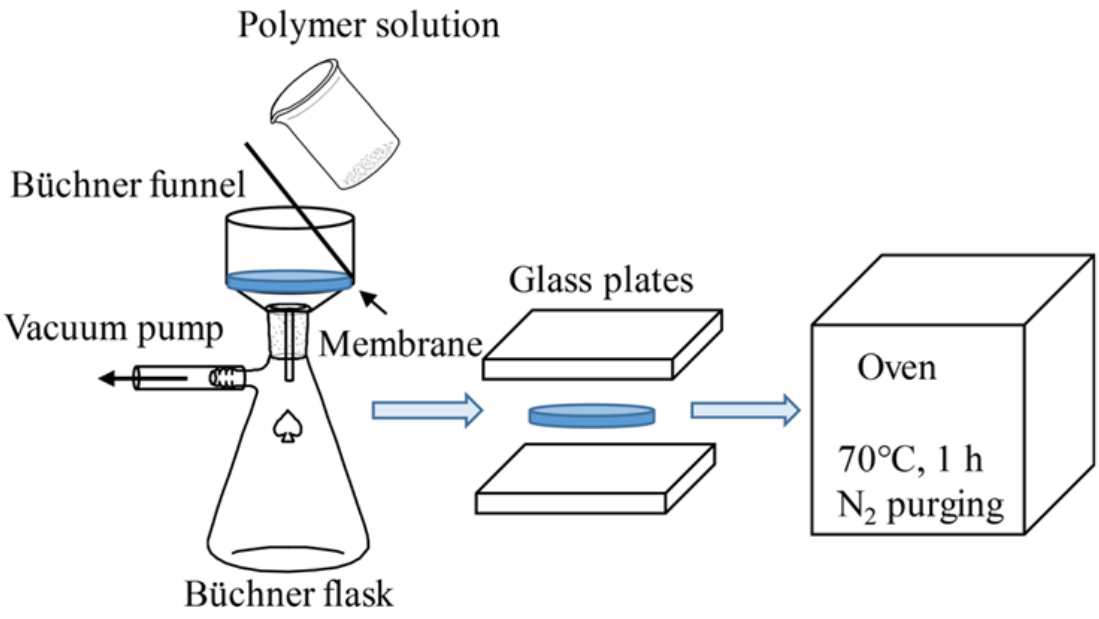

Figure 3.1 Schematic of membrane functionalization method (pass-through method).

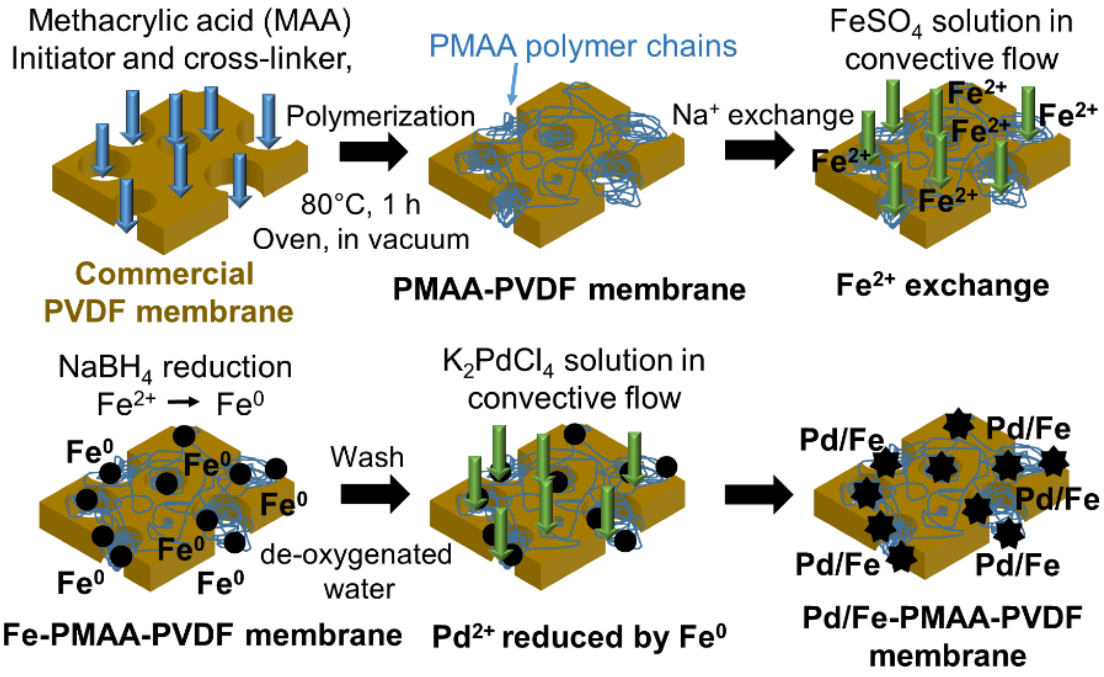

Figure 3.2 Schematic of the synthesis procedures of Pd-Fe-PMAA-PVDF membranes under pass-through method.

3.4.2 Synthesis of Pd-Fe nanoparticles into the pores of membranes

Pd-Fe nanoparticles were generated inside the membrane pores in two steps: ion exchange and reduction reaction. The PAA or PMAA functionalization brings carboxyl groups in the membrane, which could be used to ion exchange with metal ions and further control the size of formed metal nanoparticles. All the ion-exchange and metal reduction steps were conducted in a membrane filtration cell to ease the process of functionalization and enhance the possibility of applying the method in a commercial spiral wound module. Sodium sulfate solution (33 mM), with pH adjusted to 10.6, was pressurized through the membrane at 6.9 bar (150 min) for the Na^+ exchange, in order to facilitate the following ion exchange of Fe^{2+}. Ferrous sulfate solution (36 mM, pH 4.2) was then pressurized through membrane at 1.7 bar (30 min). The $NaBH_4$ solution (210 mol% of Fe) was used to reduce Fe^{2+} and form Fe nanoparticles inside the pores. After washing by de-oxygenated water, potassium tetrachloropalladate was pressurized through the membrane for Pd coating, freshly made Fe could reduce the Pd^{2+} and synthesized Pd islets are located on the surface of Fe particles. After Pd coating, synthesized Pd-Fe-PMAA-PVDF membranes were store in pure ethanol for further application. The similar technique was also applied to synthesize Pd-Fe-PAA-PVDF membranes.

3.5 Characterization

3.5.1 Membrane morphology

The morphology of the membrane surface and the size of the pores were observed using SEM and counted using ImageJ software. The membrane hydrophilicity was tested using a drop shape analyzer (DSA 100, Krüss). Attenuated total reflectance-Fourier

transform infrared spectroscopy (ATR-FTIR, Varian 7000e) was used to identify the functionalization of the PAA and PMAA.

3.5.2 Size and composition of Fe based nanoparticles

The structural characterization was conducted by an X-ray diffractometer (XRD, Siemens D500) using Cu Kα (1.5418 Å) radiation. The spectra were obtained from 2θ angles of 20-100 º, with a step size of 0.1 ºand a 1 s dwell time. Freshly made particles were washed with ethanol and then dried under vacuum. Particle morphologies were investigated using a transmission electron microscopy (TEM, FEI Talos F200X). Particles were dispersed in ethanol with 10 min sonication and then deposited on lacey/carbon copper grids. The grids were dried in oven overnight under vacuum (40 ℃). Particles composition was analyzed using an energy-dispersive X-ray spectroscopy (EDS) and X-ray Photoelectron Spectrometer (XPS, Thermo Scientific K-Alpha). XPS measurement uses an aluminum mono-chromatic X-ray source (1486.69 eV) and an electron flood gun for charge neutralization. Wide scans were performed at a pass energy of 160 eV and high-resolution scans were performed at a pass energy of 20 eV.

3.5.3 Properties of Pd-Fe nanoparticles inside membrane pores

Particle size and distribution were quantified across the entire depth of membranes by directly imaging the cross-section plane of the membrane in the SEM. To maintain the structures of the particles and membrane pores, an advanced cross-sectioning method using focused ion beam (FIB, FEI Helios Nanolab 660) was developed: A cross-sectional plane was first created by fracturing a small piece of the membrane following immersion in liquid nitrogen. The FIB was then performed to expose an undamaged region of the membrane. For gallium ion-based FIB systems, typical cross-sectioning processes only expose the first

few tens of micrometers below the surface [50, 135]. The advanced FIB preparation method allows exposure of the entire membrane cross-section (170 μm), creating a flat and smooth surface suitable for SEM imaging and elemental analysis. As shown in Figure 3.3, a small piece of the membrane was mounted on a 45 °pre-tilted SEM sample holder, with the damaged cross-section surface (resulting from brittle fracture) slightly extending over the holder's top edge. In the Helios Nanolab 660 FIB/SEM, an extra 7 °stage tilt positions the membrane's cross-section surface parallel to the ion beam. A portion of the damaged cross-section was then "cleaned out" by pointing the ion beam along a line at the surface, and slowly moving this line inward (cleaning cross-section script, Figure 3.3b). At high milling rates (30kV, 47 nA), a 170x20x10 μm^3 window can be cleared in ~30 minutes, erasing the surface damage and creating a smooth cross-section surface.

The surface exposed by the FIB milling can subsequently be characterized after rotating and tilting the stage to 45 °, to place the cross-section normal to the electron beam (Figure 3.3c). The particles location and size distribution was then determined by SEM imaging, at different depths throughout the membrane. In addition, the distribution in atomic ratio between iron and fluorine inside the membrane pores was quantified in different depths underneath the membrane surface using EDS (Oxford Instruments, X-MaxN 80 detector) line scan and mapping methods. The EDS was applied to quantify particle distribution inside the membrane pores by obtaining iron to fluorine atomic ratio (since the fluorine content is constant for every PVDF repeat units).

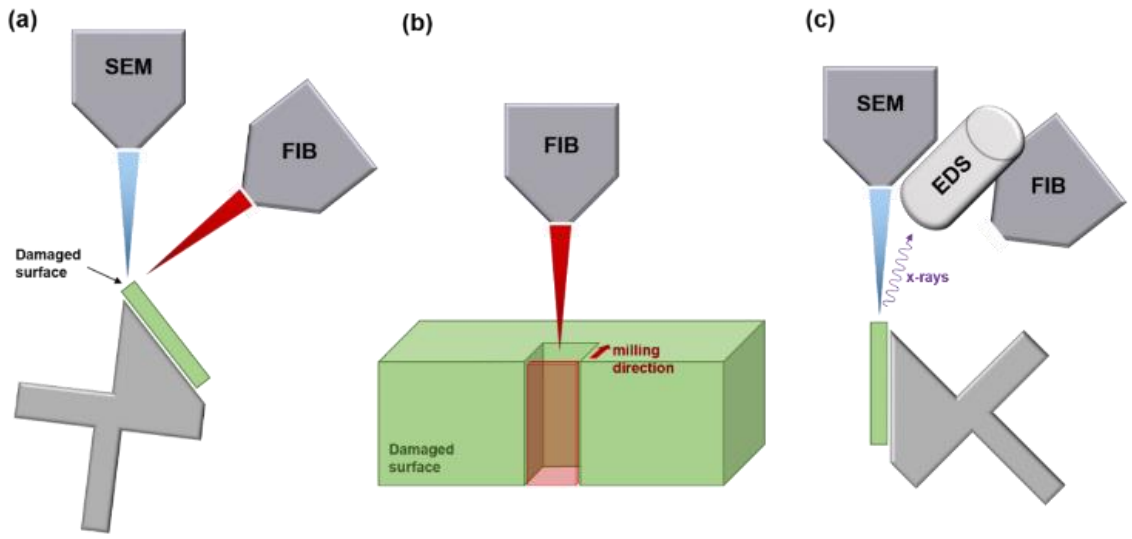

Figure 3.3 Schematic of focused ion beam preparation method and following characterization processes.

3.6 Analytical methods

3.6.1 Metal loading

Inductively coupled plasma optical emission spectroscopy (ICP-OES, VARIAN) was used to accurately measure the concentration of metal ion in solution. The amount of absorbed Fe in the ion exchange process was determined by mass balance after the Fe exchange process. The amount of Fe and coated Pd in the membranes were measured by digesting Pd-Fe immobilized membranes in dilute nitric acid (20%) with heat (40 ℃) before ICP-OES analysis.

3.6.2 PCBs analysis

PCBs analysis was performed using a gas chromatography (Varian CP-3800)-mass spectrometry (Saturn 2200). The temperature of the oven, the injector and the detector were 50 ℃, 250 ℃ and 300 ℃, respectively. The oven was then heated up to 300 ℃ at 12 ℃/min and maintained for 5 min. Hexanes was used as an extraction solution to extract the biphenyl, PCB-1 and PCB-126. The biphenyl_d10 was also added to the extraction solution as an internal standard (10 ppm). The calibration curves of biphenyl, PCB-1 and PCB-126 were all made by using eight standard points range from 0.3 ppm to 5 ppm. The R^2 value for all the calibration curves was above 0.998.

3.6.3 Volatile chlorinated organic compounds

Volatile chlorinated organic compounds (VOC) were measured using a purge and trap GC-MS method (EPA method 624 for purgeable organics). For groundwater samples, the target chlorinated organic compounds include chloroform (CF), carbon tetrachloride (CTC), trichloroethylene (TCE) and tetrachloroethylene (PCE). A Tekmar 3100 purge and trap concentrator, the Varian 3900 GC with CP-select 624 CB column

and Saturn 2100T MS were used in these analyses. Temperature conditions for oven, inlet and detector were 40 ℃, 200 ℃ and 220 ℃, respectively. The oven was first heated to 130 ℃ at a rate of 8 ℃/min and then heated up to 220 at 20 ℃/min where it remained for 2.25 min. The calibration curves of different chlorinated organics were made with an internal standard mixture (STM-341N; including chlorobenzene-d5, 1,4-dichlorobenzene-d4, 1,4-difluorobenzene and pentafluorobenzene, purchased from Ultra Scientific. Each calibration curve was made by using eight standard points ranging from 1 to 1000 ppb and the R^2 value for all the curves were above 0.98.

3.6.4 Hydrogen gas analysis

Measurement of the resulting H_2 from Fe corrosion in water was conducted using GC analysis. At select time intervals, 1 ml headspace vapor was withdrawn by a gastight syringe (Hamilton, Gastight 1001) for GC analysis. The Agilent 6890N GC, equipped with Carboxen-1006 Plot column and thermal conductivity detector, was used for the detection of hydrogen molecules. Temperature conditions for oven, inlet and detector were 50 ℃, 100 ℃ and 150 ℃, respectively. The oven was then heated up to 150 ℃ at 10 ℃/min and then maintained for 5 min. N_2 was used as carrier gas. The calibration curve of hydrogen was made by using the five standard points (commercial gas standard, hydrogen and nitrogen, from Scott-Gross Company, Inc) from 100 ppm to 1000 ppm (gravimetric).

The total moles of produced hydrogen can be quantified by using ideal gas law and Henry's law:

$$n(H_{2,total}) = n(H_{2,g}) + n(H_{2,l}) \qquad (3.6)$$

$$p_{H_2} = \frac{8.314Tn(H_{2,g})}{V_g} \qquad (3.7)$$

$$n(H_{2,l}) = 7.8 \times 10^{-6} p_{H_2} V_l \qquad (3.8)$$

where p_{H_2} is the partial pressure of H_2 (kPa) in the vials. T is room temperature 295.15K. V_l is the solution volume in the vials. In this case, $n(H_{2,g})$ can be measured using GC.

3.6.5 Chloride ion analysis

A chloride electrode (Fisherband Accumet), with 1000 ppm NaCl as a standard, was used to measure chloride ion in aqueous solution. A 2 vol% ionic strength adjuster (5 M $NaNO_3$ solution, Fisher chloride ISA solution) was added to each sample before measurement. The measurement of produced chloride ion could be used to validate the dechlorination reaction.

3.7 Long-term CTC degradation and the regeneration of Fe based nanoparticles

The Fe, S-Fe and Pd-Fe nanoparticles were evaluated in a long-term degradation study of carbon tetrachloride (CTC). The study includes 6 degradation cycles during a total 31-days of aging. All the degradations were conducted in the 8 ml vials without head space (300 rpm shaking at 22 ℃). A stock solution of CTC (0.25 mM) was replaced among different cycles, which corresponds to an aging-time of 0, 3, 5, 10, 17 and 31 days, respectively. This replacement involves magnetic separation of nanoparticles, drain of solution and refill with stock solution. Each degradation cycle operates for 24 h and all the vials were then placed on a magnet for 15 min to separate Fe based nanoparticles ($[Fe]_{initial}$ = 250 ppm). 0.3 ml solution was transferred to a 40 ml vial for GC-MS analysis. The deoxygenated water was replaced daily between the degradation cycles for the purpose of

aging. After the first 31-days of aging, the collected Fe based nanoparticles were regenerated using $NaBH_4$ (400 mol% of $[Fe]_{initial}$). The regenerated nanoparticles (30 min regeneration) were washed three times before degradation study. Duplicates were tested for the long-term study. Particle morphology and composition at different stages during the long-term studies were characterized using TEM, EDS, XRD and XPS. For each degradation cycle, the nanoparticles were sonicated for 10 min for a well dispersion.

3.8 PCB diffusivity through PAA functionalized membranes

PCB diffusivity through the membrane is important for understanding the influence of PCB mass transport and for the simulation of PCB degradation. In order to investigate the diffusion rate of PCB, a thin membrane barrier was pressed between the feed side and permeation side to measure the rate of PCB penetration through the membrane. A 300 ml ethanol water mixture (V/V = 1/9) was simultaneously added into both sides of the diffusion cells. A concentration of 15 μM PCB-126 was then added to the feed side of the membrane. At time zero, PCB-126 began to diffuse from the feed side to the permeation side by penetrating the membrane. The solution in both sides was stirred vigorously during the whole diffusion test (300 rpm). The membrane separating the two sides had an area of 3.46 cm^2. The concentration of PCB-126 on both sides of the membrane was measured over time using gas chromatography (Varian CP-3800)-mass spectrometry (Saturn 2200). Triplicate samples were collected by taking 2 ml of solution at each sides. The collected samples were extracted with 2 ml hexanes (10 ppm napathelene_d8 as an internal standard, shaking at 350 ppm for 2 h).

3.9 PCB-126 degradation

PCB-126 degradation was evaluated in convective flow mode. PCB-126 was dissolved in absolutely pure ethanol with stirring due to its extremely low water solubility. For the convective flow study, a piece of functionalized membrane was put into a dead-end filtration cell (15 μM PCB-126, $V_{ethanol}/V_{water}$ = 1/9, pH = 5.5). The effective external area was 13.2 cm^2. Permeate was collected after 20 minutes when the reaction was observed to approach steady state. Separate samples were then collected at 10 minute intervals while varying the operating pressure. Triplicate samples were collected for GC-MS analysis. In this case, residence time (the average time of particles spent in the membrane) was varied by changing the pressure applied in the filtration cell (1.38 bar to 8.96 bar). The collected permeates were extracted using hexanes (10 ppm naphthalene_d8 added as an internal standard, 2h shaking at 350 ppm) and then transferred for GC-MS measurement.

3.10 PCB-1 degradation at various pH and temperature conditions

For PCB-1 dechlorination, the 4 ml Pd-Fe-CMC solution was transferred into 8 ml vials. Prior to PCB-1 dosing, the pH was adjusted to 3.5, 7.8 and 9.2 using H_2SO_4 or NaOH. The vials were shaken at 500 rpm for the whole duration of the batch study. The extraction solution (4 ml hexanes solution with 10 ppm biphenyl-d10 used as internal standard) was added for 1 min vigorous extraction; the hexanes phase was then analyzed by using GC-MS. There was less than 5% deviation between injecting biphenyl and PCB-1 directly into the hexane versus injecting those into water followed by 1 min of hexane extraction, indicating high extraction efficiency. Different temperature conditions (4 ℃, 15 ℃, 23 ℃ and 40 ℃) were achieved by using a water bath with a mixer. For H_2 measurement, the 4

ml Pd-Fe-CMC solution was transferred into 8 ml vials with septa. The vapor phase was collected for GC analysis.

3.11 Groundwater treatment using Pd-Fe incorporated membranes

For groundwater treatment, the 6 ml Pd-Fe-CMC solution was transferred into 40 ml vials. The vials were then filled with groundwater sample without headspace. Deliberately oxidized Pd-Fe particles were used as the control group. The samples were tested with purge and trap GC-MS method.

Pd-Fe functionalized membranes, with an effective external area of 11.2 cm^2, were evaluated using a dead-end filtration cell (HP4750 stirred cell, STERLITECH corp.). The residence time (the average time particles spent in the membrane) was controlled by changing the operating pressure. In this study, the groundwater samples were permeated through the Pd-Fe incorporated membranes at various operation pressures (0.34, 0.69 and 1.0 bar). The functionalized membranes without Pd-Fe particles were also investigated as a control group to determine the loss of target chlorinated organics due to adsorption and evaporation.

3.12 On-site groundwater remediation using reactive membrane unit

For on-site technology evaluation, chloride ion was measured on-site using chloride electrode to monitor the dechlorination performance. The initial and treated samples were collected and water pH and concentration of contaminants were then measured in the lab.

Pre-filtration was needed to remove the sediments from the groundwater, which could block the pores of membrane and hinder the flux. Therefore, the Keystone 5-micron filter cartridge was firstly connected to the sampling port of the inlet of the existing air

stripping system (on-site). After pre-filtration, a 1 L groundwater was transferred to the feed container of the cross-flow membrane unit (Figure 3.4). The synthesized reactive membrane (16.4 wt% PMAA functionalized, 20 cm^2) was transferred from ethanol storage solution (after washed with deoxygenated water three time) to the cross-flow setup. Valve was used to control the flux through the membrane, which determines the reaction period the contaminants spent in the membrane pores. The treated samples were collected after 30 min to allow the system to reach a steady state. Considering the high heat generation of the pump (reach 80^oC in motor area after 2.5 h operation), there is a 0.5 h break time between every operation cycles (2.5 h). Both a 2 h continuous flow study with two repeat cycles and a long-term study were achieved.

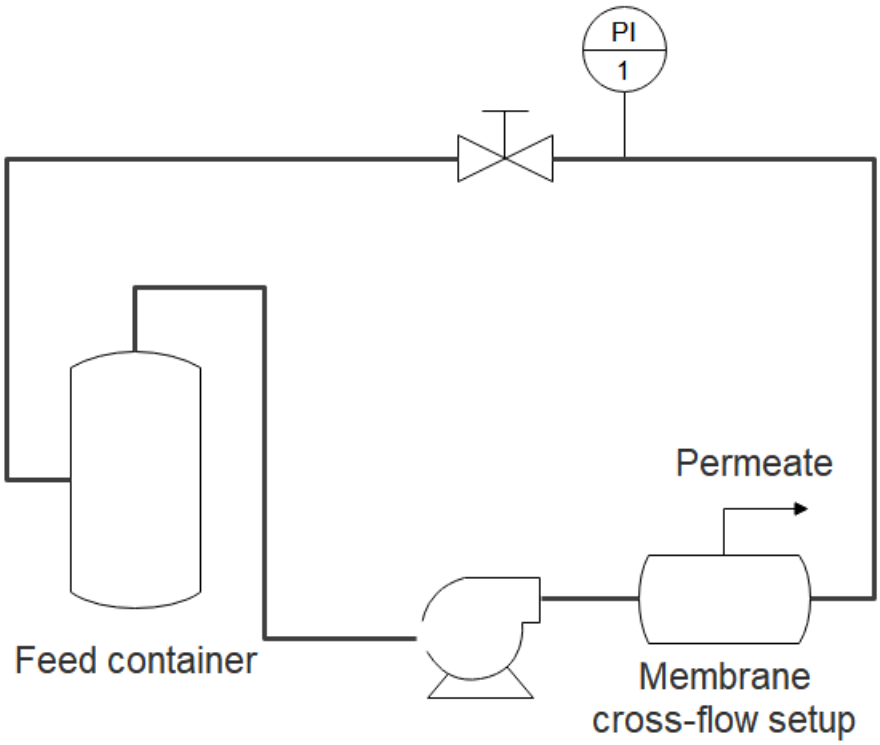

Figure 3.4 Schematic of the membrane cross-flow unit used in the on-site groundwater treatment.

CHAPTER 4. FE BASED NANOPARTICLES: FORMATION, REACTIVITY AND LONGEVITY

4.1 Overview

In this chapter, three types of nZVI based nanoparticles, such as bare Fe, sulfidized Fe (S-Fe) and palladized Fe (Pd-Fe) nanoparticles, were evaluated in reactivity, longevity and regeneration. This evaluation aims to select proper Fe based nanoparticles for the design of reactive membrane system for the degradation of chlorinated organic compounds in groundwater. The reactive membrane system is a pump and treat system: degradation reactions happened when contaminated water was pass through the membranes. The degradation performance is controlled by the time species spent inside membranes. Therefore, proper reactive particles in membrane system need both the fast reaction rate as well as the feasibility of regeneration and reuse.

In brief, Pd-Fe showed a greater degradation rate (13-20 fold) while S-Fe presented a better longevity. Regeneration of bare Fe and Pd-Fe nanoparticles were achieved using reducing agent $NaBH_4$ as well as the Fe core of S-Fe nanoparticles. However, the disappearance of sulfur species during the aging process made the S-Fe nanoparticles perform like bare Fe in terms of CTC degradation after the regeneration treatment.

4.2 Visualizing the formation of Fe, S-Fe and Pd-Fe nanoparticles

After the synthesis of precursor Fe, various dose (S or Pd) and preparation time (Table 4.1) were evaluated in the formation of S-Fe and Pd-Fe as well as the reactivity in CTC degradation. The Fe nanoparticles show a chain-like structure which was formed by multiple individual near spherical Fe nanoparticles (70 ± 20 nm) (Figure 4.1a). A core-shell structure of individual particles were also observed as a 2.5-5 nm thin oxidized shell outside the Fe core: the mole percentage of O/Fe was 5 mol% (shell, area 2) and 0.15

mol% (core, area 1), respectively (Figure 4.1d). Besides EDS mapping, the oxygen shell was also observed as a darker ring out of the bright Fe core in the high-angle annular dark-field (HAADF) mode. The lighter oxygen atoms scatter electrons less intensely than the heavier iron atoms, leading to a darker region in the HAADF mode. The darker narrow cracks found in the Fe particles (Figure 4.1b) might be the fractures on Fe particles, which could increase the surface area for reaction.

Table 4.1 Reactivity of post-prepared S-Fe and Pd-Fe at various synthesis conditions. After synthesized, [Pd/Fe] and [S/Fe] of the particles were measured using EDS. $[Fe]_{initial}$ was same for all the batches (50 ppm). $[CTC]_{initial}$ = 0.25 mM. T = 22°C.

Batches	Synthesis conditions		After synthesis	CTC degradation, residual%	
	Pd or S dose	t, min	[Pd/Fe] or [S/Fe]	after 5 min	after 120 min
Precursor Fe	N/A	N/A	N/A	0.94	0.14
Pd-Fe (A)	1 mol%	30	0.3 mol%	0.31	< 0.01
Pd-Fe (B)	10 mol%	3	1.4 mol%	< 0.01	< 0.01
Pd-Fe (C)	10 mol%	30	12.1 mol%	0.56	0.53
S-Fe (A)	20 mol%	30	1.7 mol%	0.92	0.06
S-Fe (B)	200 mol%	30	3.0 mol%	0.93	0.10
S-Fe (C)	200 mol%	300	13.9 mol%	0.98	0.29

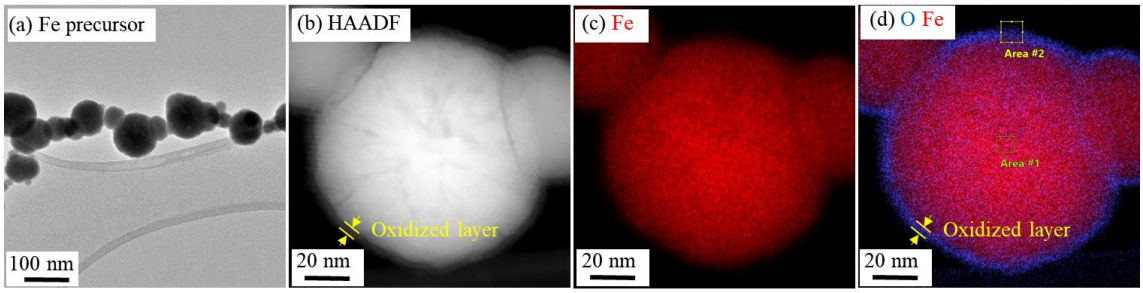

Figure 4.1 TEM characterization of initial Fe^0 nanoparticles: (a) Bright field (b) HAADF mode. EDS mapping of particles (iron in red and oxygen in blue): (c) Fe core only (d) Fe core and O shell. The chain-like structure was formed by individual near-spherical Fe^0 nanoparticles (core-shell).

The post preparation of Pd-Fe or S-Fe changed the morphology of the precursor Fe nanoparticles. As shown in Figure 4.2, the scattered formation of Pd islets was found on the surface of initial Fe nanoparticles. The formation mechanism of bimetallic Fe particles (Ni, Ag) was reported to be depended on the standard reduction potential E^0 [136]. With E^0 close to Fe, the metallic Ni was formed via sorption and reduction which tends to form hollow nanoparticles. While dendritic structures were formed for Ag-Fe bimetallic particles through rapid reduction (Ag^+/Ag has more positive E^0 than that of Fe). Since $[PdCl_4]^{2-}$ has more positive E^0 than Fe (equation 4.1 and 4.2) [137], Pd islets were rapidly formed on Fe particles via reduction reaction (equation 4.3). However, with an equal preparation time of 30 min, the higher Pd dose (10 mol% compared to 1 mol%) in preparation dramatically deformed part of the near-spherical nanoparticles to dendritic structures (Figure 4.2g to i). This structure is made by a shell of oxidized Fe and a Pd-rich core. The atomic ratio of O:Fe:Pd is 0.3:30:69.7 in the core area and 22:72.4:5.6 in the edge (Figure 4.3). The increased Pd/Fe ratio in the core area (232% compared to 7.7% in the edge) indicates the reduction of Pd prefers Fe^0-rich area, which leads to a rapid replacement of Fe in the core area (Kirkendall effect [136, 138]). Details of elemental composition of all conditions were summarized in Table 4.2.

Post preparation of Pd-Fe:

$$[PdCl_4]^{2-} + 2e^- \rightleftharpoons Pd^0 + 4Cl^- \qquad E^0 = +0.61\,V \qquad (4.1)$$

$$Fe^{2+} + 2e^- \rightleftharpoons Fe^0 \qquad E^0 = -0.44\,V \qquad (4.2)$$

$$Fe^0 + [PdCl_4]^{2-} \rightarrow Pd + Fe^{2+} + 4Cl^- \qquad (4.3)$$

Table 4.2 EDS analysis of elemental composition of Pd-Fe and S-Fe nanoparticles.

Preparation conditions	ID	Region	Element contents (atomic %)		
			O	Fe	Pd or S
1 mol%Pd-30 min	1	Edge	40	59.5	0.5
	2	Pd-rich zone	29	65.5	5.5
	3	Core	6	93.8	0.2
10 mol%Pd-3 min	1	Core	0.5	98	1.5
	2	Edge	18	79	3
	3	Pd-rich zone	0.5	44	55.5
10 mol%Pd-30 min	1	Edge	22	72.4	5.6
	2	Core	0.3	30	69.7
20 mol%S-30 min	1	Edge	49	48	3
	2	Core	10.5	89	0.5
200 mol%S-30 min	1	Edge	46.5	49	4.5
	2	Core	12	85	3
200 mol%S-300 min	1	Edge	44	36	20
	2	Core	18	77	5

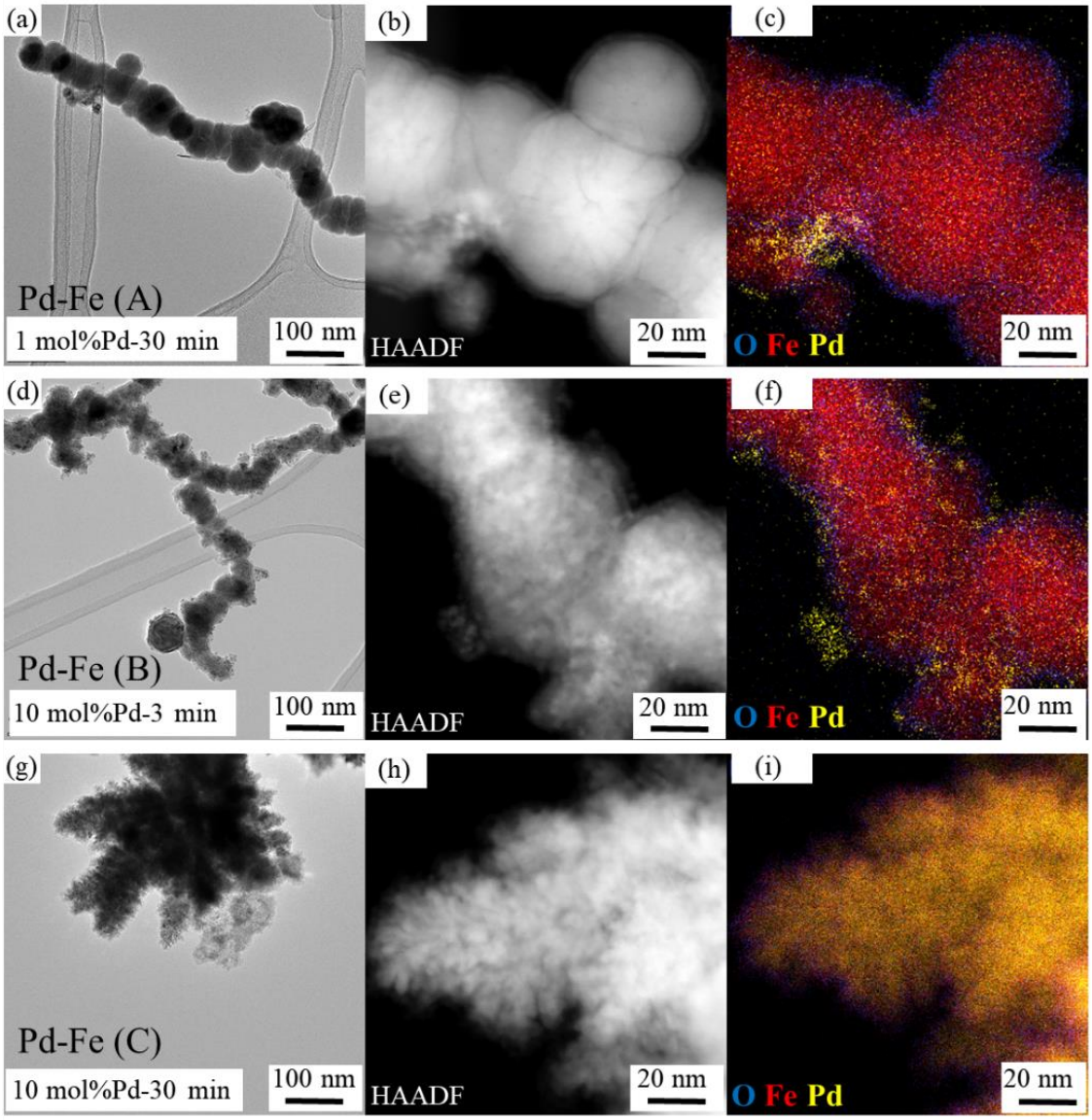

Figure 4.2 Bright field TEM imaging, HAADF imaging and EDS mappings for three types of Pd-Fe synthesized at different [Pd/Fe] and preparation time. In EDS mapping: iron in red, oxygen in blue, and palladium in yellow. The near-spherical Fe particles with Pd islets was transformed to a dendritic structure when increases Pd dose for 10-fold at the same preparation time.

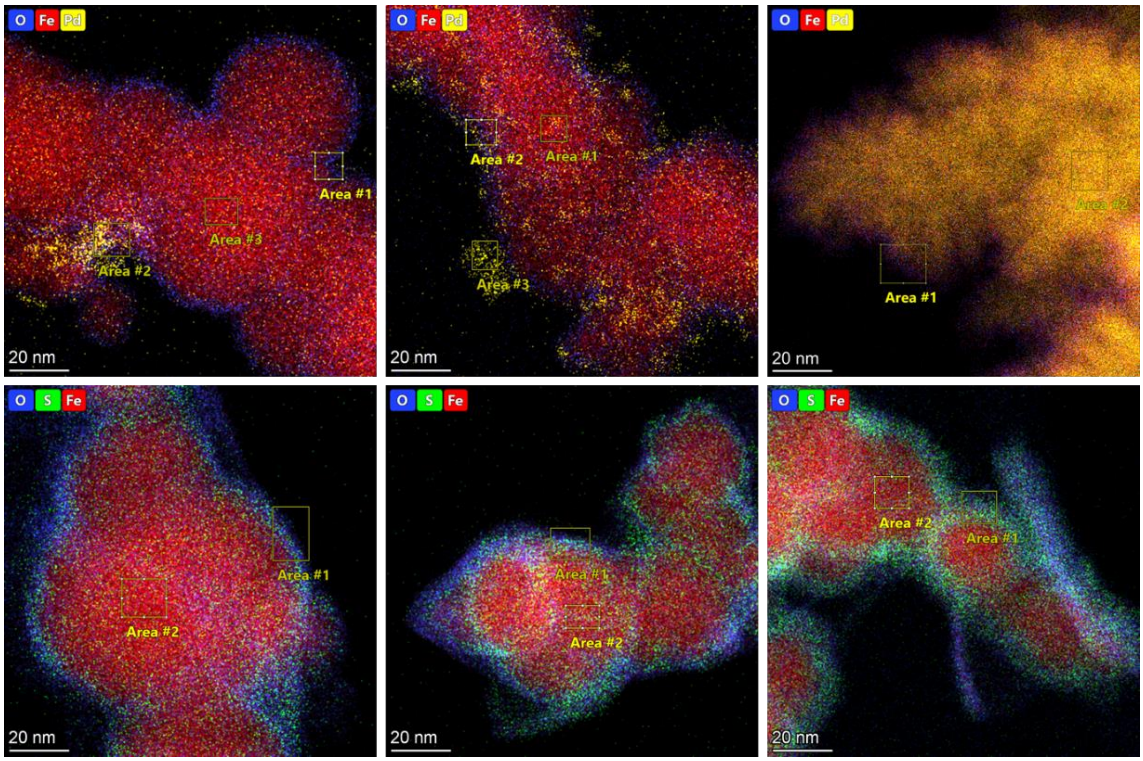

Figure 4.3 EDS mapping of various Pd-Fe and S-Fe nanoparticles. First row is Pd-Fe nanoparticles: (left) 1 mol% Pd-30 min, (center) 10 mol%Pd-3 min and (right) 10 mol%Pd-30 min. Second row is S-Fe nanoparticles: (left) 20 mol%S-30 min, (center) 200 mol%S-30 min and (right) 200 mol%S-300 min.

Rather than the significant deformation of Pd-Fe with a higher Pd dose in preparation, the formation of S-Fe was observed to be less correlated to the S dose but the preparation time. At same 30 min preparation time, a similar S shell was formed on the surface of precursor Fe nanoparticles at batches with 20 mol% S ($[S/Fe]_{shell}$ = 6.3 mol%) and with 200 mol% S ($[S/Fe]_{shell}$ = 9.1 mol%) (Figure 4.4c and f). However, a significant thicker S shell (4.5-7 nm) was observed when increases preparation time of 10-fold for the batches S-Fe(C) with 200 mol% S ($[S/Fe]_{shell}$ = 56 mol%). The details of element distribution were reported in Table 4.2. The rate-limiting step in the preparation of S-Fe is the water corrosion of Fe at neutral pH (equation 4.4), which produces Fe^{2+} to precipitate with S^{2-}. This caused a 10-53 times lower S/Fe ratio detected in particles compared to that in dosage. Furthermore, less than 0.2 atomic% of Na was detected in all synthesis conditions, which indicates a negligible adsorption and residual of Na_2S on the S-Fe nanoparticles.

The post preparation of S-Fe was achieved at neutral pH [134]:

$$Fe^0 + 2H_2O \rightarrow Fe^{2+} + 2OH^- + H_2 \uparrow \quad (\text{rate} - \text{limiting step}) \quad (4.4)$$

$$Na_2S + H_2O \rightarrow 2Na^+ + HS^- + OH^- \quad (4.5)$$

$$Fe^{2+} + 2HS^- \rightarrow FeS \downarrow + H_2S \uparrow \quad (4.6)$$

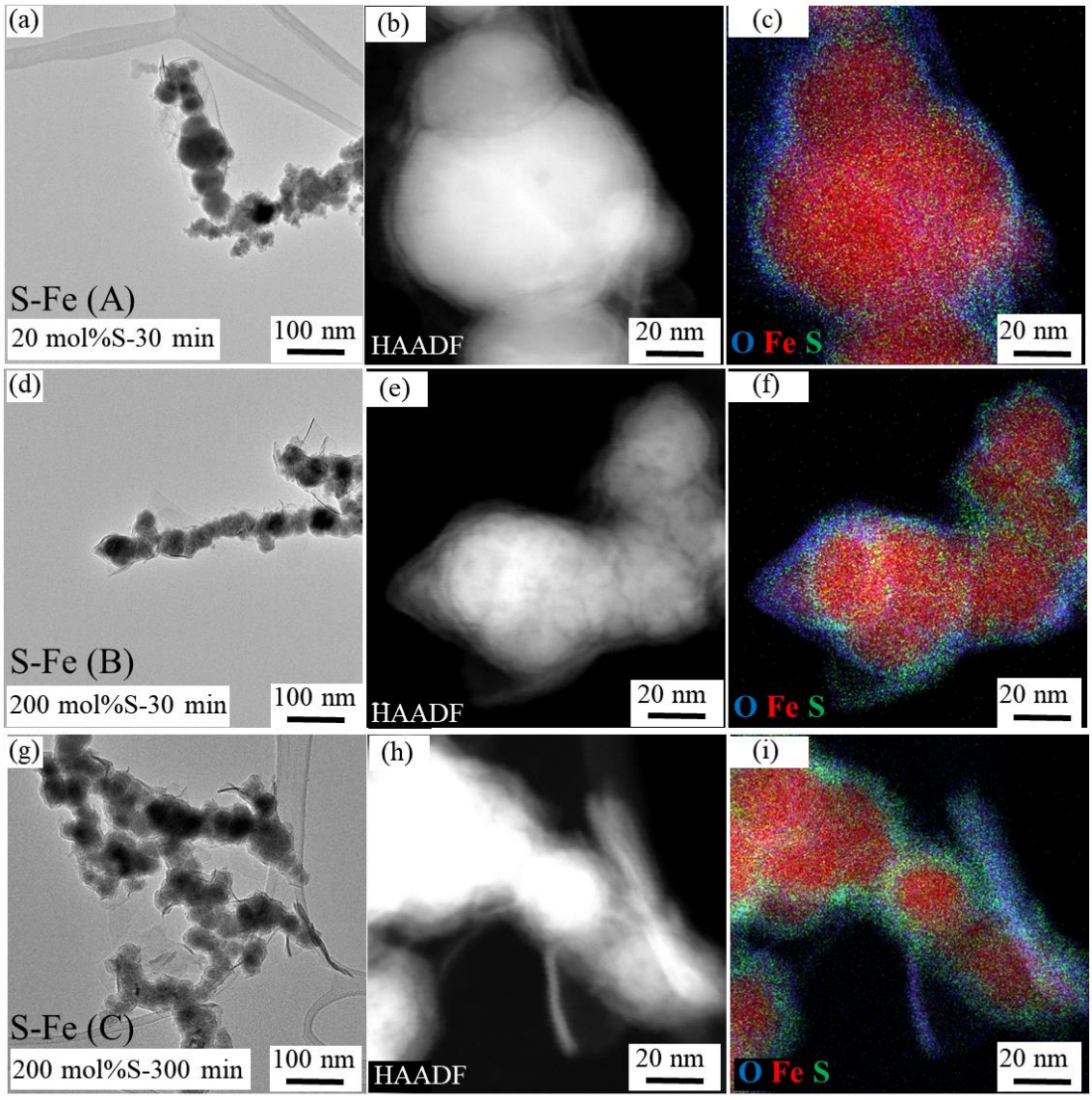

Figure 4.4 Bright field TEM imaging, HAADF imaging and EDS mappings for three types of S-Fe synthesized at different S dose and preparation time. In EDS mapping: iron in red, oxygen in blue, and palladium in yellow. Similar S layer was observed for the batches with S dose of 20 and 200 mol% at same preparation time while thicker S layers (4.7-7 nm) were formed by increasing the preparation time for 10-fold.

4.3 Correlation between particle morphology/composition and reactivity

The differences in morphology and composition significantly affected the reactivity of Pd-Fe and S-Fe nanoparticles. As shown in Table 4.1, Pd-Fe(B) (10 mol% Pd in 3 min synthesis time) and S-Fe(A) (20 mol% S in 30 min synthesis time) showed a better performance among its individual category. Through Pd served as a catalysis for H_2 hydrodechlorination, excess $[Pd/Fe]_{particle}$ was proven to decrease the production of H_2 (water corrosion of Fe) and reduction degradation [55]. The formation of dendritic structures in Pd-Fe(C) demonstrated a consumption of Fe core and a greater Pd coverage of Fe^0 surface, which leads to an insufficient H_2 production and therefore causes the insignificant hydrodechlorination degradation between 5 min and 120 min reaction time. Compared to the ineffective degradation using Pd-Fe(C), Pd-Fe(A) (with 10% Pd dose) and Pd-Fe(B) (with 10% preparation time) show more than 99% degradation of CTC within 120 min and 5 min, respectively.

For S-Fe nanoparticles, S-Fe(A) (20 mol% S dose in a 30 min synthesis time) and S-Fe(B) (200 mol% S dose in a 30 min synthesis time) show similar degradation performance. This similarity in degradation was achieved due to the similar morphology and composition of the formed particles (i.e. the correlated $[S/Fe]_{particle}$ is 1.7 atomic% and 3.0 atomic%, respectively). However, the reactivity decreased when the preparation time is increased by 10-fold (S-Fe(C), $[S/Fe]_{particle}$ = 13.9 atomic%). Excess FeS_x has been reported to decrease hydrophilicity of such particles [62] and to hinder the adsorption on metal surface [53, 139], which could eventually block the reactive sites for degradation. Mangayayam et al. show that the excessive formation of FeS_x layers (S/Fe > 10 mol%) on Fe decreased the dechlorination rate of trichloroethylene even though an increase of

reactivity was observed within the S/Fe ratio between 0-10 mol% [37]. A similar trend was also observed when S-Fe nanoparticles are stabilized using carboxymethyl cellulose [140].

Regarding the performance and cost, the batches Pd-Fe(A) and S-Fe(A) were selected for a comparison of reaction rate (Figure 4.5). CTC degradation curves could be fitted as a pseudo-first-order reaction (equation 4.7).

$$\frac{dC}{dt} = -k_{sa}\rho_m a_s C \qquad (4.7)$$

Where k_{sa} is surface area normalized reaction rate ($Lm^{-2}min^{-1}$). Since the ratio of Pd/Fe and S/Fe is minor (< 2 mol%), only the surface area of the Fe precursor was used in this calculation. ρ_m is nanoparticle loading density, which in this case is 0.05 gL^{-1}, and a_s is surface area per unit mass, which is 10.9 m^2g^{-1}. This value was calculated using average spherical nanoparticle size (~35 nm, based on the TEM characterization) and iron density (7870 gL^{-1}). In this study, only Fe surface was used for calculation.

The k_{sa} of CTC degradation followed the order of Pd-Fe (0.3 mol% Pd) >> S-Fe (1.7 mol% S) > Fe (Table 4.3). With the Pd catalyst, degradation using Pd-Fe involves an activation of produced H_2 for hydrodechlorination [51], whereas for Fe and S-Fe the H_2 production (water corrosion of Fe) is an undesirable side reaction of degradation through the electron transfer mechanism. This mechanistic difference significantly enhanced the k_{sa} of CTC degradation using Pd-Fe (13-20 fold). A 90% conversion from CTC to CF (major intermediate) was observed in all types of Fe-based nanoparticles. The formed CF was further degraded using both Pd-Fe and S-Fe. Compared to bare Fe, S-Fe was reported to limit the H_2 evolution (side reaction in degradation via electron transfer) either by decreasing the corrosion tendency [62] or by restricting hydrogen recombination reactions on H adsorption sites of particles [60, 141]. With higher usage of Fe in degradation rather

than the evolution of H_2, S-Fe, compared to Fe, shows a faster degradation rate of CTC. The FeS particles (mackinawite) were also studied (synthesized as literature [37]). Lan and Butler reported that 90% CTC was degraded after 14 days using $FeS_{mackinawite}$ ($[FeS/CTC]_{initial} = 5$) [142], however, only 12% CTC degradation was observed after 24 h reaction in this study even with a $[FeS/CTC]_{initial} = 180$ (Figure 4.5d). Hence, the reactivity of $FeS_{mackinawite}$ has a negligible contribution to the increased degradation rate using S-Fe.

Table 4.3 The surface area (Fe surface) normalized reaction rates (k_{sa}, $Lm^{-2}min^{-1}$) of CTC degradation for Fe, S-Fe and Pd-Fe ($[CTC]_{initial}$ = 0.25 mM, $[Fe/CTC]_{initial}$ = 3.6, 22°C).

Batches	[S/Fe] or [Pd/Fe] of particle	k_{sa} $Lm^{-2}min^{-1}$	R^2	Derived $t_{1/2}$ min
Fe	N/A	0.029	0.98	43
S-Fe(A)	1.7 atomic%	0.042	0.97	30
Pd-Fe(A)	0.3 atomic%	0.580	0.98	2.2

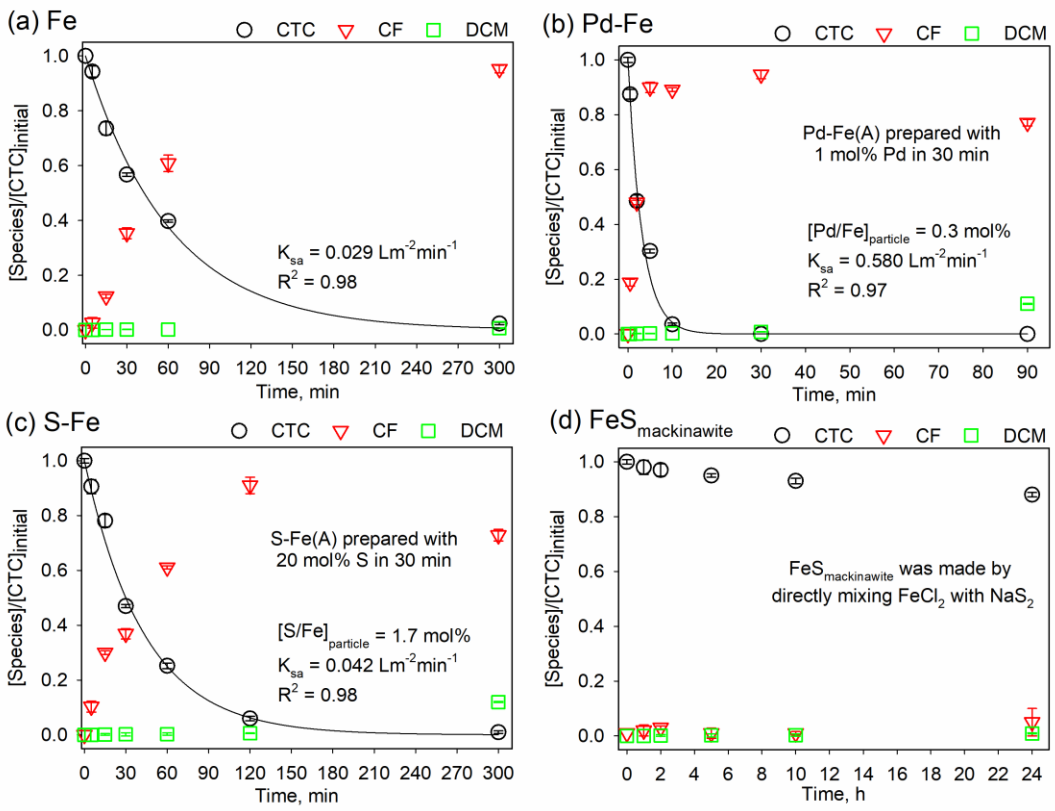

Figure 4.5 CTC degradation among Fe, Pd-Fe and S-Fe nanoparticles (with same $[Fe]_{initial}$ = 50 ppm). (a) Fe precursor (b) Pd-Fe(A) with $[Pd/Fe]_{particle}$ = 0.3 mol%, (c) S-Fe(A) with $[S/Fe]_{particle}$ = 1.7 mol%. $FeS_{mackinawite}$ particles were also tested for a comparison ($[Fe]_{initial}$ = 2500 ppm). $[CTC]_{initial}$ = 0.25 mM. T = 22°C. Abbreviation: dichloromethane (DCM), chloroform (CF) and carbon tetrachloride (CTC).

4.4 Long-term degradation and regeneration of nanoparticles

In addition to the reactivity comparison, a study of the degradation (over 31 days) and the regeneration processes (using $NaBH_4$, reducing agent) was conducted in batch mode among Fe, S-Fe and Pd-Fe nanoparticles. Within the 31-days of aging, all the particles were tested for six degradation cycles with a magnetic separation and replacement of CTC stock solution between individual cycles.

As shown in Figure 4.6, more than 99% CTC was degraded using all types of particles (Fe, S-Fe, Pd-Fe) during the first three cycles (0 to 5-days of aging). CF and dichloromethane (DCM), two major intermediates of CTC degradation) were produced and then further degraded using Fe, S-Fe and Pd-Fe. S-Fe also presented a better long-term degradation of produced CF compared to bare Fe. No obvious CTC degradation was observed for the Fe and Pd-Fe at the fourth cycle (10-days of aging), but more than 99% degradation was achieved for the S-Fe batches until the fifth cycle (17-days of aging). Herein, the S-Fe was proven to extend the longevity of bare Fe nanoparticles, which could attribute to the hindrance of the side reaction between Fe^0 and water (discussed in section 3.2).

No degradation was observed at the sixth cycle (31-days of aging) for all types of particles. Regeneration process was then achieved using $NaBH_4$ (400 mol% of $[Fe]_0$). Regenerated Fe and Pd-Fe present a similar degradation pattern compared to that when using freshly made particles. However, S-Fe performed like Fe after the regeneration process: S-Fe no longer extended longevity like the original S-Fe and was less effective in the degradation of CF.

Advanced material characterizations (TEM, XPS and XRD) were conducted during long-term study to investigate the changes of particle morphology/composition as well as to explain the loss of longevity of regenerated S-Fe. Compared to the chain-like structure observed at initial stage of Fe, S-Fe and Pd-Fe (Figure 4.7a, d, e), an agglomeration of particles was observed in all batches after 31-days of aging (Figure 4.7b, e, h) and after regeneration (Figure 4.7c, f, i). For individual particles, a transformation from near-spherical structures to thin rods, round and translucent polygons (such as square and hexagon) was also observed after aging, which could attribute to the oxidation formation of the FeOOH and magnetite (Fe_3O_4)/maghemite (γ-Fe_2O_3) [143]. As shown in Figure 4.8, the oxidation products were confirmed by observing the interplanar spacing as 0.27 nm in the area 1 (thin rod) and as 0.25 nm in the area 2 (polygons), which correspond to the (021) plane of goethite (α-FeOOH) [144] and the (311) plane of Fe_3O_4 [145], respectively. After regeneration, the near-spherical particles were recovered and the EDS analysis also show a conversion of an oxygen/iron mixed nano-rods and polygons to an oxygen shell and iron core composition (Figure 4.9). This conversion of iron oxidation products to Fe^0 leads to the restoration of reactivity of Fe and Pd-Fe nanoparticles.

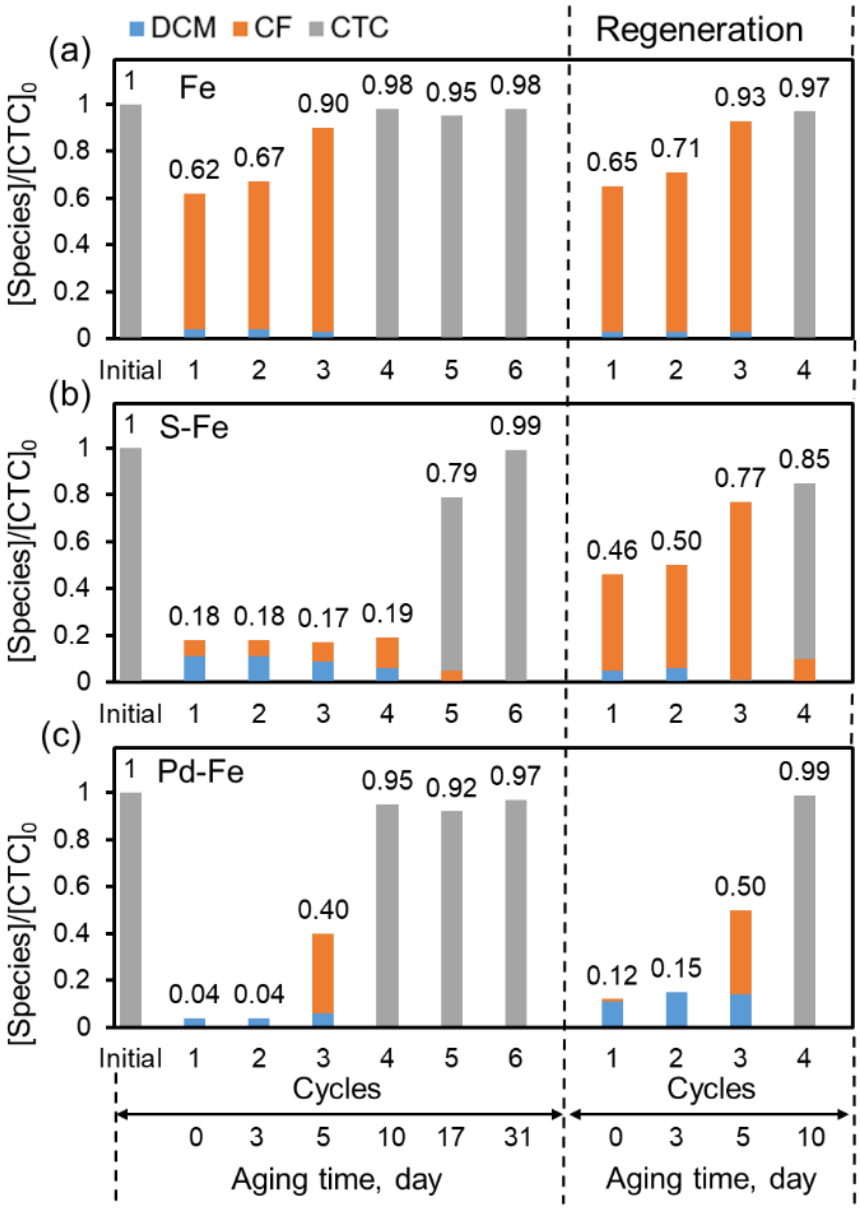

Figure 4.6 A long-term degradation study with 31-days of aging and regeneration of Fe, S-Fe ($[S/Fe]_{particle}$= 1.7 mol%) and Pd-Fe ($[Pd/Fe]_{particle}$= 0.3 mol%) nanoparticles. Same $[Fe]_{initial}$ (250 ppm) was used for all the batches. Six degradation cycles was conducted during the aging process, corresponds to the 0, 3, 5, 10, 17 and 31 days. Each cycle lasts for 24 h and a fresh stock solution of CTC was replaced between cycles. $[CTC]_{initial}$ = 0.25 mM. $[Fe]_{initial}/[CTC]_{initial}$ = 18. T = 22°C. The number above bars represents the total mass fraction of dichloromethane (DCM) chloroform (CF) and carbon tetrachloride (CTC).

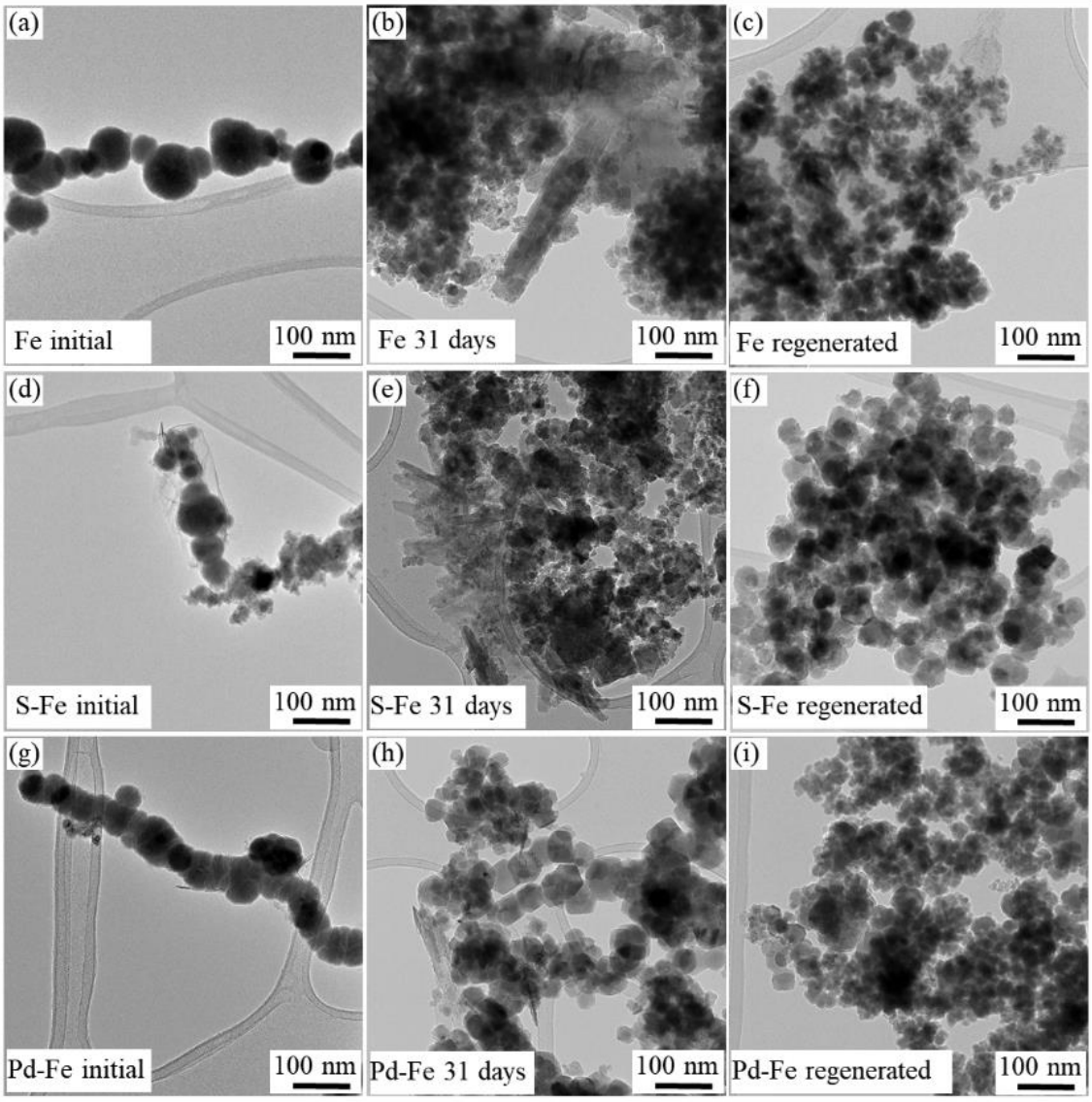

Figure 4.7 A comparison of particle morphology at three stages: initial, 31-days of aging and after regeneration. Types of particles: Fe (first row), S-Fe with 1.7 mol% S (second row) and Pd-Fe with 0.3 mol% Pd (third row). Particle agglomeration was observed during the aging process. A transformation of individual near-spherical nanoparticles to a mix of thin rods, round and translucent polygons was detected after 31-days of aging and these structures were then converted back as near-spherical particles after regeneration.

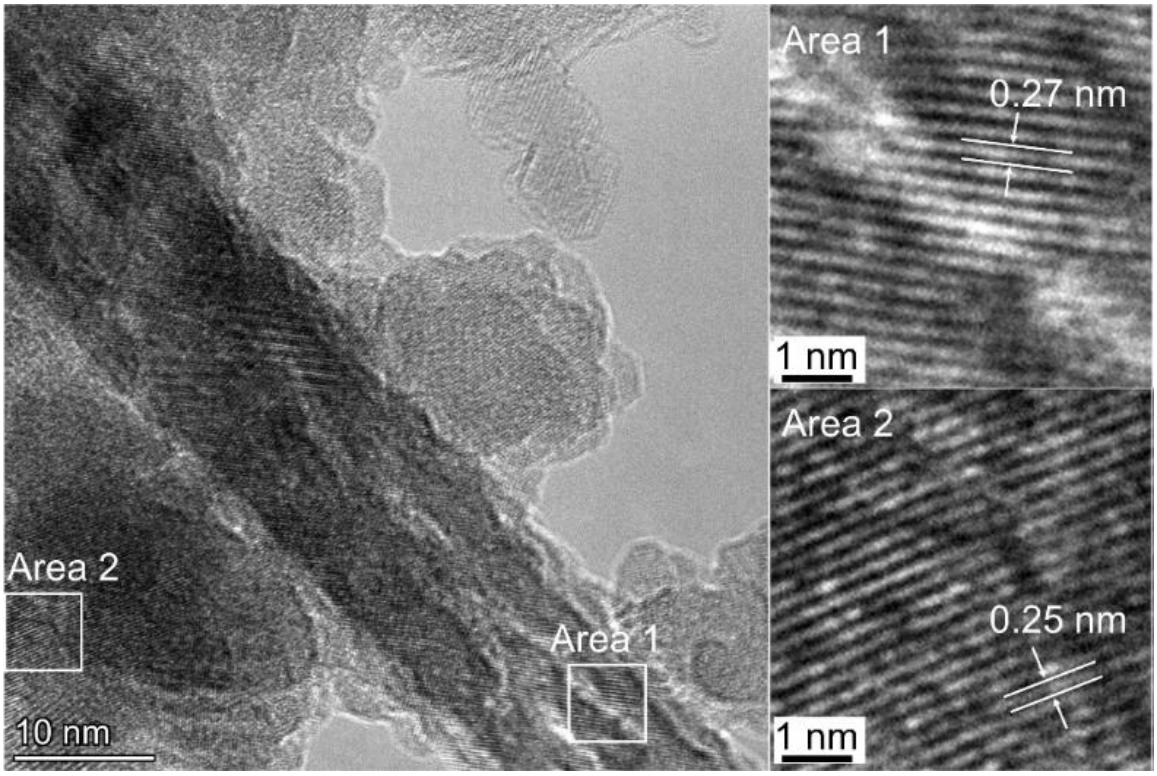

Figure 4.8 Characterization of the interplanar spacing of S-Fe (1.7 mol% S) after 31-days of aging. Two typical areas of thin rod (area 1) and polygons (area 2) were highlighted. The detected interplanar spacing of 0.27 nm and 0.25 nm corresponds to the (021) plane of goethite (α-FeOOH) and the (311) plane of Fe_3O_4, respectively.

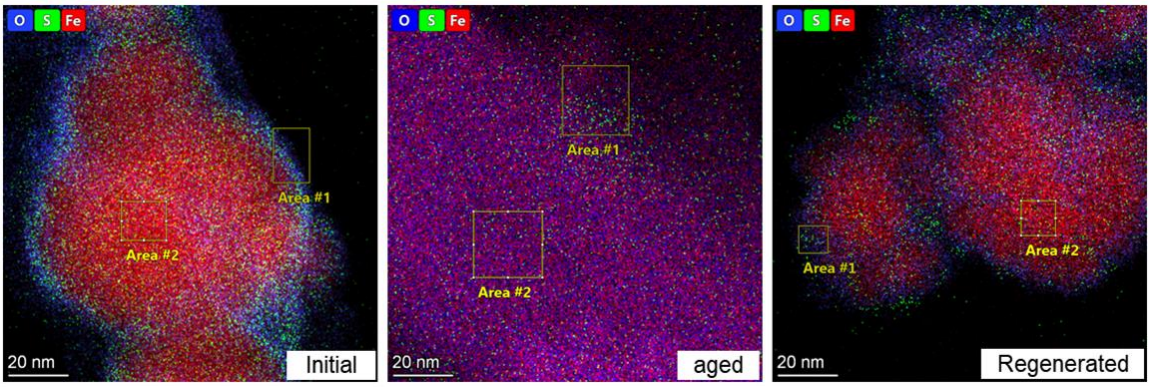

Figure 4.9 EDS mapping of S-Fe (20 mol% in 30 min) at initial, aged (31-days of aging) and regeneration stage of the long-term test. Iron in red, oxygen in blue, and sulfur in green. The [S/Fe] of marked areas was summarized in Figure 4.10.

Specific to S-Fe, Fe particles (precursor) were initially entangled by layers of thin flakes, which accounts to the formation of FeS_x [146, 147]. These thin flasks disappeared after 31-days of aging (Figure 4.7d, e) and the EDS analysis (Figure 4.9) detected a negligible S on the whole mapping area (<0.2 mol%) after aging comparing to that at initial stage (1.7 mol%) (Table 4.4). Therefore, the loss of FeS_x might be the reason that regenerated S-Fe performed just like regenerated Fe in CTC degradation after the aging and regeneration processes.

The formation of FeS_x and the loss of FeS_x during aging were both confirmed using XPS. As shown in Figure 4.10**Error! Reference source not found.**a, the scanned S 2p spectra were fit with doublets corresponding to $2p_{1/2}$ and $2p_{3/2}$. No obvious sulfur peak was observed after 31-days of aging. However, different valence states of sulfur such as disulfide (S_2^{2-}), sulfide (S^{2-}) and sulfate (SO_4^{2-}) were observed at both initial and 5-days of aging S-Fe batches (Figure 4.10b, c). This existence of SO_4^{2-} in the initial stage indicates the exposure to oxygen during preparation process and this exposure could also happen in the long-term study when the CTC solution was replaced between the degradation cycles. The oxidation of Fe sulfide minerals (mackinawite and pyrite) has been widely reported and could convert insoluble FeS/FeS_2 to soluble sulfur species such as SO_3^{2-} and SO_4^{2-} [148-151]. This oxidation conversion could lead to a decrease in sulfur content during aging which was confirmed from S/Fe atomic ratio as 49%, 25% and <0.1% corresponding to initial, 5-days of aging and 31-days of aging. Xu et al. reported the formation of 18% SO_4^{2-} at the initial stage of post-prepared S-Fe while no oxidized sulfur species (besides S_n^{2-}) was detected when S-Fe particles were prepared in a one-step method without using Fe^0 nanoparticles as a precursor. Hence, they suggest one-step prepared S-Fe has a better

stability of oxidation compared to the post-prepared S-Fe. Interestedly, they also reported post-prepared S-Fe (nano-scale, $[S/Fe]_{particle}$ = 0.8 mol%) was hydrophilic but one-step prepared S-Fe (micron-scale, $[S/Fe]_{particle}$ = 5.4 mol%) was hydrophobic. [62]. The difference in hydrophilicity might also impact the adsorption of soluble oxidized sulfur species. This lack of oxidized sulfur species in XPS analysis was also detected during the aging process of synthesized micron-scale $FeS_{mackinawite}$ (hydrophobic) [142, 152]. Therefore, the post-prepared S-Fe (with a greater hydrophilic property and nano-scale particle size), could either have a greater adsorption of soluble sulfur species or is more active for oxidation conversion.

Table 4.4 EDS analysis of elemental composition of S-Fe particles (20 mol% S dose in 30 min) during long-term study. The target regions are marked in Figure 4.9.

S-Fe batch	ID	Region	[S/Fe] atomic%	$[S/Fe]_{particle}$ atomic% whole mapping area
Initial	1	Edge	6.3	1.7
	2	Core	0.6	
31-days of aging	1	Edge	1.0	<0.2
	2	Core	<0.1	
Regeneration treatment	1	Edge	1.4	<0.2
	2	Core	0.4	

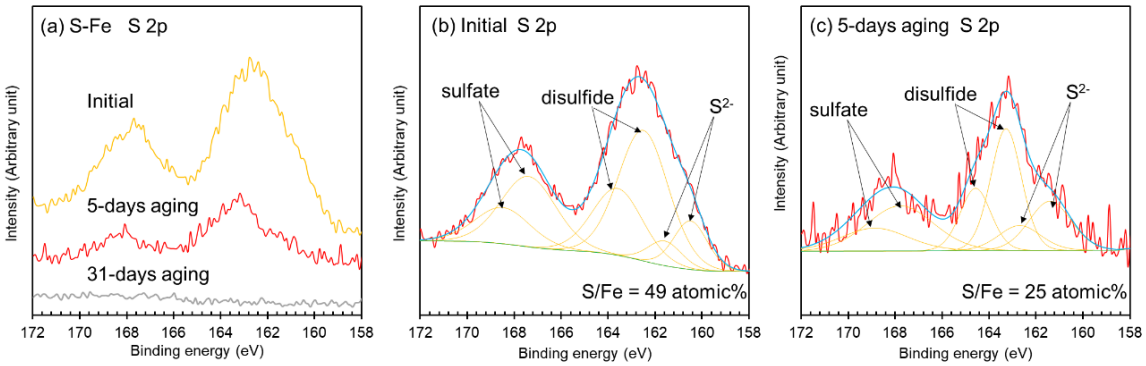

Figure 4.10 XPS analysis of S 2p spectra of S-Fe nanoparticles at initial stage (figure b), 5-days of aging (figure c). A disappearance of S spectra was observed after 31-days of aging (figure a).

XRD analysis was also conducted to identify materials. For a better XRD signal, 2.5 mol% Pd-Fe was prepared just for characterization. The diffraction peaks of Fe^0 appeared at 44.5 °, 64.9 °and 82.2 °(Figure 4.11a), correspond to the crystal planes of (110), (200) and (211), respectively (agrees with JCPDS 06-0696) [153]. These peaks were observed at the initial Fe, S-Fe and Pd-Fe particles. The peak at 40.1 °observed in Pd-Fe agrees with the major crystal plane (111) of Pd (JCPDS 05-0681) [154]. For S-Fe (Figure 4.11b), no characteristic peaks of FeS_x were detected and this phenomena has been reported [37, 155]. The explanation might be the low [S/Fe] (1.7 mol%) and the poor crystallization when FeS_x was produced at room temperature. After 31-days of aging, the characteristic peaks of magnetite (Fe_3O_4)/maghemite (γ-Fe_2O_3) (30.2 °, 35.6 °, 57.4 °, 62.8 °) were detected at all the batches [156, 157]. This correlates with the polygons observed in TEM imaging (Figure 4.7b, e, h). However, no obvious characteristic peak of FeOOH were observed, which might due to a poor crystallization [158]. Seha et al. reported the primary formation of the poorly crystalline akaganeite (β-FeOOH) during Fe^0 treatment of metolachlor, while α-FeOOH and Fe_3O_4 were detected in the similar treatment containing $FeSO_4$ [143]. Greenlee et al. also observed that lepidocrocite (γ-FeOOH) is the primary oxidation product of Fe^0 under oxygenated water [159]. These studies suggest the formation of Fe oxidation products is significant related to water conditions, such as dissolved oxygen level and various inorganic salts. Furthermore, after $NaBH_4$ treatment, the characteristic peaks of the iron oxides were disappeared and similar diffraction patterns of the initial particles were present. This conversion demonstrates the regeneration of Fe^0.

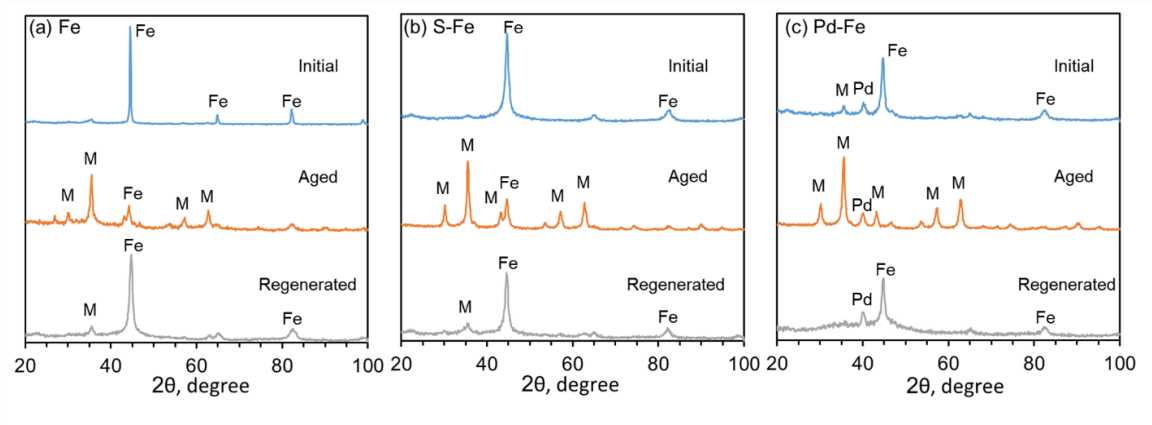

Figure 4.11 XRD analysis of (a) Fe (b) S-Fe (c) Pd-Fe nanoparticles at three stages: initial, 31-days of aging and after $NaBH_4$ regeneration. Marks of characteristic peaks: Fe^0 (Fe), magnetite (Fe_3O_4)/maghemite (γ-Fe_2O_3) (M) and palladium (Pd). The emergence of peaks of Fe_3O_4/γ-Fe_2O_3 demonstrated the oxidation of Fe0, while these peaks were disappeared with the rising of Fe^0 peaks after reductive regeneration.

CHAPTER 5. ROLES OF H_2 EVOLUTION AND PARTICLE PROPERTIES IN PCB REMEDIATION

5.1 Overview

Due to the fast degradation rate and feasibility in regeneration, Pd-Fe nanoparticles were selected to be incorporated with membrane domains for the treatment of chlorinated organic compounds. In this chapter, both the particle properties (Pd fraction and particle composition) and water conditions (pH, temperature) were evaluated in the degradation treatment of 2-chlorobiphenyl (PCB-1). In short, excessive Pd coverage (>5.5 wt%) on Fe nanoparticles hindered the production of H_2 (water corrosion of Fe), which leads to the insufficient H_2 for hydrodechlorination of contaminants. In addition, the degradation rate of four target contaminants in groundwater (chloroform, carbon tetrachloride, trichloroethylene and tetrachloroethylene) were measured respectively using Pd-Fe. The degradation rate follows the order of carbon tetrachloride > trichloroethylene > tetrachloroethylene > chloroform.

5.2 Effects of Pd fraction and particle compositions

The dechlorination of PCB-1 by Pd-Fe nanoparticles can be described as equation 5.1 to 5.3. As a catalyst, an increase of the amount of Pd can accelerate the dechlorination reaction under sufficient H_2 condition, such as Pd particles under a H_2 stream [160-162] . However, when the corrosion of Fe is the source for H_2, excessive Pd coverage on Fe could reduce the exposed Fe for H_2 production, leading to a decrease in the dechlorination rate. In Figure 5.1b, a tradeoff between increasing Pd fraction and H_2 production was observed for a same source of Fe. Tee et al. reported the study with Ni/Fe bimetallic particles and they also found a 10-fold decrease in H_2 generation with an increase of Ni content from 20% to 75% [163]. For ease of comparison, H_2 production was normalized to the batches

with 0% Pd. Based on the GC analysis, nearly 51.2×10^{-7} mol hydrogen was produced by the 0 wt% Pd batches at 10 min interval. Stoichiometrically, the complete dechlorination of 1.1×10^{-7} mol PCB-1 to biphenyl requires 0.55×10^{-7} mol H_2. In results, 0.61×10^{-7} and 0.46×10^{-7} mol H_2 were produced at the 5.5 and 12 wt% Pd batches, respectively. Insufficient H_2 was produced at the 12 wt% Pd batches, leading to a less dechlorination compared to the batches with 5.5 wt% and even 0.5 wt% Pd.

The production of H_2 by the corrosion of Fe^0 in water [164]:

$$Fe^0 + 2H_2O \rightarrow Fe^{2+} + H_2 \uparrow + 2OH^- \quad (5.1)$$

The formation of atomic hydrogen and the dechlorination of PCB-1 [59, 165]:

$$H_2 \uparrow \overset{Pd}{\rightarrow} 2H* \quad (5.2)$$

$$C_{12}H_9Cl\ (PCB\ 1) + 2H* \rightarrow C_{12}H_{10}\ (biphenyl) + H^+ + Cl^- \quad (5.3)$$

For the formation of Pd-Fe nanoparticles, the Pd^{2+} ions were reduced by metallic Fe and a layer of Pd islets was then formed on the surface of Fe [166, 167]. Therefore, a theoretical Pd surface coverage could be estimated by assuming a uniform distribution of the Pd monolayer on the surface of Fe [168]. Based on XRD studies, the Pd layer was found to be predominantly in the lowest energy face-centered cubic (fcc) (111) crystallographic orientation (Figure 5.1a). Since each fcc (111) plane contains two Pd atoms, the surface area of single atom in the fcc (111) unit cell is calculated as:

$$Surface\ Area\ of\ Single\ Atom\ in\ Unit\ Cell, nm^2 = \frac{0.5 \times 2\sqrt{3}r \times 4r}{2} = 2\sqrt{3}r^2 \quad (5.4)$$

Where, r is the radius of a palladium atom (0.138 nm). According to the observed diameter of Fe particles in TEM, the loading of a full Pd monolayer coverage on the Fe surface was derived as 53 wt% of Fe. In experiments, the Pd contents as 0.05, 0.5, 2, 5.5,

12 and 50 wt% of Fe correspond to 0.1, 1.0, 3.8, 10.4, 22.6, 94.3% Pd coverage on Fe surface, respectively. At a low surface coverage (< 10.4%, corresponding <5.5 wt%), an increase of dechlorination and a decrease of H_2 production were observed with increasing Pd coverage. This observation indicates, when sufficient H_2 is produced at low Pd coverage (coverage from 0% to 10.4%, corresponding to 0 wt% to 5.5 wt%), the amount of catalyst Pd was the rate-limiting factor for the dechlorination reaction. However, H_2 production was observed to be the rate-limiting factor at higher Pd surface coverage (10.4 to 94.3%, corresponding to 5.5 wt% to 50 wt%). No significant production of H_2 was found for the 50 wt% batches, which correspond to a nearly 95% Pd coverage on the individual Fe particles. Overall, the batches with Pd percentages from 0.5 wt% to 5.5 wt% (1.0% to 10.4% Pd coverage) yielded higher dechlorination performance.

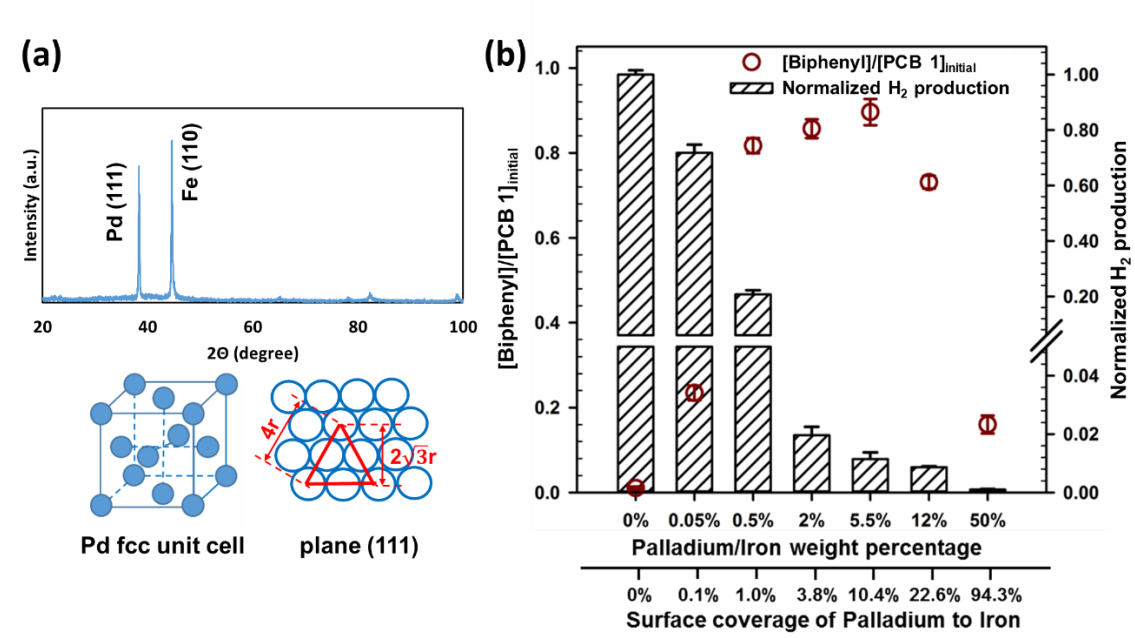

Figure 5.1 (a) XRD analysis of Pd/Fe bimetallic particles (>100 nm particles were synthesized specifically for XRD analysis). (b) Solution phase studies of the effects of Pd contents (validated using ICP) on both the dechlorination and the H_2 production (CMC is 0.5 wt%, [Fe] = 500 ppm, $[PCB\text{-}1]_o$ = 5 ppm. Reaction time 10 min. T = 23 °C, pH = 7.8). The H_2 production at various Pd contents was normalized with the H_2 production at 0% Pd batches, which was measured as 51.2×10^{-7} mol. The mass balance between unreacted PCB-1 and produced biphenyl was achieved above 90% for every batch.

The composition of the nanoparticles, either palladized-Fe bimetallic or isolated Pd and Fe particles, is another important factor for dechlorination rate. As shown in Figure 5.2a, with 0.5 wt% Pd and a same Fe source, the palladized-Fe batches presented a significantly higher reaction rate (observed rate constant k_{obs} = 0.173 min^{-1}) than the isolated Pd and Fe batches (k_{obs} = 0.009 min^{-1}, Pd particle size ~4.5 nm (Figure 5.3a). Even when 24-fold more Pd was added as isolated particles (12wt% Pd), the reactivity (k_{obs} = 0.014 min^{-1}) was nearly 12-fold lower than the palladized-Fe batches with only 0.5 wt% Pd. The isolated batches were observed to have insignificant effect on H_2 production (Figure 5.2b) which means sufficient H_2 was produced in the batches with isolated Pd and Fe nanoparticles. The formation of Pd islet on the Fe surface (Figure 5.3b) enhances the specific surface area of the Pd catalyst compared to that of the Pd particles formed on the isolated Pd and Fe batches. The larger specific surface area contributes to a higher reaction rate for the palladized-Fe particles. Furthermore, the palladized-Fe is more favorable for the diffusion of produced H_2 to the reactive sites on Pd islets, which could increase the formation of atomic hydrogen for dechlorination.

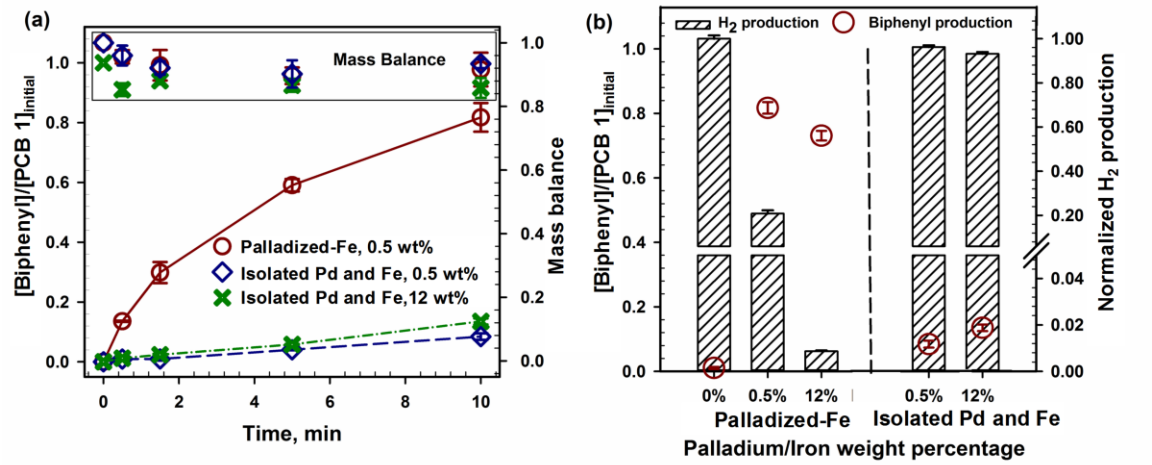

Figure 5.2 The effects of the particle composition (either palladized-Fe bimetallic or isolated Pd and Fe nanoparticles) on dechlorination (figure a) and H_2 production (figure b). This study conducted in a solution phase (CMC is 0.5 wt%, [Fe] = 500 ppm, $[PCB\text{-}1]_o = 5$ ppm. T = 23 ^oC, pH = 7.8). The H_2 production at different Pd contents, in 10 min, was normalized with the production at 0% Pd batches.

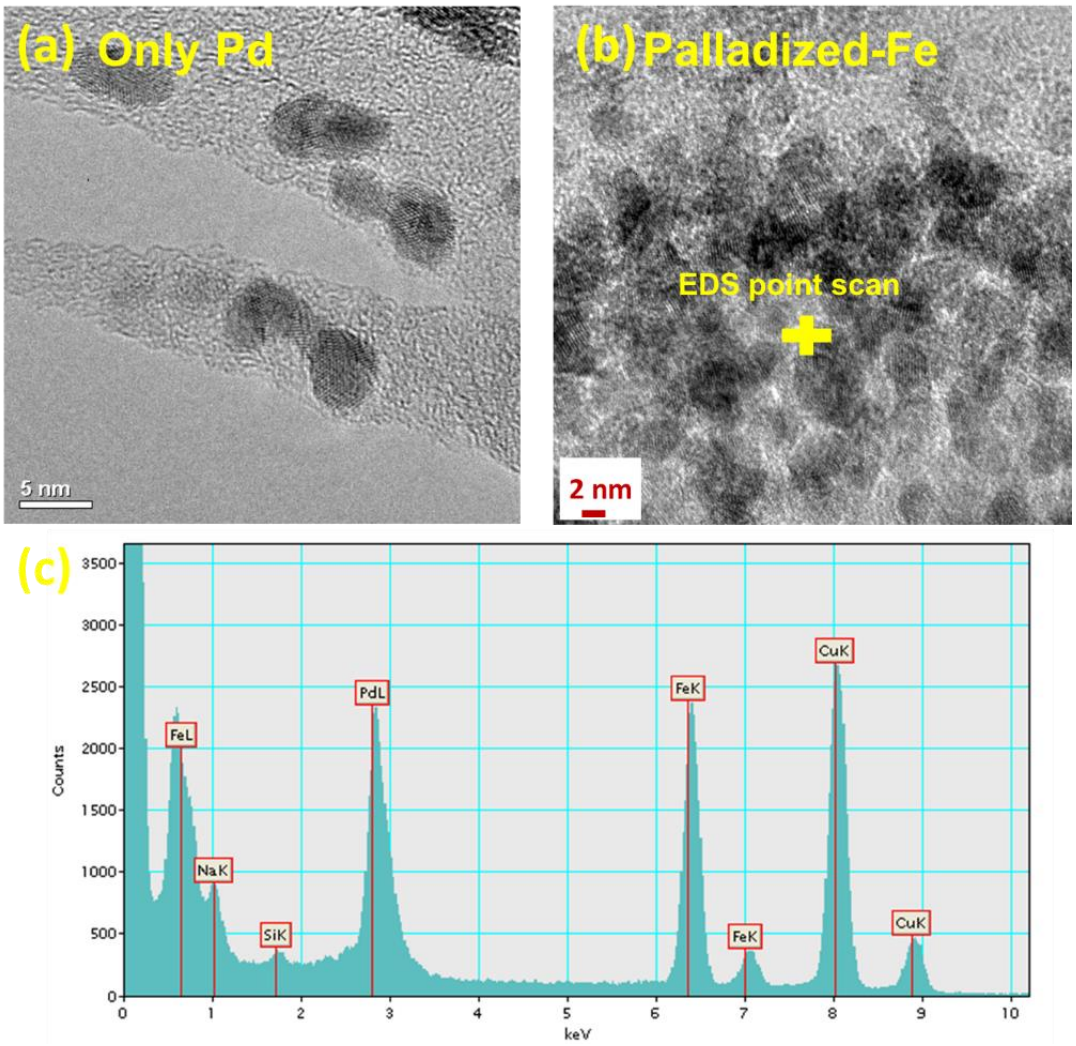

Figure 5.3 TEM images of Pd (figure a) and Pd/Fe bimetallic (Pd was 50 wt% of Fe, figure b) particles. 0.5 wt% CMC used as stabilizer. (c) EDS scan of the edge on the bimetallic particle.

5.3 Effects of pH and temperature in PCB-1 dechlorination

Environmental pH can impact the longevity of bimetallic particles and dechlorination performance [57, 169]. In acidic condition, the H_2 produced via corrosion of Fe occurs more readily and thus provides more H_2 for Pd activation. In alkaline conditions, a surface passivation occurs via iron hydroxide precipitation, resulting in the formation of passive surface layer that can deactivate Pd/Fe particles [170].

The solution pH was proven to have a significant impact on PCB-1 dechlorination (Figure 5.4a). The initial pH of PCB-1 solutions was adjusted to be 3.5, 7.8 and 9.2, respectively, by adding H_2SO_4 or NaOH. No buffer solutions were added to prevent any effects of buffers on corrosion of Fe [171]. After the dechlorination reaction, the water corrosion of Fe caused slight changes on pH [169], which resulted in pH values of 3.6, 8.1 and 9.3, respectively. In Figure 5.4a, the higher initial dechlorination rate was observed at pH 3.5 batches. A discoloration (from black to pale green) was observed for the pH 3.5 samples after 1.5 min, which indicated the dissolution of Fe particles. Even though the lower pH batches showed the faster initial dechlorination rate, they eventually produced less biphenyl than the batches at pH 7.8 and 9.2. A positive correlation between the acidic condition and overall dechlorination performance was reported for the similar Pd-Fe bimetallic systems [171, 172]. However, the size and concentration of the bimetallic nanoparticles are important to consider and could potentially reduce dechlorination performance. The negative correlation with the acidic condition and dechlorination performance in this study could be explained as following: (1) extensive and rapid H_2 production could form gas bubbles around the reaction sites which inhibits dissolved-phase contact with target pollutants [169, 173]; (2) Fe could be rapidly consumed when the

produced H_2 is not able to efficiently activated as reactive atomic hydrogen [174]; and (3) the loss of Pd islets on Fe surface caused by the rapid erosion of Fe base [57, 173].

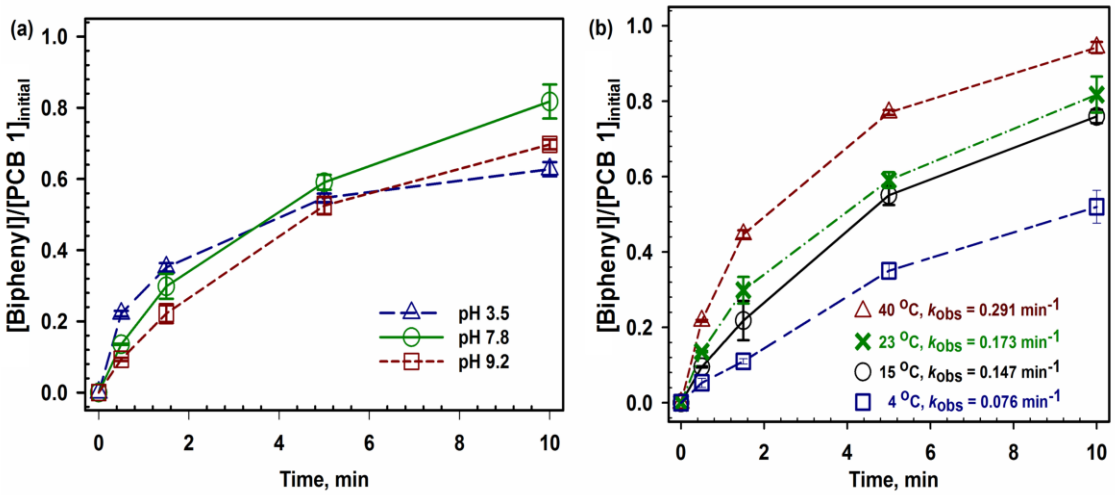

Figure 5.4 Effects of pH and temperature conditions on dechlorination performance in solution phase studies (CMC is 0.5 wt%, [Fe]=500 ppm, Pd was 0.5 wt% of Fe, $[PCB\text{-}1]_o$= 5 ppm). (a) The initial pH 3.5, 7.8 and 9.2 were converted to 3.6, 8.1 and 9.3, respectively. T = 23 ^oC. (b) Based on the Arrhenius equation, the activation energy of PCB-1 dechlorination was obtained as 26.5 kJ/mol. The initial pH = 7.8.

To better understand the mechanism of the PCB-1 dechlorination reaction, kinetic studies were investigated to evaluate the activation energy (Ea, kJ/mol). As shown in Figure 5.4b, a higher temperature had a positive effect on the dechlorination (mass balance was achieved above 90% for every batches). The k_{obs} under temperatures of 4, 15, 23 and 40 ^{o}C were calculated as 0.076, 0.147, 0.173 and 0.291 min^{-1}, respectively. The activation energy for the degradation of PCB-1 by Pd-Fe nanoparticles was evaluated by the Arrhenius equation:

$$k_{obs} = A \times \exp(-E_a/RT) \qquad (5.5)$$

where k_{obs} is the observed first-order rate constant (min^{-1}), A is the frequency factor, E_a is the activation energy, R is the ideal gas constant, and T is the absolute temperature. Figure 5.5 shows the plot of 1/T versus the natural logarithm of rate constants for PCB-1 degradation using Pd-Fe nanoparticles.

With 0.5 wt% Pd, the activation energy was found to be 26.5 kJ/mol. According to calculated activation energy, the consistency of dechlorination results between the experimental and predicted data was found and shown in Figure 5.6. Fang and Al-Abed reported the activation energy for PCB-1 dechlorination between 17 to 20 kJ/mol from 4 to 60 ^{o}C using Pd-Fe nanoparticles (Pd was 0.585 wt% of Fe). They found an insignificant relation between the observed dechlorination rates and the initial concentration of PCB-1, which suggests the overall rate is limited by the adsorption [175]. Xu et al. reported Ea = 24.5 kJ/mol for the dechlorination of 2,2'-dichlorobiphenyl by membrane-supported Pd-Fe nanoparticles suggesting a diffusion-controlled reaction [176]. An Ea of 29 kJ/mol was reported for PCB-77 dechlorination at 25 and 40 ℃ in a Pd-Fe nanotubes system, which indicates the shape of the catalyst has some pivotal role in reaction mechanism [177]. The

effect of the shape of particles on activation energy was reported considering tetrahedral, cubic and near spherical particles in solution phase [178].

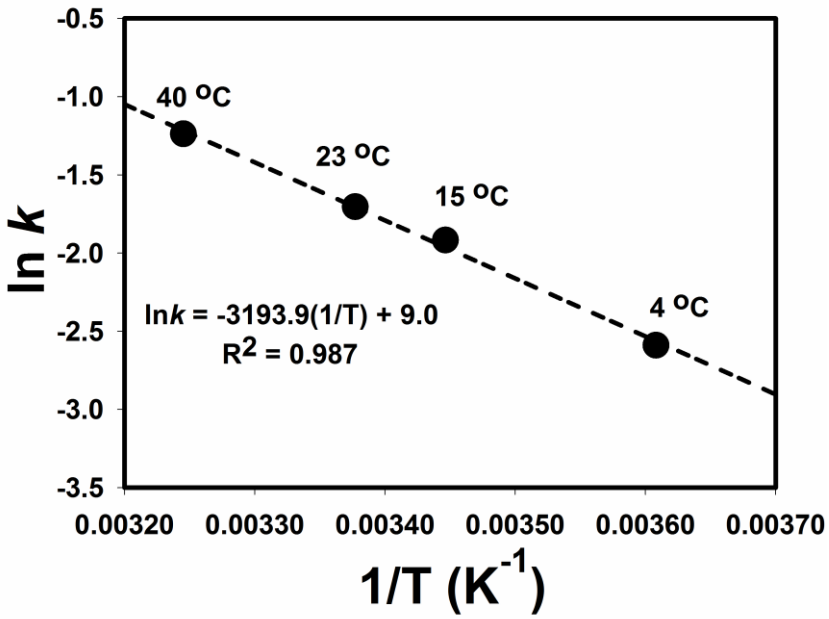

Figure 5.5 The linear fit of E_a for the dechlorination of PCB-1 with Pd/Fe bimetallic (CMC is 0.05 wt%, Pd is 0.5 wt% of Fe) particles at various temperatures.

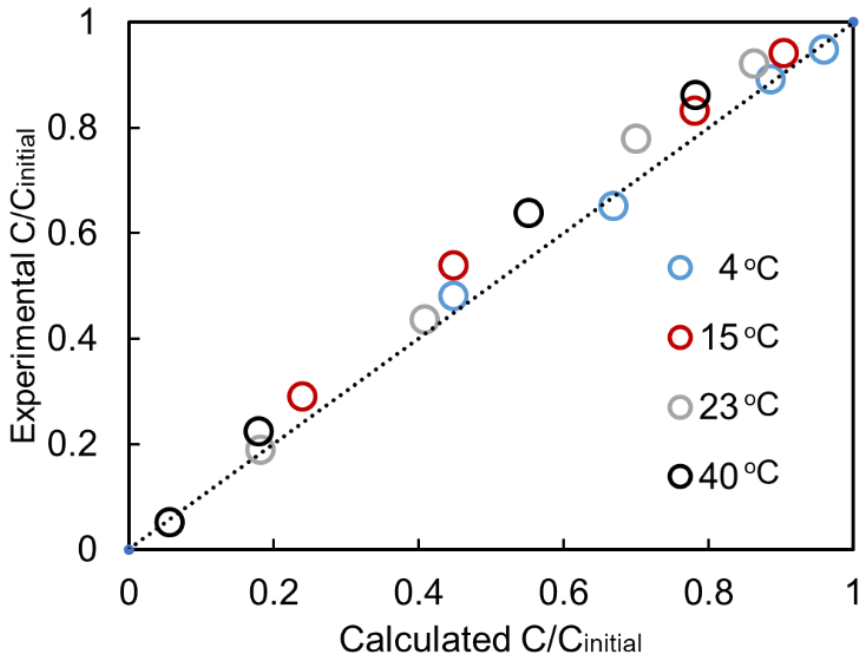

Figure 5.6 The comparison between PCB-1 dechlorination data and the prediction data with the derivate activation energy.

5.4 Kinetic studies of target chlorinated organic compounds

Four major chlorinated organic contaminants, i.e., chloroform (CF), carbon tetrachloride (CTC), trichloroethylene (TCE) and tetrachloroethylene (PCE), were treated respectively using Pd-Fe. To compare the kinetics, similar initial concentration of individual species (0.23-0.25 mM) was made separately in DI water and a same $[Fe/Species]_{initial}$ was applied for degradation tests. As shown in Figure 5.7, the degradation curves of these four species were well fitted with the pseudo first order reaction. Therefore, the half-life and the surface area normalized reaction rate (ksa) were derived and summarized in Table 5.1. The degradation rate follows the order of CTC > TCE > PCE > CF.

Table 5.1 The surface area normalized reaction rate of different species. The degradation studies were conducted using Pd-Fe nanoparticles ([Fe] = 50 ppm, 0.5 wt% Pd of Fe, average size: 35 nm). All the degradation reactions fit the pseudo first order reaction and the half-life ($t_{1/2}$) was also derived accordingly.

Species	mM	[Fe]/[Species]	k_{sa}, $Lm^{-2}min^{-1}$	R^2	Derived $t_{1/2}$ min
Chloroform (CF)	0.24	3.7	0.005	0.95	239
Carbon tetrachloride (CTC)	0.25	3.6	0.580	0.97	2.2
Tetrachloroethylene (PCE)	0.23	3.8	0.073	0.98	17.3
Trichloroethylene (TCE)	0.24	3.7	0.152	0.97	8.4

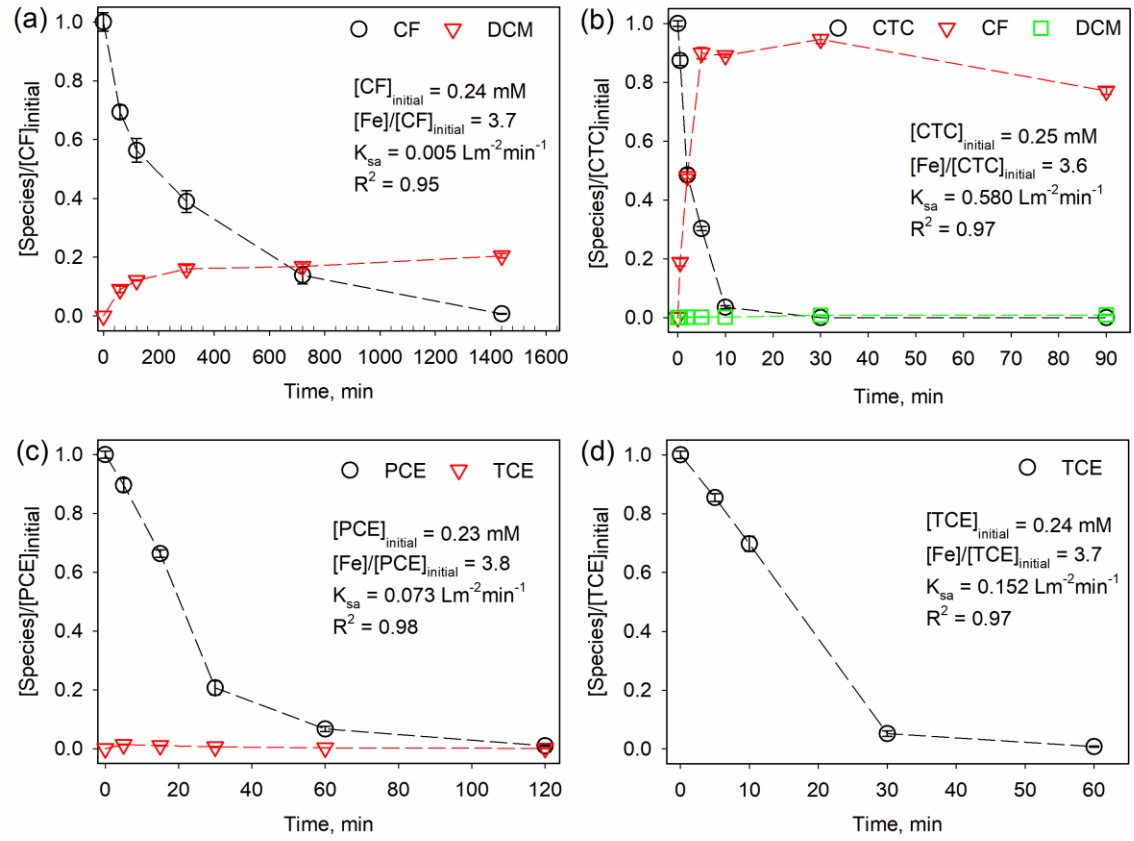

Figure 5.7 The degradation studies of four target compounds were conducted using Pd-Fe nanoparticles ([Fe] = 50 ppm, 0.5 wt% Pd of Fe, average size: 35 nm in radius, T = 22ºC). All the degradation reactions fit the pseudo first order reaction and surface area normalized reaction rate was also derived accordingly.

CHAPTER 6. INTEGRATION OF REACTIVE PD/FE NANOPARTICLES AND MEMBRANES

6.1 Overview

The reactive Pd-Fe nanoparticles were evaluated in the degradation of different toxic chlorinated organic compounds, as well as tested under various water conditions. In this chapter, poly(acrylic acid) or poly(methacrylic acid) (PAA or PMAA) functionalized polyvinylidene fluoride (PVDF) membranes were synthesized for the intergradation of reactive Pd-Fe nanoparticles. Advanced material characterization was also applied to test the particle properties inside the pores of membranes.

6.2 Properties of responsive PMAA or PAA functionalized PVDF membranes

The successful polymerization of PAA or PMAA (validated by ATR-FTIR analysis in Figure 6.1) changed the properties of the pre-hydrophilized commercial PVDF membranes, such as contact angle, thickness, permeability, etc. (Table 6.1). The in-situ polymerization was observed to decrease the pore size of the original PVDF membranes (Figure 6.2). Due to the ionization of the carboxyl group, the PAA or PMAA chains swell when the solution pH > pKa of PAA or PMAA, which was reported as 4.3-4.7 and 4.6-4.8, respectively [179-181]. A greater pH (>pKa) was found to decrease the membrane pore size and permeability, and vice versa. For example, the permeability ($Lm^{-2}h^{-1}bar^{-1}$, LMH/bar) of the PMAA functionalized membranes (12.1 wt%) were measured as 543 ± 4, 86.3 ± 3.6 and 18.2 ± 0.5 at pH 2.3, pH 5.5 and pH 10.5, respectively (Figure 6.3). The permeability at pH 2.3 was measured at 0.34, 0.69 and 1.03 bar and the permeability at pH 5.5 and pH 10.5 were measured at 1.72, 3.45 and 5.17 bar. A reversible permeability at different pH was also observed (responsive behavior in flux). The permeability decreased with an increase of pH and recovered after the pH adjusted back to the lower value.

Table 6.1 Properties of pristine and PAA or PMAA functionalized PVDF membranes (1 mol% initiator and 1 mol% cross linker).

Membrane	Pore size (nm)	Mass gain (%)	Thickness (μm)	Contact angle (°), pH 5.5	Permeability (LMH/bar) (pH 2.3)	Permeability (LMH/bar) (pH 10.5)
Pristine	279.8 ± 68.6	N/A	170.2 ± 4.1	81.3 ± 1.9	6611 ± 55	6589 ± 57
PAA	49.8 ± 24.1	13.1	173.8 ± 3.2	52.5 ± 3.9	16.4 ± 1.2	3.5 ± 0.4
PMAA	121.2 ± 35.4	12.1	172.4 ± 2.4	54.1 ± 2.3	543 ± 4	18.2 ± 0.5

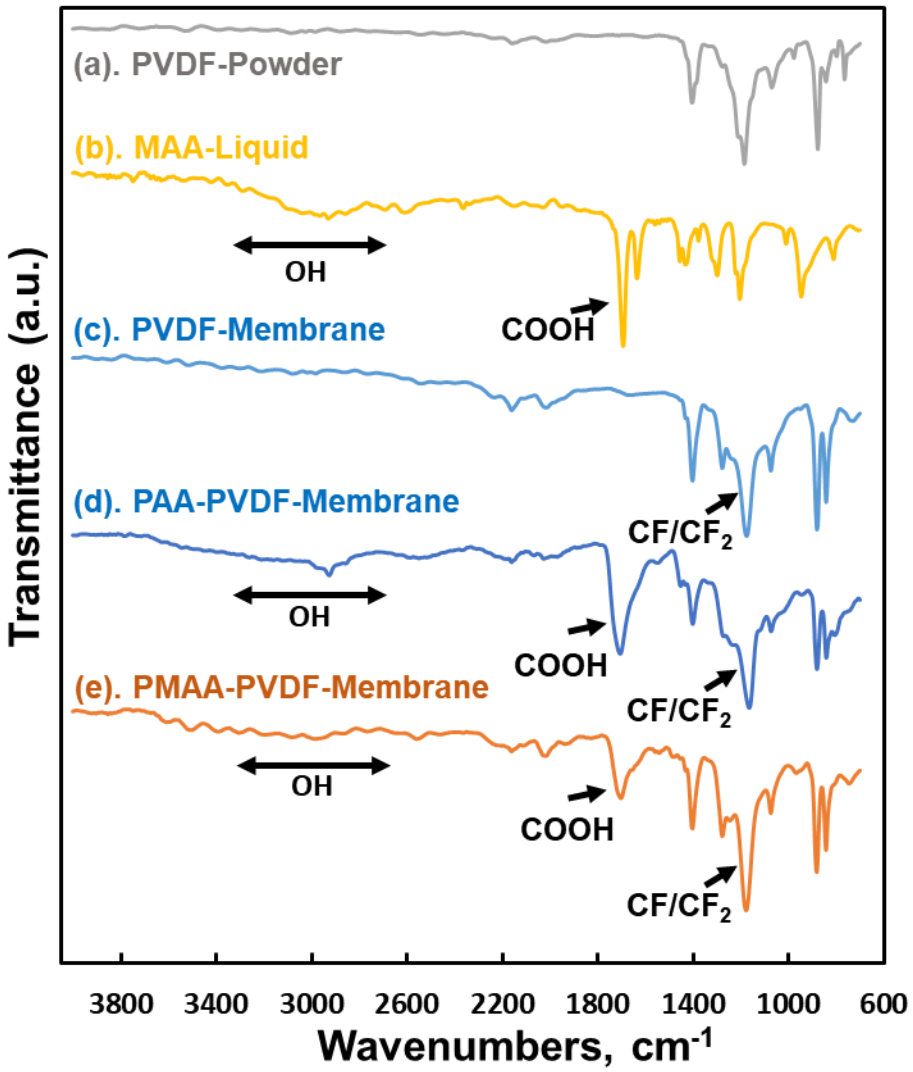

Figure 6.1 ATR-FTIR analysis of (a) PVDF powder, (b) methacrylic acid powder, (c) original PVDF 700 membrane, (d) PAA-PVDF 700 membrane and (e) PMAA-PVDF 700 membrane, respectively.

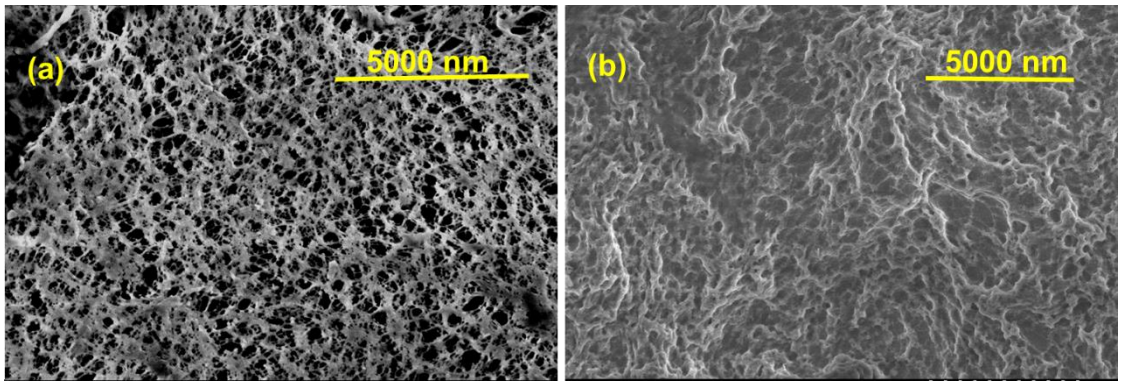

Figure 6.2 SEM image of (a). Pristine PVDF 700 membrane (Solecta, Inc) and (b). PAA-PVDF 700 membrane (13.1 wt% PAA, 1 mol% initiator and 1 mol% cross-linker).

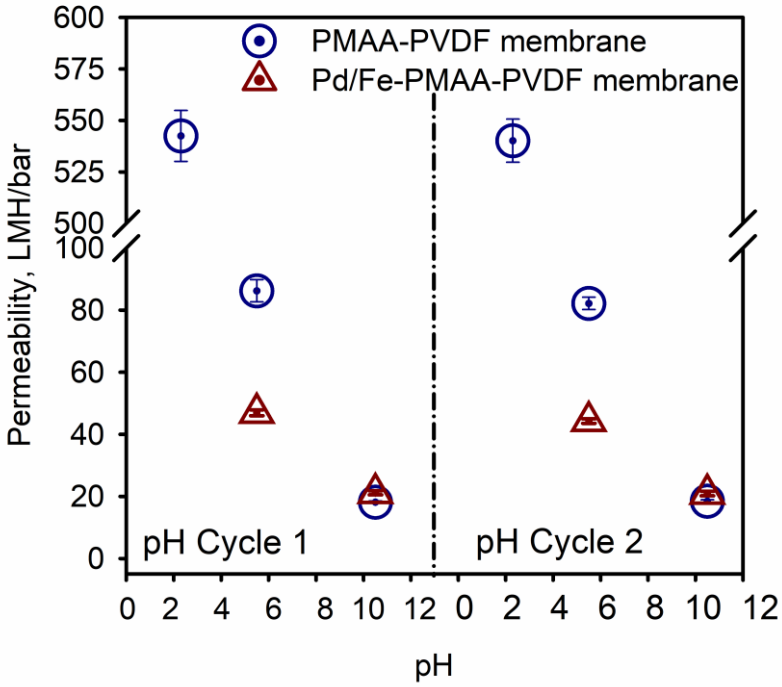

Figure 6.3 The pH-responsive permeability of two types of functionalized PVDF membranes (Solecta PVDF 700): (1) 12.1 wt% PMAA-PVDF membranes and (2) Pd-Fe particles incorporated PMAA-PVDF

This pH responsive behavior was also observed during the measurement of contact angle (Figure 6.4). The membrane pieces were immersed at different pH and then dried under a nitrogen flow before the measurement. The results show that contact angle measured at pH 2.3 (68.3 ± 2.7) is greater than the measurement at pH 10.5 (48.2 ± 1.2), which means the membrane surface is more hydrophilic at pH 10.5. Furthermore, the water droplets at pH 10.5 wetted the surface more rapidly and spread out over 300 s. Cheng et al. reported a similar pH responsive wettability on an electrospun PVDF-poly(acrylic acid) nanofiber membrane [182]. The ionization of carboxyl group stretched out the polymer chain and promoted the replacement of air trapped in the pores by water, which accelerated the surface wetting. Such a pH responsive behavior on permeability and wettability could be applied in selectively separation and drug release [183-185].

6.3 Size and distribution of Pd-Fe particles throughout the membrane pores

The size and distribution of reactive particles have significant impacts on dechlorination performance, especially for those particles in the pores of membrane. The particles on the membrane surface were characterized using SEM (Figure 6.5). The average size of Pd-Fe nanoparticles on the membrane surface was calculated as 19.4 ± 3.2 nm (calculated as a Gaussian distribution). However, a special method was required to characterize those particles inside membrane pores, that is the developed FIB cross-sectioning method. The FIB can precisely slice a smooth cross-section plane, which maintains the pore structures. To a better understanding of the FIB-SEM technique, the Millipore PVDF membrane (thickness: 80 μm) was used only for characterization due to its more porous structures and its lack of any supporting materials. As shown in Figure 6.6a, the FIB-modified area, in the center of the cross-section plane, is smoother and

clearer than the unmodified area. As summarized in Figure 6.6d, the particle size was uniform inside membrane pores (23.2 ± 8.2 nm) but smaller than those nanoparticles (39.1 ± 9.3 nm) located on the top and bottom surfaces. The size difference was caused by the formation of a PMAA rich layer (thickness: ~2 μm), which was not restrained by the PVDF pores, on the top and bottom surfaces of the membrane. The particle distribution was observed using EDS mapping. Since the fluorine to carbon ratio is constant in every repeat unit of the PVDF (F/C = 1/1), the iron to fluorine ratio is used to determine the particle distribution inside the membrane pores. A higher distribution of particles on top and bottom surface of the membrane was also observed.

The characterization of functionalized PVDF 700 membranes was also conducted. The EDS mapping, in Figure 6.7d, shows that the Fe was mainly observed at the top PVDF layer (43 μm) and Fe was barely found in the supporting material (127 μm). A greater Fe density and relatively large particles (20.2 ± 6.6 nm) were also observed on both top and bottom surfaces of the PVDF layer. A uniform size and density distribution of particles (17.1 ± 4.9 nm) were found inside the PVDF layer (Figure 6.7e).

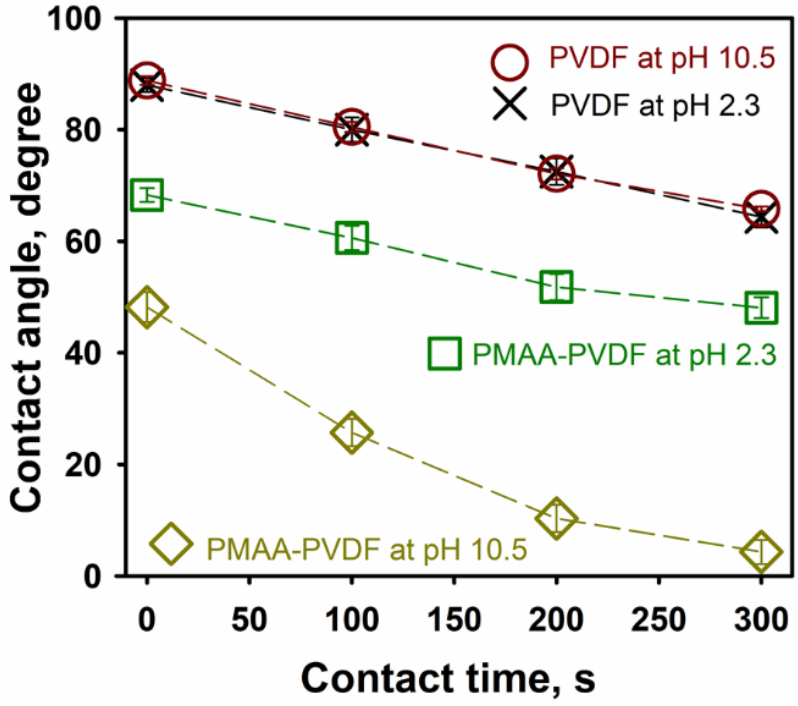

Figure 6.4 The change of contact angles as a function of contact time. The original PVDF membranes (Solecta PVDF 700) were used as a control for the functionalized PMAA-PVDF membranes (12.1 wt% PMAA). The membranes were immersed at target pH and then dried under a nitrogen flow before the contact angle measurement.

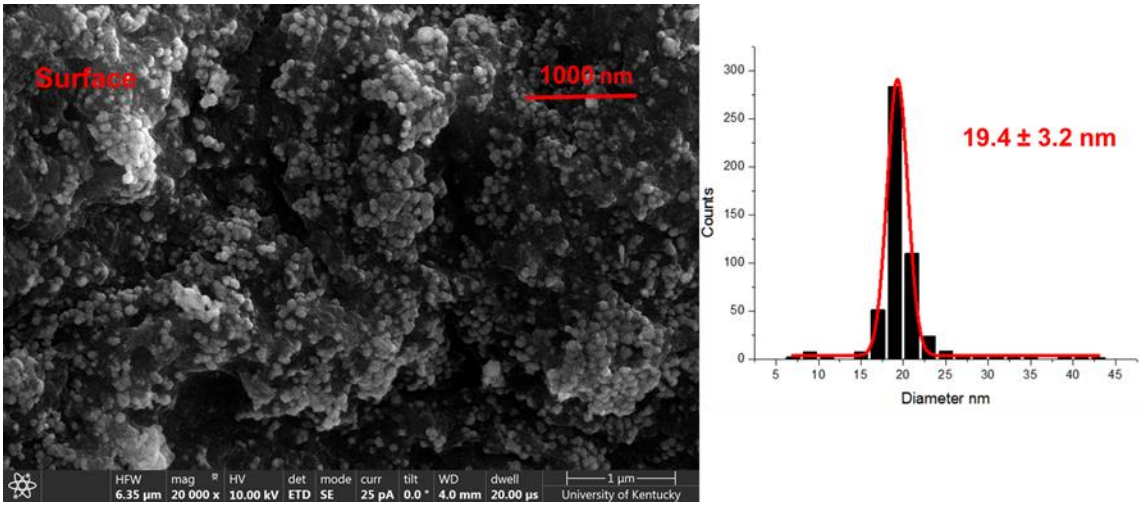

Figure 6.5 FIB-SEM image of the surface on the Fe/Pd-PAA-PVDF 700 membrane (13.4 wt % PAA, 1 mol % initiator and 1 mol % of cross-linker, 4.1 mg Fe, 1.3 wt % Pd) and the summary of observed Fe/Pd nanoparticles (more than 500 counts).

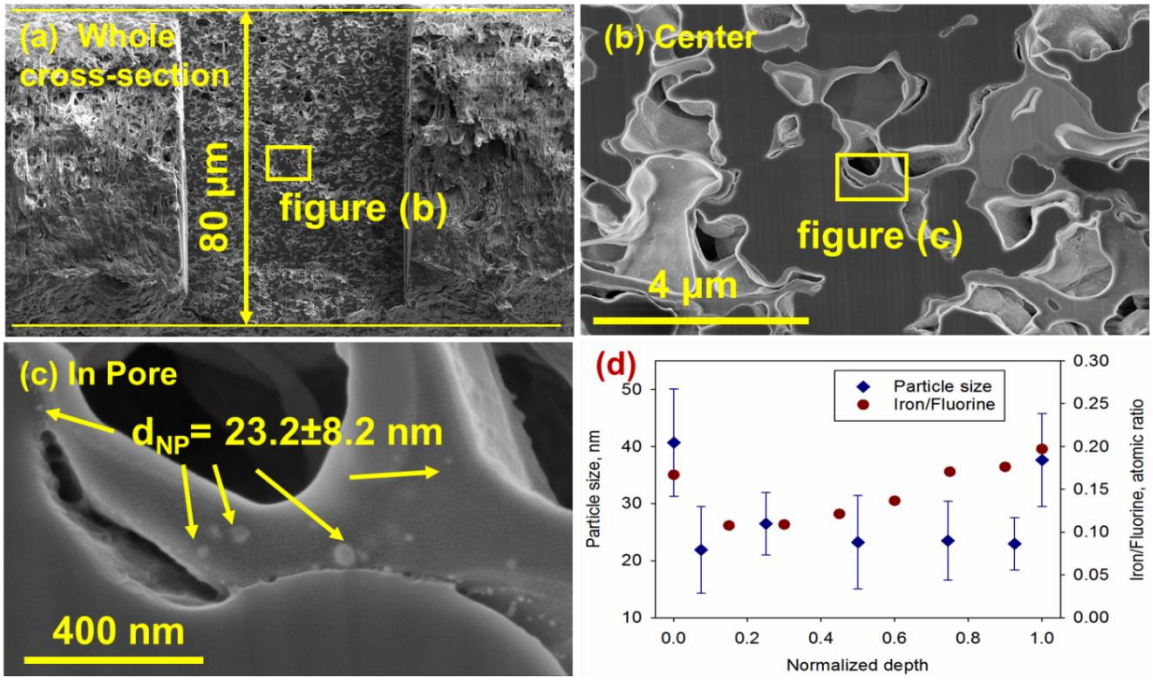

Figure 6.6 The SEM images for nanoparticles in the pores of membranes (PMAA functionalized Millipore DVPP04700 membranes). (a) An 80 µm membrane cross-section sample, the smooth area in the center, was prepared using FIB. (b) pore structure. (c) The nanoparticles inside the pores. (d) The quantification of particle size and distribution at various depths underneath the membrane surface (more than 300 particles were counted in every point). The Millipore PVDF membranes were used only for characterization.

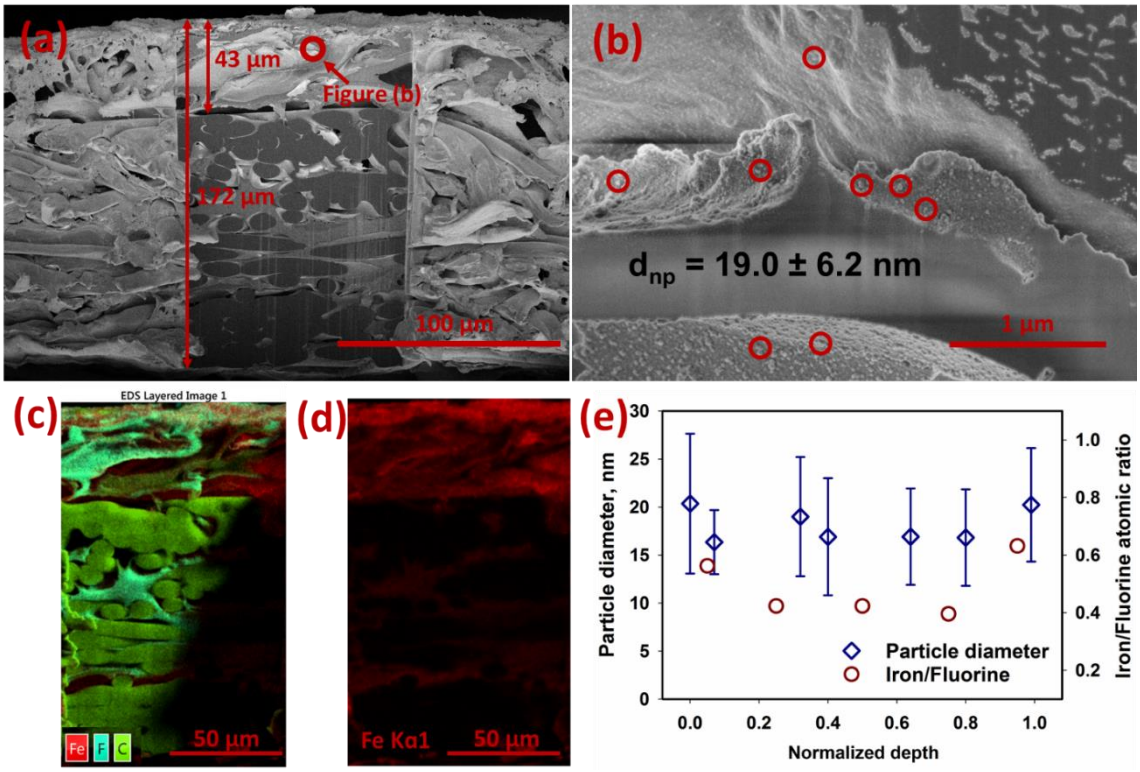

Figure 6.7 The properties of Pd-Fe nanoparticles inside the membrane pores (12.1 wt% PMAA-PVDF 700 membrane). FIB was applied to prepare the entire membrane cross-section samples with less damage (ion beam 2.5-6 nm). (a) An entire membrane cross-section sample. The 172 um thickness sample was first prepared by cracking after freeze drying (liquid nitrogen). The smooth area in the center was treated by FIB. (b) The specific area in FIB modified area in image (a). (c) The elements analysis, in the area under FIB modification, using EDS. (d) The Fe distribution. (e) The relation between particle size and particle distribution at various depths in the PVDF layer. The depths were normalized with the thickness of PVDF top layer, which is 43 µm.

6.4 Reactivity of the Pd-Fe nanoparticles incorporated membranes

After the integration of reactive Pd-Fe nanoparticles and membrane domains, the Pd-Fe incorporated membranes were tested in the degradation of 3,3',4,4',5-pentachlorobiphenyl (PCB-126). The reactive membranes were placed in the bottom of a filtration cell and the solution with PCB-126 was continuously passing through the membranes with the applied pressure (scheme in Figure 6.8). At this convective flow study, the synthetic water was permeated through a Pd-Fe-PAA-PVDF membrane (4.1 mg Fe, Pd was 1.3 wt% of Fe) with the applied pressure ranging from 1.38 to 8.96 bar. The residence time is the period the species spent inside the membrane pores, which is controlled by the operating pressure and is used to determine the reaction time for dechlorination. Assuming a uniform distribution of cylindrical pores of the membranes, the residence time was calculated by $\tau = V_{void} / (J_w A)$, where $V_{void} = V_{matrix} - V_{NP} = \emptyset V_{membrane} - V_{NP}$, and where J_w is the pure water flux at specific pressure. $\emptyset$ is surface porosity. V_{matrix} is the space inside membrane pores (based on the weight difference between dry and wet PAA-PVDF membranes). V_{NP} is the volume of Pd-Fe particles, which was calculated using the specific metal loading and the average size of particles obtained from the characterization.

As shown in Figure 6.9, with the increase of residence time, the PCB-126 concentration in the permeate remained unchanged when the PCB synthetic solution penetrated the Fe-PAA-PVDF membrane. It means the absorption and evaporation of PCB-126 can be neglected under convective flow mode. In contrast, the concentration of the PCB in the permeate side continuously decreased with the increases of residence time. About 96% of the PCB was dechlorinated at a residence time of 14.7 seconds. The reaction rate was determined by the kinetic studies below.

Based on the characterization of membrane and Pd-Fe nanoparticles, the functionalized membrane is assumed to be a combination of cylindrical pores with uniformly distributed Pd-Fe nanoparticles. Furthermore, due to the small Reynolds number ($Re \ll 1$), each cylindrical pore could be assumed to be a laminar flow reactor (LFR) [186, 187].

For laminar flow in every cylindrical pores:

$$u(r) = 2u_0(1 - \frac{r}{R})^2 \qquad (6.1)$$

Where R is the pore size of the functionalized membrane. Velocity u_0 and u(r) are the velocities at center of the pores or at radius r, respectively.

Flux through the membrane with surface area (A_M = 13.2 cm^2) and porosity ($\emptyset$ = 35.4%):

$$J_w = \frac{n_{pores} \int_0^R u(r) 2\pi r dr}{A_M} = \frac{\emptyset u_0}{2} \qquad (6.2)$$

The mean velocity ($\bar{u}$) at the pores:

$$\bar{u} = \frac{J_w A_M}{n_{pores} \pi R^2} = \frac{J_w}{\emptyset} = \frac{u_0}{2} \qquad (6.3)$$

The residence time (τ) for the membrane thickness (L = 70 μm) is

$$\tau = \frac{V_{void}}{J_w A_M} = \frac{2L}{u_0} \qquad (6.4)$$

It should be noted that the mean velocity is related to the membrane water permeation flux and is a function of transmembrane pressure. Diffusivity of PCB-126 in membrane ($D_M = 1.1 \times 10^{-12}\ m^2 s^{-1}$ in the membrane [50]) in this study can be neglected

because of the large Peclet number (ranging from 10^2 to 10^3). Besides, when assuming diffusion is isotropic, the mass balance of the pseudo-first-order reaction can be integrated as a function of pore axial distance, z, since u(r) is only a function of radius. k_{obs} refers to rate constant for parent compound degradation (PCB-126).

$$C(r,z) = C(r,0)\exp\left[-\frac{k_{obs}z}{u(r)}\right] \qquad (6.5)$$

In order to obtain the mean concentration $\bar{C}$ at certain z, a cross-section averaging method was applied to integrate the concentration over the radial dimension as below [186]:

$$\bar{C}_{final} = \frac{\int_0^r C(r,z)u(r)2\pi r dr}{\int_0^r u(r)2\pi r dr} \qquad (6.6)$$

$$\bar{C}_{final} = \frac{2\bar{C}_{initial}\int_{u_0}^{0} e^{\left(-\frac{k_{obs}L}{u(r)}\right)}u(r)du(r)}{{u_0}^2} \qquad (6.7)$$

Therefore, the mean outlet concentration $\bar{C}_{final}$ (z = L) can be evaluated by the exponential integral:

$$\bar{C}_{final} = \frac{\bar{C}_{initial}\left[(k_{obs}L)^2 E_1\left(\frac{k_{obs}L}{u_0}\right) + e^{-\frac{k_{obs}L}{u_0}}(u_0^2 - k_{obs}Lu_0)\right]}{u_0^2} \qquad (6.8)$$

Substituting u_0 with τ:

$$\bar{C}_{final} = \frac{\bar{C}_{initial}\tau^2\left[{k_{obs}}^2 E_1\left(\frac{k_{obs}\tau}{2}\right) + e^{-\frac{k_{obs}\tau}{2}}\left(4\frac{1}{\tau^2} - 2\frac{k_{obs}}{\tau}\right)\right]}{4} \qquad (6.9)$$

$$E_1\left(\frac{k_{obs}\tau}{2}\right) = \int_{\frac{k_{obs}\tau}{2}}^{\infty} \frac{e^{-t}}{t} dt \qquad (6.10)$$

This derived equation 6.9 can be used to fit k_{obs} values from the experimental reaction data ($\tau, \bar{C}_{initial}, \bar{C}_{final}$). For residence time of 7.1 s, 14.7 s and 27.0 s, k_{obs} was determined to be 0.359 s^{-1}, 0.317 s^{-1} and 0.329 s^{-1}, respectively. The model verified that k_{obs} is indeed independent of τ. Furthermore, the LFR model was used to simulate degradation versus residence time. The smallest root mean square of simulated data and experimental results was 0.11 at the k_{obs} value equal to 0.355 s^{-1}(Figure 6.9). The k_{sa} was calculated (fitted as a pseudo first order reaction) as 0.171 $Lm^{-2}h^{-1}$. By comparison, the plug flow reactor (PFR) model was also applied. Since the assumption of PFR model is the fluid in the tube is perfectly mixed, it needs a smaller reaction rate to achieve the same degradation performance compared to that of the LFR model. The decreases in derived k_{obs} was observed that the average k_{obs} was calculated as 0.23 s^{-1} for PFR model, which is only 65% of the observed rate constant obtained from LFR model.

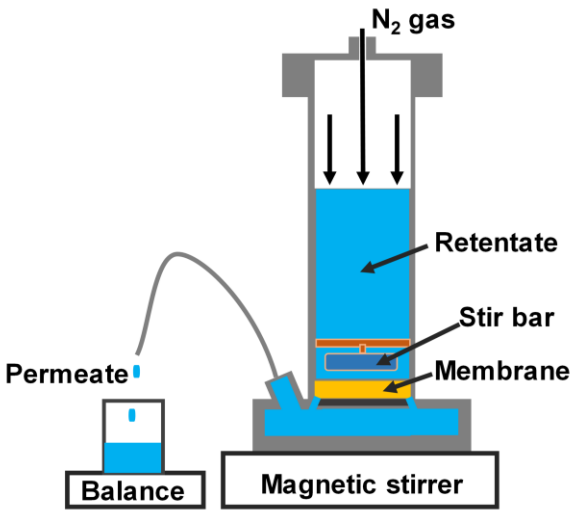

Figure 6.8 Scheme of the convective flow study of PCB-126 degradation. The reactive membrane was placed in the bottom of the filtration cell.

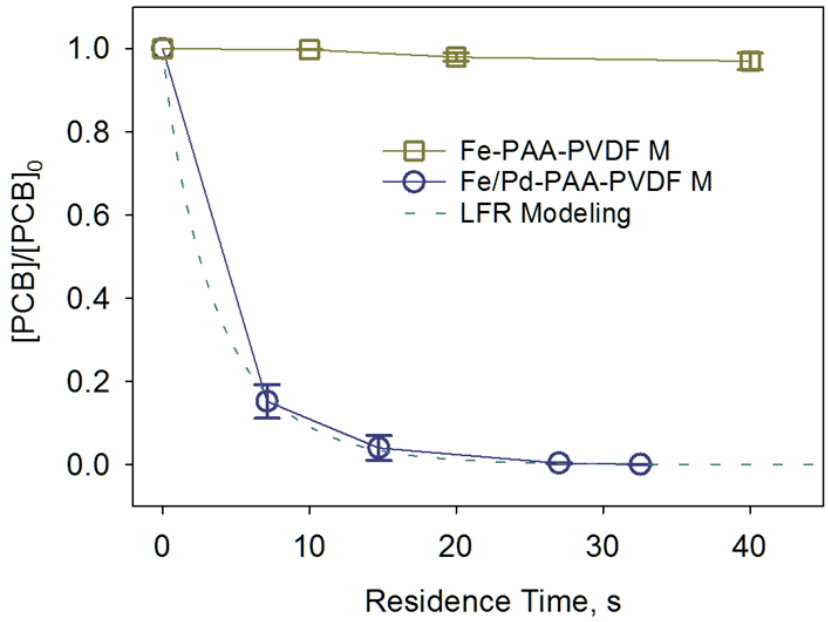

Figure 6.9 Convective flow study of PCB-126 degradation by Fe-Pd-PAA-PVDF 700 membranes. Fe-PAA-PVDF membrane served as blank control group and laminar flow reactor model was used for experimental data fitting. Effective surface area: 13.2 cm^2. $[PCB\text{-}126]_0$ = 15 μM, 4.1 mg Fe per membrane, [Pd] = 1.3 wt % as Fe, pH = 5.5, T = 22 ℃.

CHAPTER 7. GROUNDWATER TREATMENT USING REACTIVE MEMBRANES

7.1 Overview

Combined with the material characterization and degradation study, the research is extended to the remediation of contaminated groundwater using the Pd-Fe nanoparticles incorporated membranes. The groundwater was collected from a contaminated industrial site, that is currently being remediated by Arcadis US Inc. Compared to the conventional sorption methods, such as air stripping, the use of reactive membranes could save the energy to produce steam gas periodically for the regeneration of activated carbon adsorbent and could degrade the contaminants to non-toxic compounds.

7.2 Groundwater condition

The groundwater contains saturated and unsaturated chlorinated aliphatic compounds, that are dichloromethane (DCM), chloroform (CF), carbon tetrachloride (CTC), trichloroethylene (TCE), tetrachloroethylene (PCE), hexachloroethane and hexachloro-1,3-butadiene (HCBD) (Figure 7.1). Within these compounds, we are interested in the treatment of CF, CTC, TCE and PCE. The concentration of these target compounds as well as the water condition are summarized in Table 7.1. No significant variation in concentration of contaminants was observed between the groundwater samples collected during spring and summer in 2018. In this study, the real groundwater samples (collected on summer) were used in the treatment study in both solution phase without membranes and in membrane domain under convective flow mode.

Table 7.1 Analysis results of the collected groundwater samples during spring and summer in 2018. Volatile chlorinated species (unit, ppb) were analyzed using purge and trap GC-MS method. The groundwater was used in the remediation tests in the lab.

Species	Chloroform (CF)	Carbon tetrachloride (CTC)	Trichloroethylene (TCE)	Tetrachloroethylene (PCE)
Spring samples	32 ±1	39 ±1	185 ±1	980 ±2
Summer samples	25 ±1	31 ±1	168 ±2	919 ±2
* EPA MCL drinking water	**MCLG 70	5	5	5

pH	Iron ppm	Calcium ppm	Magnesium ppm	Chloride ppm	Hardness as $CaCO_3$, ppm	Conductivity µS/cm
7.8	<0.5	102.0	31.5	***30.3	386.3	986

* EPA Maximum Contaminant Level (MCL) – The highest level of a contaminant that is allowed in drinking water. Data obtained from National Primary Drinking Water Regulations (EPA 816-F-09-004).

** MCL N/A for chloroform. EPA Maximum Contaminant Level Goal (MCLG) – The level of a contaminant in drinking water below which there is no known or expected risk to health. Data obtained from EPA 816-F-09-004.

*** Chloride results were analyzed using both the chloride electrode (30.3 ppm) and ion chromatography (26.3 ppm).

Compounds	Methylene chloride	Chloroform	Carbon tet	TCE	PCE	Hexachloroethane	Hexachloro-1,3-Butadiene
Retention time (min)	2.3	2.45	2.8	3.4	5.3	8.3	9.2

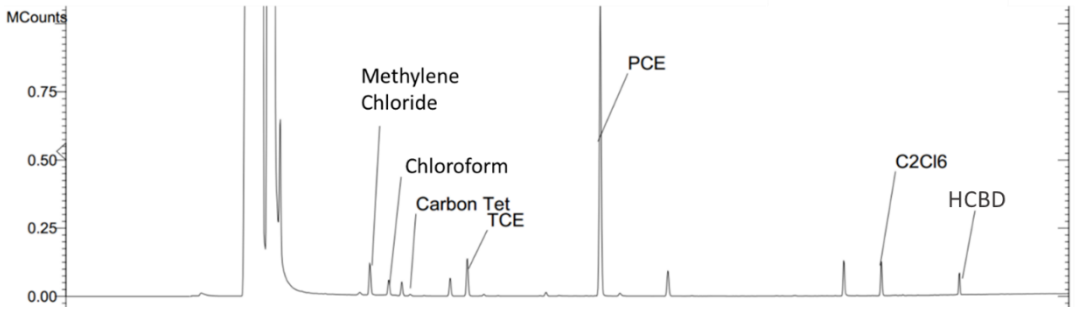

Figure 7.1 Chromatography of different chlorinated organic compounds using purge and trap GC-MS methods

7.3 Groundwater treatment using functionalized reactive membranes

For the convective flow study, the groundwater was permeated through a Pd-Fe-PMAA-PVDF membrane (4.1 mg Fe, Pd was 0.5 wt% of Fe) under 0.34, 0.69 and 1.0 bar, corresponding to the 2.2 s, 1.8 s and 0.9 s residence time, respectively. Residence time is the period the species spent inside the membrane pores, which was controlled by the operating pressure and was used to determine the reaction time for dechlorination. Assuming a uniform distribution of cylindrical pores of the membranes, the residence time (τ) was derived as equation 7.1 and 7.2. The details of calculation are summarized in section 6.4.

$$\tau = V_{void} \,/\, (J_w\, A) \qquad (7.1)$$

$$V_{void} = V_{matrix} - V_{NP} = V_{membrane}\emptyset - V_{NP} \qquad (7.2)$$

The permeate samples at different operating pressures were collected after 15 min to allow the system to reach a steady state. The control group, using the oxidized Pd-Fe-PMAA-PVDF membranes, was made to test the potential loss due to adsorption and evaporation. The membranes were deliberately oxidized by immersing into the water with a purge of air for 12 h. As shown in Figure 7.2a, the concentration of chlorinated species declined continuously with the increase of residence times. The initial pH 7.8 was increased to 8.0, 8.0 and 8.2 at the residence times of 0.9 s, 1.8 s and 2.2 s, respectively. The extent of dechlorination was enhanced with the increased residence time. At 2.2 s residence time in a single pass through the membranes, only 25% CF, 1% CTC, 9% TCE and 16% PCE remained.

As shown in Figure 7.2b, an increase of [Cl^-] in the permeate samples was found using a chloride electrode (calibration curve in Figure 7.3). Based on the GC-MS results,

the theoretical [Cl^-] production should be 1.2 ppm (34 μM) when all the four chlorinated organic compounds were completely dechlorinated. The chloride production was found to be 4 to 5 folds greater than the theoretical amount. Besides the target compounds, other volatile chlorinated organic compounds were also found in the groundwater included ~196 ppb 1,2-dichloroethene, ~82 ppb hexachlorobutadiene and ~200 ppb hexachloroethane. These three volatile compounds were also demonstrated to dechlorinate with Pd-Fe and accounts for some of the difference in chloride mass balance [188, 189]. Since the analysis in this study was focused only on the target volatile chlorinated contaminants, the column used in GC was specific for the detection of those volatile compounds with small molecules. The possible presence of other larger chlorinated organic molecules and non-volatile species was not validated (no chlorobenzene was found using a semi-volatile column). Thus, the measurement of produced [Cl^-] could reflect the overall trend of dechlorination but could not be used as an appropriate indicator for the dechlorination extent of individual chlorinated organics. However, due to the low cost and the benefit for a real-time sensing capability, the chloride electrode can be used as a monitor for the dechlorination performance on-site.

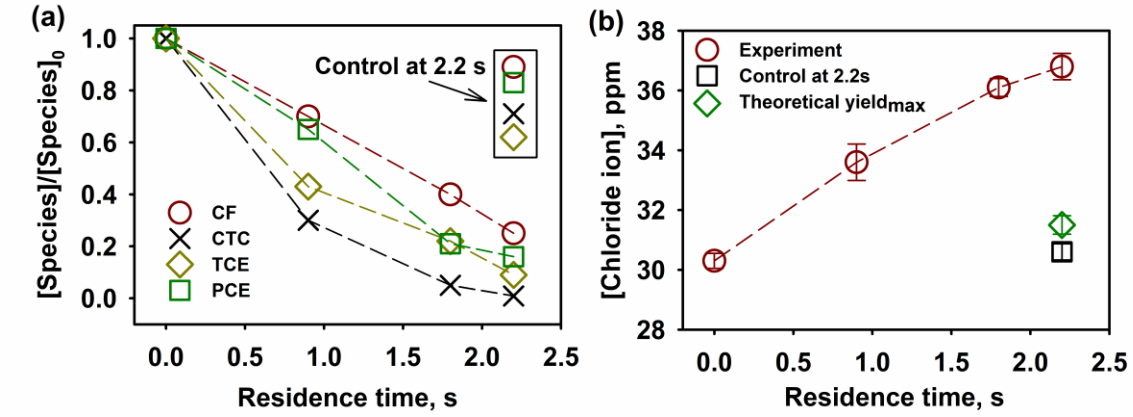

Figure 7.2 Groundwater samples were treated by permeating through the Pd-Fe nanoparticles incorporated membranes (12.1 wt% PMAA, permeability at pH 7.8 was tested as 25 LMH/bar, [Fe]= 4.1 mg per membrane, effective external area 11.2 cm^2, Pd is 0.5 wt% of Fe, initial pH=7.8, T = 23^{o}C). (a) The $[Species]_o$ results came from direct measurement of the groundwater sample. (b) Corresponding chloride concentration was measured by using a chloride electrode. The theoretical $yield_{max}$ indicates the maximum chloride production of four chlorinated compounds. The compounds are: chloroform (CF), carbon tetrachloride (CTC), trichloroethylene (TCE) and tetrachloroethylene (PCE). Deliberately oxidized Pd-Fe nanoparticles incorporated membranes were used as the control groups.

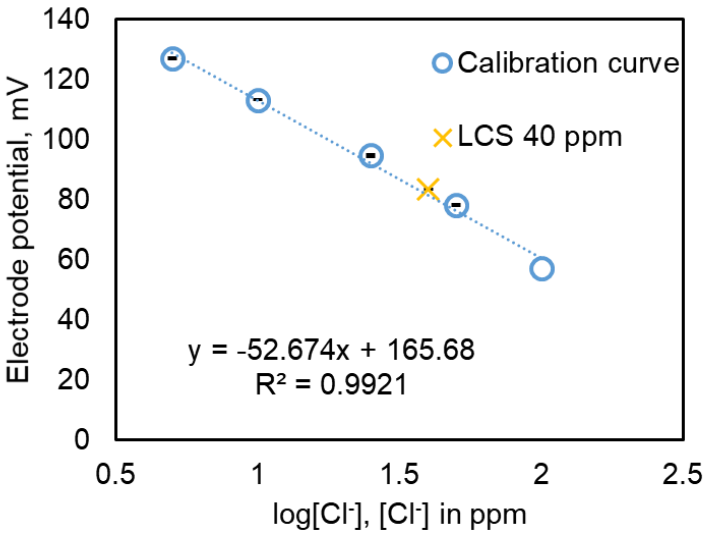

Figure 7.3 Calibration curve of chloride ion using a chloride electrode. LCS: laboratory control sample

7.4 Kinetic studies

An assumption of uniform distribution of cylindrical pores was made based on the characterization of membrane pores (diameter: 121.2 ± 35.4 nm). A plug flow reactor model was then used to obtain the rate constant. For instance, the rate of TCE dechlorination k_{obs}, at residence time of 0.9 s, 1.8 s and 2.2 s, was determined to be 0.93 s^{-1}, 0.80 s^{-1} and 0.89 s^{-1}, respectively. The average k_{obs} was calculated as 0.87 s^{-1}. With the characterization of membrane porosity and nanoparticles inside the membrane pores (particle size of 17.1 ± 4.9 nm, in Figure 6.7e), the k_{sa} value of TCE, for example, in convective flow mode was calculated as 0.009 $Lm^{-2}min^{-1}$ (0.5 wt% Pd).

The groundwater was also treated in solution phase: using Pd-Fe nanoparticles without the membrane domains. After a 30 min reaction in the solution phase studies (CMC is 0.5 wt%, [Fe]=72 ppm and 0.5 wt% Pd), all the species were effectively dechlorinated below the threshold of EPA maximum contaminant level (Figure 7.4). Less than 1% remaining was achieved for all the species except CF. The CF is the dechlorination intermediates of CTC, which leads to the increase of CF concentration in first 5 min of reaction. The control group was made using deliberately oxidized Pd-Fe nanoparticles, which were prepared by purging air into the suspension of the Pd-Fe nanoparticles for 12 h. This control group shows more than 88% remaining of every species.

For chlorinated ethylenes, the complete dechlorination of TCE and PCE to nontoxic ethylene and ethane, using Pd-Fe particles, has been reported in the literature [51, 69, 190, 191]:

$$TCE \xrightarrow{multiple\ dechlorination} ethylene/ethane + 3Cl^{-} \qquad (7.3)$$

For chlorinated methanes, Feng and Lim reported that above 85% CTC was dechlorinated to methane, with an existence of 11% dichloromethane as a dechlorination intermediate [192]:

$$CCl_4 \xrightarrow{Pd-Fe} CH_4 + 4Cl^- \qquad (7.4)$$

$$CCl_4 \xrightarrow{Pd-Fe} CH_2Cl_2 + 2Cl^- \qquad (7.5)$$

To better understand the dechlorination performance, some synthetic solutions with higher initial concentration of CTC (15 ppm) and TCE (11.7 ppm) were made, for use in the chloride ion (Cl^-) measurement. The Cl^- is one of the final products of the dechlorination: the complete dechlorination of 1 mol CTC and 1 mol TCE would theoretically produce 4 mol and 3 mol Cl^-, respectively. The result shows above 99% CTC was degraded and 76% CTC was dechlorinated in 4 h (Figure 7.5). Compared to the complete dechlorination of TCE (nearly 97% conversion of chloride), the less dechlorination in CTC study indicates the incomplete dechlorination of CTC. The GC-MS results show that 8% CTC was converted to dichloromethane, whose concentration was then kept stable in this study.

Based on the degradation results, the degradation could be regarded as pseudo-first-order reaction (equation 7.6). The concentration of CF initially increased due to CTC dechlorination (CF is a dechlorination intermediate of CTC). Since the degradation rate of CTC is much greater than that of CF, for ease of derivation, the degradation of CF could be regarded as pseudo-first-order reaction after the complete degradation of CTC.

$$\frac{dC}{dt} = -k_{sa}\rho_m a_s C \qquad (7.6)$$

Where, k_{sa} is surface normalized reaction rate ($Lm^{-2}min^{-1}$). ρ_m is nanoparticle loading density, which is 0.072 gL^{-1}, a_s is surface area per unit mass, which is 187 m^2g^{-1}, calculated from average spherical nanoparticle size (4.2 nm, based on the TEM characterization) and iron density (7870 gL^{-1}). The summary of k_{sa} is listed in Table 7.2. The reduction rate followed the order of CTC>TCE>PCE>CF.

Compared to the solution phase studies, the same trend of degradation rate was observed as: CTC>TCE>PCE>CF (Table 7.2). Moreover, the significant decline of k_{sa} from the solution phase studies to the membrane domain studies (besides CF) indicates the degradation rate is controlled by diffusion of target compounds in the membrane domain. Compared to the solution phase, the membrane domain causes additional mass transfer resistance, which hinders the diffusion of contaminants to reactive nanoparticles and decreases the observed reaction rate. For CF, the k_{sa} is much lower than the other compounds and the difference between the two studies could within the margin of experimental error.

Table 7.2 The surface area normalized reaction rates (k_{sa}, $Lm^{-2}min^{-1}$) of each compound in both solution phase and membrane domain studies of groundwater remediation (0.5 wt% Pd in both cases).

Conditions	CF	CTC	TCE	PCE
*Solution phase	0.002	0.101	0.034	0.017
**Membrane domain	0.006	0.019	0.009	0.008

* Evaluated using a pseudo-first-order reaction, $R^2 > 0.96$ for all
**Evaluated using a plug flow reactor model, $R^2 > 0.94$ for all

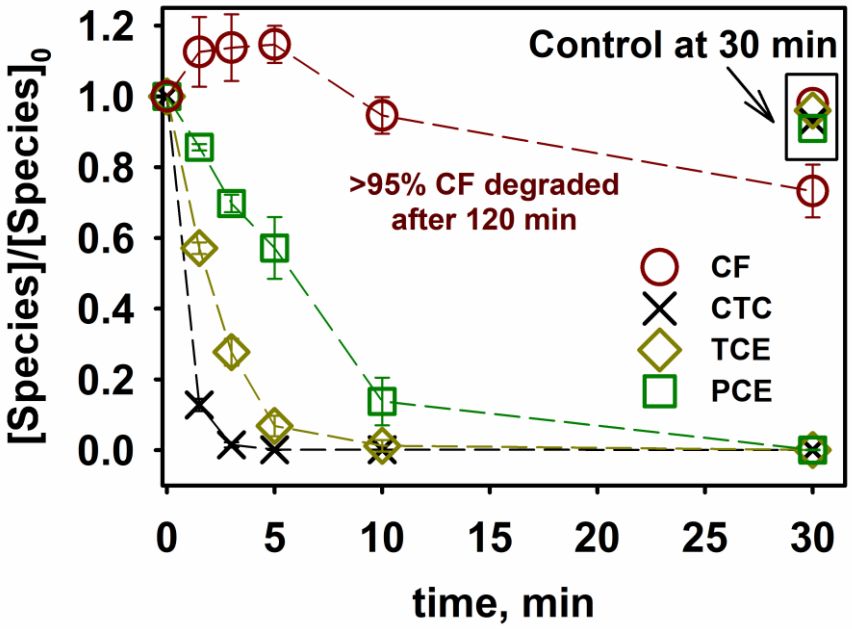

Figure 7.4 Groundwater samples were treated with Pd-Fe nanoparticles in a solution phase study ([Fe]= 72 mg/L, Pd is 0.5 wt% of Fe, 0.5 wt% CMC solution, T= 23ºC, initial pH= 7.8). After post filtration and acid dissolution, the samples were analyzed in purge and trap GC-MS method. The compounds are: chloroform (CF), carbon tetrachloride (CTC), trichloroethylene (TCE) and tetrachloroethylene (PCE). The initial concentration ($[Species]_o$) were directly measured of the groundwater samples with the same filtration and acid dissolution steps. Deliberately oxidized Pd-Fe particles were used as the control groups.

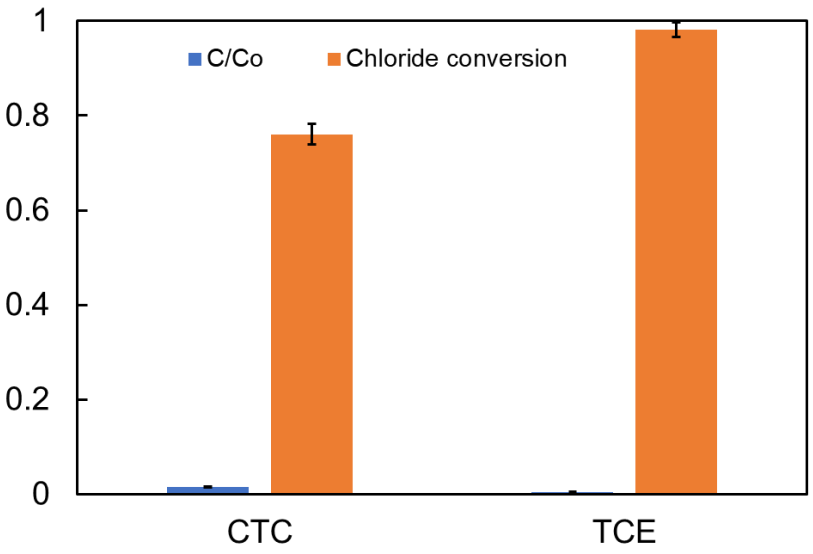

Figure 7.5 The degradation and chloride conversion of CTC and TCE in 4 h solution phase study ([Fe]=72 ppm and 0.5 wt% Pd)

7.5 Long-term degradation of groundwater using reactive membranes

The functionalization of PMAA prevents leaching of embedded nanoparticles. Although the dechlorination reaction and the corrosion in water convert Fe^0 to Fe^{2+}, the PMAA chains serve as cation exchangers and recapture the produced Fe^{2+}. To test the stability of Pd-Fe nanoparticles on the membrane domains, the 200 ml contaminated groundwater samples were pressurized through the membranes at 1 bar (equivalent of 179 L/m^2 flow through membrane). Results show less than 2 % Fe and Pd, compared to the metal loading on the membranes, were leached and found in the permeate solution (measured using ICP).

To test the commercial viability of the functionalized membranes, a long-term study was conducted using the synthetic water of model compounds, such as CTC and PCE (35 ppb CTC and 950 ppb PCE as the similar concentrations as the target groundwater, pH was also adjusted to 7.8). The Pd-Fe-PMAA-PVDF membranes (12.1 wt% PMAA, permeability: 25 LMH/bar) was tested in a continuous flow with the operating pressure of 0.34 bar, which indicates a residence time of 2.2 s. The deliberately oxidized Pd-Fe-PMAA-PVDF membranes were used as control group. As shown in Figure 7.6a, a consistent degradation performance was observed within first 5 h, that is less than 5% CTC and 20% PCE were remained in the permeate samples. A significant decrease of reactivity was observed after 36 h continuous flow (equivalent of treatment of 299 L/m^2). Compared to the reactive nanoparticles for initial condition (Figure 7.6b) several sheet-like structures (15-105 nm in length) were observed after 36 h continuous flow (Figure 7.6c) which indicates the formation of iron oxide or iron hydroxide. This formation of passive layer could hinder the degradation reactions [164, 193]. However, the regeneration of

nanoparticles was achieved by passing $NaBH_4$ (210 mol% of initial [Fe]) through the membranes. After regeneration and washing using deoxygenated DI water, a recovery of reactivity was observed and a similar degradation performance was achieved compared to the first cycle. The control group was also regenerated but then deliberately oxidized again by passing DI water using air for the operating pressure. Particle size on the membrane surface was changed from 20.1 ± 7.2 nm (at t = 0 h) to 26.2 ± 5.2 nm after regeneration (Figure 7.6d) No severe agglomeration of nanoparticles was observed. Furthermore, the capacity of PMAA to recapture the dissolved iron ions (less than 2 % Fe and Pd were leaked) could retain the produced iron ions for further conversion back to Fe^0.

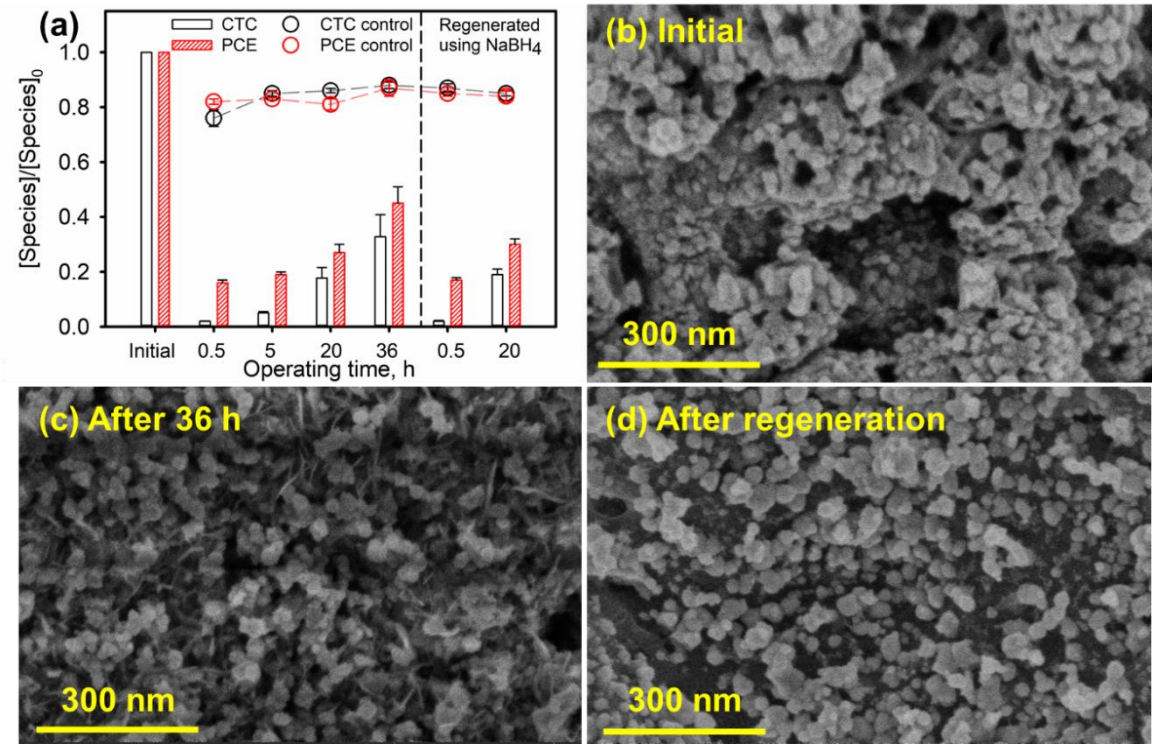

Figure 7.6 The long-term degradation study of the functionalized Pd/Fe-PMAA-PVDF membranes was conducted in convection flow (12.1 wt% PMAA, membrane permeability at pH 7.8: 25 LMH/bar, [Fe]= 4.1 mg per membrane, effective external area 11.2 cm^2, Pd is 0.5 wt% of Fe, initial pH= 7.8, T = 23^{o}C). Synthetic water was prepared with the similar concentrations of those in the groundwater (35 ppb carbon tetrachloride (CTC) and 950 ppb tetrachloroethylene (PCE)). The deliberately oxidized functionalized membranes were used as the control groups and these membranes were oxidized again after $NaBH_4$ regeneration process. Figure (a): degradation performance in a continuous flow at 0.34 bar (residence time 2.2 s). Figure (b, c, d): the reactive particles on the membrane surface were characterized in three different conditions.

7.6 On-site treatment of chlorinated organics using reactive membranes

The groundwater was firstly filtered using a Keystone 5-micron filter cartridge to remove sediments. The water conditions after pre-filtration are summarized in Table 7.3. Typical samples (after pre-filtration and after treatment) were also tested by an environmental testing lab (Eurofins TestAmerica, Inc). About 10% error was detected from species measured between UK and Eurofins, but about 30% error was found in the feed concentration of CF, and the concentration of TCE and PCE after the test. To get a better comparison, multiple samples need to be evaluated (instead of the only two samples were evaluated in this case). Also, for these highly volatile toxic chlorinated organics, no air bubble should be left in the sealed vials. Compared to the groundwater samples collected at the spring and summer in 2018 (Table 7.1), the concentration of CTC in the groundwater (collected in Oct 2019) increased around 42% and the concentration of PCE and chloride ion decreased around 49% and 30%, respectively. After the pre-filtration, the groundwater was pumped through the cross-flow setup and then recycled back to the feed container. The permeates through reactive membranes were collected and analyzed. The operation conditions of reactive Pd-Fe functionalized membranes in the cross-flow setup are listed in Table 7.4.

Effective treatment was achieved in the on-site technology evaluation as expected. As shown in Figure 7.7a, only 32% CF, <0.1% CTC, 12% TCE and 14% PCE was detected after passing through reactive membranes at 2.4 s residence time (7.1 mg Fe per membrane, 0.5 wt% Pd). Compared to the remediation tests conducted in lab (section 7.5), a similar degradation performance was observed for the on-site tests under a similar residence time (Table 7.4). Degradation performance was consistence within the first 2 h except a decrease

of CF degradation was detected. This decreases in CF degradation was restored after the reductive regeneration of the membrane (50 mol% $NaBH_4$). The increased concentration of chloride ion ($[Cl^-]_{initial}$ = 22 ppm) after the treatment also demonstrated the successful dechlorination reaction (Figure 7.7b). However, as we reported [55], the reactive membranes also degrade the other chlorinated organic compounds in the groundwater, such as hexachloroethane (~90 ppb) and hexachlorobutadiene (~43 ppb). Therefore, the detection of chloride ion can only show the trend of dechlorination reaction but not the degradation performance of specific compounds.

The long-term degradation tests were also conducted. A decrease of degradation was observed during the aging process (Figure 7.8): no obvious degradation was detected after 26 h of aging (equivalent of treatment of 193 L/m^2). This deactivation attributes to the water corrosion/oxidation of incorporated Fe nanoparticles as mentioned in section 4.4 and 7.5. As shown in Figure 7.9, the initial membrane with metallic Fe^0 particles (black) turned brown after 27 h of aging, which indicates the oxidation of Fe^0. After the 27 h of aging, the regeneration using 50 mol% $NaBH_4$ converted the oxidized iron back to Fe^0 (Figure 7.9c) and restored the reactivity and present a similar degradation compared to that of the freshly prepared membranes (Figure 7.8).

The results of on-site treatment match with the results obtained in the bench. For further optimization of the system, a magnetic drive pump could be used as an alternative to decrease the heat generation and enable the continuous operation. Since the flow/permeate ratio was only 0.016% in this test, a bypass line could be added to control the flowrate and save energy. Membrane spiral wound module, with 220-fold greater surface area (0.45 m^2), could be applied to increase the treatment capability to 0.15 GPM.

Furthermore, a parallel arrangement of membrane modules could be installed to increase the capacity and add flexibility of application.

Table 7.3 Analysis results of groundwater samples collected after pre-filtration (5-micron filter cartridge) and collected after a 0.5 h continuous flow through the reactive membranes. The concentration of target species was tested both in the lab at University of Kentucky (UK) and by an environmental testing lab (Eurofins TestAmerica, Inc). The groundwater was collected at October 2019 and was used in the on-site remediation tests.

Sample	Location	Measured (ppb)				Dilution corrected (ppb))			
		CF	CTC	TCE	PCE	CF	CTC	TCE	PCE
Feed	UK	6.6	13.4	36.1	141.8	31.7	58.9	158.9	637.1
	Eurofins	9.9	10.7	36.7	141.0	47.4	51.4	176.2	676.8
Test	UK	2.0	<0.1	3.6	16.3	9.6	<0.1	15.9	71.7
	Eurofins	1.8	<0.1	2.3	11.1	8.6	<0.1	11.1	53.3

Table 7.4 Groundwater remediation (in lab and on-site) using reactive Pd-Fe functionalized membranes. On-site tests were conducted on a cross flow unit with higher contact area than the filtration cell used in lab. Degradation results were compared based on the similar residence time (reaction period) in these two cases.

A. Membrane operation conditions:

Type	PMAA (wt%)	Membrane Area (cm^2)	Pressure (bar)	Residence time (s)	Permeability $L/(m^2*h*bar)$
In lab	12.1	11.2	0.34	2.2	25
On-site	16.4	20.0	2.41	2.4	6.2

B. Groundwater remediation performance (percentage represents the residue of species after passing through the reactive membranes at corresponding residence time):

Type	Residence time (s)	CF	CTC	TCE	PCE
In lab	2.2	25%	<0.1%	9%	16%
On-site	2.4	32%	<0.1%	12%	14%

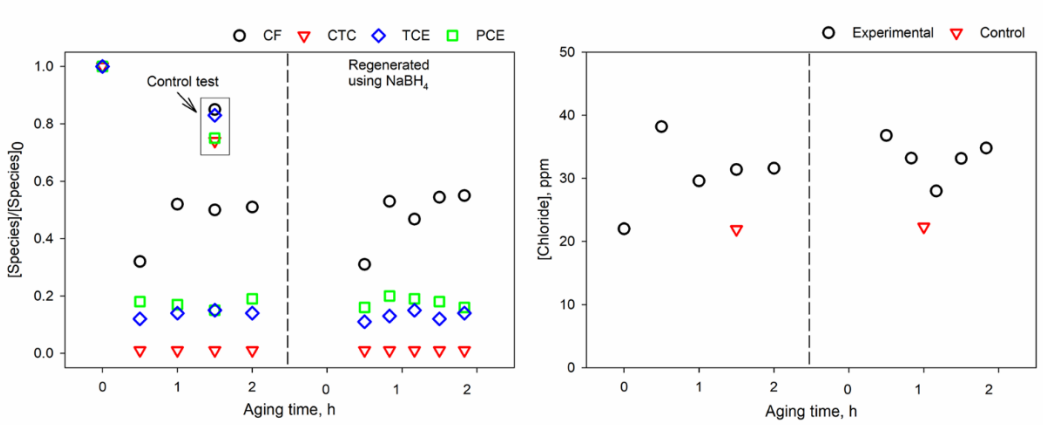

Figure 7.7 On-site cross-flow studies using the 16.4 wt% PMAA-functionalized membrane filter (0.5 wt% Pd). Operating pressure: 2.4 bar. (a) degradation performance (b) chloride ion production. The membrane without reactive nanoparticles was also tested as a control group.

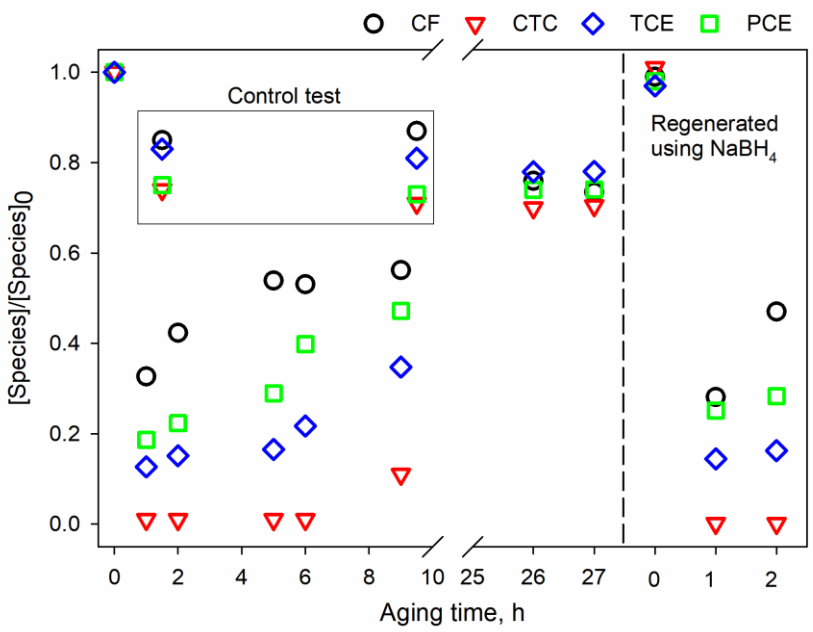

Figure 7.8 Long-term degradation and regeneration studies (on-site tests) using the 16.4 wt% PMAA-functionalized membrane filter (0.5 wt% Pd). Operating pressure: 2.4 bar. The membrane without reactive nanoparticles was also tested as a control group.

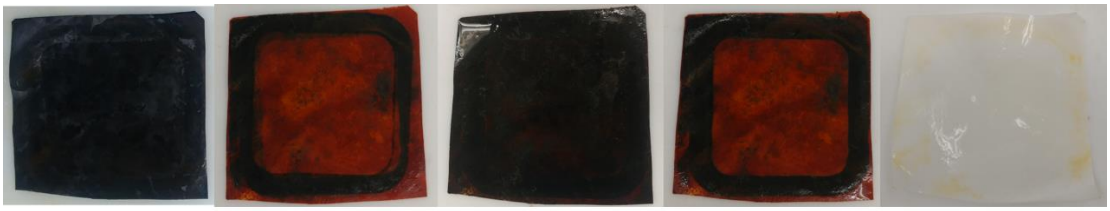

Figure 7.9 Changes of the reactive membrane during the aging and regeneration processes.

CHAPTER 8. CONCLUSION

8.1 Overview

In this dissertation, three different Fe based nanoparticles (bare Fe, Pd-Fe and S-Fe) were evaluated in terms of morphology, reactivity, longevity and regeneration. Pd-Fe nanoparticles, with 20-fold greater reaction rate of CTC than that of bare Fe (k_{sa} = 0.580 $Lm^{-2}min^{-1}$), were selected as the reactive nanoparticles for the treatment of chlorinated organic compounds in groundwater (reductive pathway). To prevent the leaching and agglomeration of nanoparticles, PAA or PMAA functionalized membrane platforms were developed to in-situ generate Pd-Fe nanoparticles in the pores of membranes (ion-exchange process). These reactive membranes effectively treated model compound PCBs and a mixture of chlorinated organic compounds in the groundwater. The long-term treatment, regeneration and reuse of aged reactive membranes were achieved both in lab and on-site.

8.2 Specific accomplishments of each chapter

<u>Chapter 4. Fe based nanoparticles: formation, reactivity and longevity</u>

- After the sythesis of the precursor Fe^0 nanoparticles (~ 35 nm radius), Pd-Fe and S-Fe nanoparticles were prepared based on the distinct formation mechanisms: Pd-Fe (redox reaction) and S-Fe (corrosion and precipitation).
- An increases of Pd dose (1 to 10 mol%) dramatically deformed the original structure of near-spherical Fe^0 core with dispersive Pd islets to dendritic structures, which significantly consumed Fe^0 on the surface of nanoparticles and decreased degradation rate of CTC.

- For S-Fe and Fe nanoparticles, H_2 evolution is an undesired side reaction of degradation via electron transfer mechanism. S-Fe has been reported to limit H_2 evolution and thereby enhance CTC degradation and particle longevity compared to bare Fe: only < 5% CF (major intermediate of CTC degradation) remained after 24 h degradation using S-Fe while nearly 60% CF remained when using Fe.
- S-Fe presented better longevity compared to Pd-Fe and Fe. Significant agglomeration was observed in all types of particles after 31-days of aging. Individual near-spherical Fe cores were oxidized to thin rods and polygonal structures, which were identified as FeOOH and magnetite (Fe_3O_4)/maghemite (γ-Fe_2O_3) respectively via interplanar spacing measurement and XRD analysis.
- Similar morphology and degradation performance were restored for both regenerated Fe and Pd-Fe, comparable to that of freshly made particles (using reducing agent $NaBH_4$).
- Only the Fe core was restored for S-Fe (using $NaBH_4$) but not the disappeared FeS_x shell. The loss of FeS_x during aging made S-Fe nanoparticles eventually have similar morphology and CTC degradation performance compared to that of bare Fe after the regeneration (using $NaBH_4$) process.

Chapter 5. Evaluation of particle properties and water conditions in dechlorination treatment

- The increased Pd coverage on the Fe surface limited the H_2 production. With Pd coverage of 0.1%, 3.8% and 94.3%, the H_2 production at same time interval decreased 38%, 98% and 99.9%, respectivily, compared to that of bare Fe (without Pd).

- The insufficient H_2 production with a increase of Pd coverage significantly hindered hydrodechlorination: only 18% PCB-1 was degraded under 94.3% Pd coverage, comparing to 80% degradation was detected at Pd coverage of 1%. The H_2 production was observed to become the rate limiting factor for dechlorination performance at higher Pd coverage on the Fe surface (10.4 to 94.3%, corresponding to 5.5 to 50 wt% Pd of Fe).
- Palladized-Fe presented faster dechlorination rate: k_{obs} is 18-fold higher than isolated Pd and Fe nanoparticles (Pd is 0.5 wt% of Fe in both cases).
- The activation energy of PCB-1 dechlorination was calculated as 26.5 kJ/mol at pH 7.8 (0.5 wt% Pd). Even though lower solution pH (pH 3.6) increased the initial dechlorination rate, it eventually produced less biphenyl than the batches at pH 7.8 and 9.2.
- The surface area normalized reaction rate (k_{sa}) of CF, CTC, TCE and PCE are 0.005, 0.580, 0.073 and 0.152 $Lm^{-2}min^{-1}$, respectivly. These rates were measured individually using Pd-Fe nanoparticles (0.5 wt% Pd).

Chapter 6. Integration of reactive Pd-Fe nanoparticles and functionalized membranes

- Due to the ionization of the carboxyl group, both PAA and PMAA were deprotonated ($-COO^-$) when solution pH is higher than the pKa of PAA or PMAA. The pH responsive behavior in membrane pores was also observed: the membrane permeability was decreased by 5-30 folds when pH increased from 2.3 to 10.5.
- The PAA or PMAA functionalized membranes control the size of synthesized Pd-Fe nanoparticles. A uniform distribution of particle size (17.1 ±4.9 nm) and density

was observed throughout the entire PVDF membranes using the developed FIB cross-sectioning method.

- In convective flow treatment of PCB-126, about 96% of the PCB was dechlorinated at a residence time of 14.7 seconds. An LFR model was used to investigate the reaction rate. The surface area normalized rate constant k_{sa} was calculated to be 0.171 $Lm^{-2}h^{-1}$.

Chapter 7. Groundwater treatment using reactive membranes

- For the tests in the lab, a single pass through the PMAA functionalized membrane (0.5 wt% Pd, 99.5% Fe) lowered feed concentrations by 75% CF, 99% CTC, 91% TCE and 84% PCE at a residence time of only 2.2 seconds. The degradation rate followed the order of CTC>TCE>PCE>CF.
- The similar oxidation of Fe (FeOOH and magnetite (Fe_3O_4)/maghemite (γ-Fe_2O_3)) was observed when the reactive Pd-Fe nanoparticles incorporated membranes were applied in the long-term treatment of the groundwater sample
- The formation of PMAA in membrane pores prevents agglomeration: particle size was 20.1 $\pm$ 7.2 nm at initial and 26.2 $\pm$ 5.2 nm after a 36 h continuous flow and following $NaBH_4$ reduction. Less than 2% leaching of the incorporated nanoparticles were observed after passing 179 L/m^2 equivalent of water through the membranes at 1 bar.
- With a complete degradation of CTC and TCE, 76% and 97% conversion of chloride ions were detected, respectivly. The incomplete dechlorination of CTC showed the conversion of 8% dichloromethane, whose concentration was then kept stable with the reactive Pd-Fe nanoparticles.

- For the on-site technology evaluation, effective treatment was achieved as expected: less than 0.1% CTC, 18% PCE and 12% TCE were observed at a residence time of 2.4 seconds in passing through the reactive membranes. After the deactivation of nanoparticles under a 27 h of aging, the regeneration using 50 mol% $NaBH_4$ succesfully restored the reactivity and the regenerated membranes presented a similar degradation compared to that of the freshly prepared reactive membranes.

8.3 Key advancements to science and engineering

- In-situ polymerization of acrylic acid or methacrylic acid allows the in-situ synthesis of nanoparticles inside the pores of membranes, providing a suitable platform to prevent the agglomeration and leaching of reactive nanoparticles. This method can be used in various domains to in-situ generate metallic nanoparticles.
- With the development of the FIB cross-sectioning method, individual nanoparticles can be clearly characterized inside the pores of membranes (at different depths), resulting in a better simulation of degradation performance and providing an advanced material characterization method to investigate the nano-structures of polymer/nanoparticles matrix.
- The advanced characterizations (FIB, TEM, XPS, etc.) on particle morphologies and compositions during the aging and regeneration processes providing an insight understanding of particle reactivity, longevity and regeneration.
- The evaluation of particle properties (Pd coverage, composition, etc.) and water parameters in degradation performance guides the design of optimal reactive nanoparticles incorporated membrane systems for the application in groundwater

treatment. The H_2 evolution was also quantified, with various compositions of Pd-Fe nanoparticles, to determine the degradation performance.

- The effective treatment of the groundwater (a mixtures of organic contaminants) both in lab and on-site enriches the understanding of membrane applications and enhances the optimization of the reactive membrane systems for the potential to scale up.

REFERENCES

[1] D. Henschler, Toxicity of chlorinated organic compounds: effects of the introduction of chlorine in organic molecules, Angewandte Chemie International Edition in English, 33 (1994) 1920-1935.

[2] M. Rossberg, W. Lendle, G. Pfleiderer, A. Tögel, E.L. Dreher, E. Langer, H. Rassaerts, P. Kleinschmidt, H. Strack, R. Cook, Chlorinated hydrocarbons, Ullmann's encyclopedia of industrial chemistry, (2006).

[3] A.P.H. Association, Resolution 9304: Recognizing and addressing the environmental and occupational health problems posed by chlorinated organic chemicals, Am J Public Health, 84 (1994) 514-515.

[4] S. Ramamoorthy, S. Ramamoorthy, Chlorinated organic compounds in the environment: regulatory and monitoring assessment, CRC press, 1997.

[5] H. Nollet, M. Roels, P. Lutgen, P. Van der Meeren, W. Verstraete, Removal of PCBs from wastewater using fly ash, Chemosphere, 53 (2003) 655-665.

[6] C. Tu, Y. Teng, Y. Luo, X. Li, X. Sun, Z. Li, W. Liu, P. Christie, Potential for biodegradation of polychlorinated biphenyls (PCBs) by Sinorhizobium meliloti, Journal of hazardous materials, 186 (2011) 1438-1444.

[7] M. Stefaniuk, P. Oleszczuk, Y.S. Ok, Review on nano zerovalent iron (nZVI): from synthesis to environmental applications, Chemical Engineering Journal, 287 (2016) 618-632.

[8] R. Mukherjee, R. Kumar, A. Sinha, Y. Lama, A.K. Saha, A review on synthesis, characterization, and applications of nano zero valent iron (nZVI) for environmental remediation, Critical Reviews in Environmental Science and Technology, 46 (2016) 443-466.

[9] B.V. Aken, P.A. Correa, J.L. Schnoor, Phytoremediation of polychlorinated biphenyls: new trends and promises, Environmental science & technology, 44 (2010) 2767-2776.

[10] R.W. Gillham, S.F. O'Hannesin, Enhanced degradation of halogenated aliphatics by zero-valent iron, Groundwater, 32 (1994) 958-967.

[11] F.-W. Chuang, R.A. Larson, M.S. Wessman, Zero-valent iron-promoted dechlorination of polychlorinated biphenyls, Environmental science & technology, 29 (1995) 2460-2463.

[12] N.C. Mueller, J. Braun, J. Bruns, M. Černík, P. Rissing, D. Rickerby, B. Nowack, Application of nanoscale zero valent iron (NZVI) for groundwater remediation in Europe, Environmental Science and Pollution Research, 19 (2012) 550-558.

[13] H. Kim, H.-J. Hong, J. Jung, S.-H. Kim, J.-W. Yang, Degradation of trichloroethylene (TCE) by nanoscale zero-valent iron (nZVI) immobilized in alginate bead, Journal of hazardous materials, 176 (2010) 1038-1043.

[14] W.S. Orth, R.W. Gillham, Dechlorination of trichloroethene in aqueous solution using Fe0, Environmental Science & Technology, 30 (1995) 66-71.

[15] X.-q. Li, D.W. Elliott, W.-x. Zhang, Zero-valent iron nanoparticles for abatement of environmental pollutants: materials and engineering aspects, Critical reviews in solid state and materials sciences, 31 (2006) 111-122.

[16] Y. Liu, S.A. Majetich, R.D. Tilton, D.S. Sholl, G.V. Lowry, TCE dechlorination rates, pathways, and efficiency of nanoscale iron particles with different properties, Environmental science & technology, 39 (2005) 1338-1345.

[17] J. Yu, X. Hou, X. Hu, H. Yuan, J. Wang, C. Chen, Efficient Degradation of Chloramphenicol by Zero-Valent Iron Microspheres and New Insights in Mechanisms, Applied Catalysis B: Environmental, (2019) 117876.
[18] F. He, D. Zhao, Hydrodechlorination of trichloroethene using stabilized Fe-Pd nanoparticles: Reaction mechanism and effects of stabilizers, catalysts and reaction conditions, Applied Catalysis B: Environmental, 84 (2008) 533-540.
[19] E.J. Borojovich, R. Bar-Ziv, O. Oster-Golberg, H. Sebbag, M. Zinigrad, D. Meyerstein, T. Zidki, Halo-organic pollutants: The effect of an electrical bias on their decomposition mechanism on porous iron electrodes, Applied Catalysis B: Environmental, 210 (2017) 255-262.
[20] T. Phenrat, T. Thongboot, G.V. Lowry, Electromagnetic induction of zerovalent iron (ZVI) powder and nanoscale zerovalent iron (NZVI) particles enhances dechlorination of trichloroethylene in contaminated groundwater and soil: proof of concept, Environmental science & technology, 50 (2015) 872-880.
[21] F. Fu, D.D. Dionysiou, H. Liu, The use of zero-valent iron for groundwater remediation and wastewater treatment: a review, Journal of hazardous materials, 267 (2014) 194-205.
[22] J.A. Donadelli, L. Carlos, A. Arques, F.S.G. Einschlag, Kinetic and mechanistic analysis of azo dyes decolorization by ZVI-assisted Fenton systems: pH-dependent shift in the contributions of reductive and oxidative transformation pathways, Applied Catalysis B: Environmental, 231 (2018) 51-61.
[23] I. Grčić, S. Papić, K. Žižek, N. Koprivanac, Zero-valent iron (ZVI) Fenton oxidation of reactive dye wastewater under UV-C and solar irradiation, Chemical engineering journal, 195 (2012) 77-90.
[24] R. Yamaguchi, S. Kurosu, M. Suzuki, Y. Kawase, Hydroxyl radical generation by zero-valent iron/Cu (ZVI/Cu) bimetallic catalyst in wastewater treatment: Heterogeneous Fenton/Fenton-like reactions by Fenton reagents formed in-situ under oxic conditions, Chemical Engineering Journal, 334 (2018) 1537-1549.
[25] G.E. Hoag, J.B. Collins, J.L. Holcomb, J.R. Hoag, M.N. Nadagouda, R.S. Varma, Degradation of bromothymol blue by 'greener'nano-scale zero-valent iron synthesized using tea polyphenols, Journal of Materials Chemistry, 19 (2009) 8671-8677.
[26] X. Peng, B. Xi, Y. Zhao, Q. Shi, X. Meng, X. Mao, Y. Jiang, Z. Ma, W. Tan, H. Liu, Effect of arsenic on the formation and adsorption property of ferric hydroxide precipitates in ZVI treatment, Environmental science & technology, 51 (2017) 10100-10108.
[27] R.D. Ludwig, D.J. Smyth, D.W. Blowes, L.E. Spink, R.T. Wilkin, D.G. Jewett, C.J. Weisener, Treatment of arsenic, heavy metals, and acidity using a mixed ZVI-compost PRB, Environmental Science & Technology, 43 (2009) 1970-1976.
[28] J. Li, Z. Shi, B. Ma, P. Zhang, X. Jiang, Z. Xiao, X. Guan, Improving the reactivity of zerovalent iron by taking advantage of its magnetic memory: implications for arsenite removal, Environmental science & technology, 49 (2015) 10581-10588.
[29] J. Li, H. Qin, X. Guan, Premagnetization for enhancing the reactivity of multiple zerovalent iron samples toward various contaminants, Environmental science & technology, 49 (2015) 14401-14408.
[30] F. He, D. Zhao, Manipulating the size and dispersibility of zerovalent iron nanoparticles by use of carboxymethyl cellulose stabilizers, Environmental Science & Technology, 41 (2007) 6216-6221.

[31] R. Hudson, G. Hamasaka, T. Osako, Y.M. Yamada, C.J. Li, Y. Uozumi, A. Moores, Highly efficient iron (0) nanoparticle-catalyzed hydrogenation in water in flow, Green Chemistry, 15 (2013) 2141-2148.
[32] Y.P. Sun, X.Q. Li, W.X. Zhang, H.P. Wang, A method for the preparation of stable dispersion of zero-valent iron nanoparticles, Colloids and Surfaces A: Physicochemical and Engineering Aspects, 308 (2007) 60-66.
[33] C.G. Hadjipanayis, M.J. Bonder, S. Balakrishnan, X. Wang, H. Mao, G.C. Hadjipanayis, Metallic iron nanoparticles for MRI contrast enhancement and local hyperthermia, Small, 4 (2008) 1925-1929.
[34] L.F. Greenlee, N.S. Rentz, ATMP-stabilized iron nanoparticles: chelator-controlled nanoparticle synthesis, Journal of Nanoparticle Research, 16 (2014) 1-16.
[35] Y.N. Vodyanitskii, Artificial permeable redox barriers for purification of soil and ground water: A review of publications, Eurasian soil science, 47 (2014) 1058-1068.
[36] J. Xu, T. Sheng, Y. Hu, S.A. Baig, X. Lv, X. Xu, Adsorption–dechlorination of 2, 4-dichlorophenol using two specified MWCNTs-stabilized Pd/Fe nanocomposites, Chemical engineering journal, 219 (2013) 162-173.
[37] M. Mangayayam, K. Dideriksen, M. Ceccato, D.J. Tobler, The Structure of Sulfidized Zero-Valent Iron by One-Pot Synthesis: Impact on Contaminant Selectivity and Long-Term Performance, Environmental science & technology, 53 (2019) 4389-4396.
[38] X. Guan, Y. Sun, H. Qin, J. Li, I.M. Lo, D. He, H. Dong, The limitations of applying zero-valent iron technology in contaminants sequestration and the corresponding countermeasures: the development in zero-valent iron technology in the last two decades (1994–2014), Water research, 75 (2015) 224-248.
[39] F. He, D. Zhao, C. Paul, Field assessment of carboxymethyl cellulose stabilized iron nanoparticles for in situ destruction of chlorinated solvents in source zones, Water Research, 44 (2010) 2360-2370.
[40] M. Cohen, N. Weisbrod, Field Scale Mobility and Transport Manipulation of Carbon-Supported Nanoscale Zerovalent Iron in Fractured Media, Environmental science & technology, 52 (2018) 7849-7858.
[41] R.L. Johnson, J.T. Nurmi, G.S. O'Brien Johnson, D. Fan, R.L. O'Brien Johnson, Z. Shi, A.J. Salter-Blanc, P.G. Tratnyek, G.V. Lowry, Field-scale transport and transformation of carboxymethylcellulose-stabilized nano zero-valent iron, Environmental science & technology, 47 (2013) 1573-1580.
[42] X. Zhao, W. Liu, Z. Cai, B. Han, T. Qian, D. Zhao, An overview of preparation and applications of stabilized zero-valent iron nanoparticles for soil and groundwater remediation, Water research, 100 (2016) 245-266.
[43] S. Kanel, R. Goswami, T. Clement, M. Barnett, D. Zhao, Two dimensional transport characteristics of surface stabilized zero-valent iron nanoparticles in porous media, Environmental Science & Technology, 42 (2007) 896-900.
[44] P. Jiemvarangkul, W.-x. Zhang, H.-L. Lien, Enhanced transport of polyelectrolyte stabilized nanoscale zero-valent iron (nZVI) in porous media, Chemical Engineering Journal, 170 (2011) 482-491.
[45] J.D. Torrey, J.P. Killgore, N.M. Bedford, L.F. Greenlee, Oxidation behavior of zero-valent iron nanoparticles in mixed matrix water purification membranes, Environmental Science: Water Research & Technology, 1 (2015) 146-152.

[46] M.S. Islam, S. Hernández, H. Wan, L. Ormsbee, D. Bhattacharyya, Role of membrane pore polymerization conditions for pH responsive behavior, catalytic metal nanoparticle synthesis, and PCB degradation, Journal of Membrane Science, 555 (2018) 348-361.
[47] V. Smuleac, R. Varma, S. Sikdar, D. Bhattacharyya, Green synthesis of Fe and Fe/Pd bimetallic nanoparticles in membranes for reductive degradation of chlorinated organics, Journal of membrane science, 379 (2011) 131-137.
[48] X. Ling, J. Li, W. Zhu, Y. Zhu, X. Sun, J. Shen, W. Han, L. Wang, Synthesis of nanoscale zero-valent iron/ordered mesoporous carbon for adsorption and synergistic reduction of nitrobenzene, Chemosphere, 87 (2012) 655-660.
[49] X. Sun, Y. Yan, J. Li, W. Han, L. Wang, SBA-15-incorporated nanoscale zero-valent iron particles for chromium (VI) removal from groundwater: mechanism, effect of pH, humic acid and sustained reactivity, Journal of hazardous materials, 266 (2014) 26-33.
[50] H. Wan, N.J. Briot, A. Saad, L. Ormsbee, D. Bhattacharyya, Pore functionalized PVDF membranes with in-situ synthesized metal nanoparticles: Material characterization, and toxic organic degradation, Journal of Membrane Science, 530 (2017) 147-157.
[51] Y. Han, C. Liu, J. Horita, W. Yan, Trichloroethene hydrodechlorination by Pd-Fe bimetallic nanoparticles: Solute-induced catalyst deactivation analyzed by carbon isotope fractionation, Applied Catalysis B: Environmental, 188 (2016) 77-86.
[52] Z. Liu, C. Gu, M. Ye, Y. Bian, Y. Cheng, F. Wang, X. Yang, Y. Song, X. Jiang, Debromination of polybrominated diphenyl ethers by attapulgite-supported Fe/Ni bimetallic nanoparticles: Influencing factors, kinetics and mechanism, Journal of hazardous materials, 298 (2015) 328-337.
[53] J. Xu, Z. Cao, H. Zhou, Z. Lou, Y. Wang, X. Xu, G.V. Lowry, Sulfur Dose and Sulfidation Time Affect Reactivity and Selectivity of Post-Sulfidized Nanoscale Zerovalent Iron, Environmental Science & Technology, 53 (2019) 13344-13352.
[54] W. Xu, Z. Li, S. Shi, J. Qi, S. Cai, Y. Yu, D.M. O'Carroll, F. He, Carboxymethyl Cellulose Stabilized and Sulfidated Nanoscale Zero-Valent Iron: Characterization and Trichloroethene Dechlorination, Applied Catalysis B: Environmental, (2019) 118303.
[55] H. Wan, M.S. Islam, N.J. Briot, M. Schnobrich, L. Pacholik, L. Ormsbee, D. Bhattacharyya, Pd/Fe nanoparticle integrated PMAA-PVDF membranes for chloro-organic remediation from synthetic and site groundwater, Journal of Membrane Science, 594 (2020) 117454.
[56] H.-L. Lien, W.-X. Zhang, Nanoscale Pd/Fe bimetallic particles: catalytic effects of palladium on hydrodechlorination, Applied Catalysis B: Environmental, 77 (2007) 110-116.
[57] T. Zhou, Y. Li, T.-T. Lim, Catalytic hydrodechlorination of chlorophenols by Pd/Fe nanoparticles: comparisons with other bimetallic systems, kinetics and mechanism, Separation and Purification Technology, 76 (2010) 206-214.
[58] J. Xu, J. Tang, S.A. Baig, X. Lv, X. Xu, Enhanced dechlorination of 2, 4-dichlorophenol by Pd/FeFe3O4 nanocomposites, Journal of hazardous materials, 244 (2013) 628-636.
[59] H. Choi, S.R. Al-Abed, S. Agarwal, D.D. Dionysiou, Synthesis of reactive nano-Fe/Pd bimetallic system-impregnated activated carbon for the simultaneous adsorption and dechlorination of PCBs, Chemistry of Materials, 20 (2008) 3649-3655.

[60] Y. Han, W. Yan, Reductive dechlorination of trichloroethene by zero-valent iron nanoparticles: reactivity enhancement through sulfidation treatment, Environmental science & technology, 50 (2016) 12992-13001.
[61] S. Bhattacharjee, S. Ghoshal, Optimal design of sulfidated nanoscale zerovalent iron for enhanced trichloroethene degradation, Environmental science & technology, 52 (2018) 11078-11086.
[62] J. Xu, Y. Wang, C. Weng, W. Bai, Y. Jiao, R. Kaegi, G.V. Lowry, Reactivity, Selectivity, and Long-term Performance of Sulfidized Nanoscale Zerovalent Iron with Different Properties, Environmental science & technology, 53 (2019) 5936-5945.
[63] J. Li, X. Zhang, M. Liu, B. Pan, W. Zhang, Z. Shi, X. Guan, Enhanced reactivity and electron selectivity of sulfidated zerovalent iron toward chromate under aerobic conditions, Environmental science & technology, 52 (2018) 2988-2997.
[64] D. Li, Z. Mao, Y. Zhong, W. Huang, Y. Wu, P.a. Peng, Reductive transformation of tetrabromobisphenol A by sulfidated nano zerovalent iron, Water research, 103 (2016) 1-9.
[65] J. Xu, Z. Cao, X. Liu, H. Zhao, X. Xiao, J. Wu, X. Xu, J.L. Zhou, Preparation of functionalized Pd/Fe-Fe3O4@ MWCNTs nanomaterials for aqueous 2, 4-dichlorophenol removal: Interactions, influence factors, and kinetics, Journal of hazardous materials, 317 (2016) 656-666.
[66] G.N. Jovanovic, J.E. Atwater, P. Žnidaršič-Plazl, I. Plazl, Dechlorination of polychlorinated phenols on bimetallic Pd/Fe catalyst in a magnetically stabilized fluidized bed, Chemical Engineering Journal, 274 (2015) 50-60.
[67] Q. Shi, H. Wang, S. Liu, L. Pang, Z. Bian, Electrocatalytic reduction-oxidation of chlorinated phenols using a nanostructured Pd-Fe modified graphene catalyst, Electrochimica Acta, 178 (2015) 92-100.
[68] X. Ma, D. He, A.M. Jones, T.D. Waite, T. An, Ligand-mediated contaminant degradation by bare and carboxymethyl cellulose-coated bimetallic palladium-zero valent iron nanoparticles in high salinity environments, Journal of Environmental Sciences, (2018).
[69] X. Wang, W. Wang, G. Lowry, X. Li, Y. Guo, T. Li, Preparation of palladized carbon nanotubes encapsulated iron composites: highly efficient dechlorination for trichloroethylene and low corrosion of nanoiron, Royal Society open science, 5 (2018) 172242.
[70] Y. Ma, Y. Wang, X. Lv, F. Meng, Q. Yang, Insight into the mode of action of Pd-doped zero-valent iron nanoparticles@ graphene (Pd/FePs@ G) toward carbon tetrachloride dechlorination reaction in aqueous solution, Applied Catalysis A: General, 560 (2018) 84-93.
[71] G.K. Parshetti, R.-a. Doong, Dechlorination of trichloroethylene by Ni/Fe nanoparticles immobilized in PEG/PVDF and PEG/nylon 66 membranes, Water research, 43 (2009) 3086-3094.
[72] X. Wang, C. Chen, H. Liu, J. Ma, Preparation and characterization of PAA/PVDF membrane-immobilized Pd/Fe nanoparticles for dechlorination of trichloroacetic acid, Water research, 42 (2008) 4656-4664.
[73] Y. Gu, I. Favier, C. Pradel, D.L. Gin, J.F. Lahitte, R.D. Noble, M. Gómez, J.C. Remigy, High catalytic efficiency of palladium nanoparticles immobilized in a polymer

membrane containing poly (ionic liquid) in Suzuki–Miyaura cross-coupling reaction, Journal of Membrane Science, 492 (2015) 331-339.
[74] J. Kim, Q. Fu, K. Xie, J.M. Scofield, S.E. Kentish, G.G. Qiao, CO 2 separation using surface-functionalized SiO 2 nanoparticles incorporated ultra-thin film composite mixed matrix membranes for post-combustion carbon capture, Journal of Membrane Science, 515 (2016) 54-62.
[75] L. Huang, S. Zhao, Z. Wang, J. Wu, J. Wang, S. Wang, In situ immobilization of silver nanoparticles for improving permeability, antifouling and anti-bacterial properties of ultrafiltration membrane, Journal of Membrane Science, 499 (2016) 269-281.
[76] C.S. Kim, S.H. Ahn, D.Y. Jang, Review: Developments in micro/nanoscale fabrication by focused ion beams, Vacuum, 86 (2012) 1014-1035.
[77] S. Reyntjens, R. Puers, A review of focused ion beam applications in microsystem technology, Journal of Micromechanics and Microengineering, 11 (2001) 287.
[78] A. Fane, Membranes for water production and wastewater reuse, Desalination, 106 (1996) 1-9.
[79] D.M. Warsinger, S. Chakraborty, E.W. Tow, M.H. Plumlee, C. Bellona, S. Loutatidou, L. Karimi, A.M. Mikelonis, A. Achilli, A. Ghassemi, A review of polymeric membranes and processes for potable water reuse, Progress in polymer science, 81 (2018) 209-237.
[80] H.B. Park, J. Kamcev, L.M. Robeson, M. Elimelech, B.D. Freeman, Maximizing the right stuff: The trade-off between membrane permeability and selectivity, Science, 356 (2017) eaab0530.
[81] B.E. Logan, M. Elimelech, Membrane-based processes for sustainable power generation using water, Nature, 488 (2012) 313.
[82] T.H. Bae, J.S. Lee, W. Qiu, W.J. Koros, C.W. Jones, S. Nair, A high-performance gas-separation membrane containing submicrometer-sized metal–organic framework crystals, Angewandte Chemie International Edition, 49 (2010) 9863-9866.
[83] Y.-x. Shen, P.O. Saboe, I.T. Sines, M. Erbakan, M. Kumar, Biomimetic membranes: A review, Journal of Membrane Science, 454 (2014) 359-381.
[84] S. Karan, Z. Jiang, A.G. Livingston, Sub–10 nm polyamide nanofilms with ultrafast solvent transport for molecular separation, Science, 348 (2015) 1347-1351.
[85] L.J. Zeman, A.L. Zydney, Microfiltration and ultrafiltration: principles and applications, CRC Press, 2017.
[86] J. Wei, C. Qiu, C.Y. Tang, R. Wang, A.G. Fane, Synthesis and characterization of flat-sheet thin film composite forward osmosis membranes, Journal of Membrane Science, 372 (2011) 292-302.
[87] M. Yu, C. Zhou, J. Liu, J.D. Hankins, J. Zheng, Luminescent gold nanoparticles with pH-dependent membrane adsorption, Journal of the American Chemical Society, 133 (2011) 11014-11017.
[88] F. Zhang, H. Zhang, C. Qu, Imidazolium functionalized polysulfone anion exchange membrane for fuel cell application, Journal of Materials Chemistry, 21 (2011) 12744-12752.
[89] G.H. Choi, D.K. Rhee, A.R. Park, M.J. Oh, S. Hong, J.J. Richardson, J. Guo, F. Caruso, P.J. Yoo, Ag nanoparticle/polydopamine-coated inverse opals as highly efficient catalytic membranes, ACS applied materials & interfaces, 8 (2016) 3250-3257.

[90] C. Hu, M.-S. Wang, C.-H. Chen, Y.-R. Chen, P.-H. Huang, K.-L. Tung, Phosphorus-doped g-C3N4 integrated photocatalytic membrane reactor for wastewater treatment, Journal of Membrane Science, (2019).
[91] X. Fang, J. Li, B. Ren, Y. Huang, D. Wang, Z. Liao, Q. Li, L. Wang, D.D. Dionysiou, Polymeric ultrafiltration membrane with in situ formed nano-silver within the inner pores for simultaneous separation and catalysis, Journal of Membrane Science, (2019).
[92] R. Ling, J. Shao, J.P. Chen, M. Reinhard, Iron catalyzed degradation of an aromatic polyamide reverse osmosis membrane by free chlorine, Journal of Membrane Science, 577 (2019) 205-211.
[93] G. Vitola, R. Mazzei, T. Poerio, E. Porzio, G. Manco, I. Perrotta, F. Militano, L. Giorno, Biocatalytic membrane reactor development for organophosphates degradation, Journal of hazardous materials, 365 (2019) 789-795.
[94] H. Zhang, J. Luo, S. Li, J.M. Woodley, Y. Wan, Can graphene oxide improve the performance of biocatalytic membrane?, Chemical Engineering Journal, 359 (2019) 982-993.
[95] X. Wang, Y. Zou, B. Meng, X. Tan, S. Wang, S. Liu, Catalytic palladium membrane reactors for one-step benzene hydroxylation to phenol, Journal of membrane science, 563 (2018) 864-872.
[96] M. Sun, I. Zucker, D.M. Davenport, X. Zhou, J. Qu, M. Elimelech, Reactive, self-cleaning ultrafiltration membrane functionalized with iron oxychloride nanocatalysts, Environmental science & technology, 52 (2018) 8674-8683.
[97] R. Molinari, C. Lavorato, P. Argurio, Recent progress of photocatalytic membrane reactors in water treatment and in synthesis of organic compounds. A review, Catalysis Today, 281 (2017) 144-164.
[98] S. Gul, Z.A. Rehan, S.A. Khan, K. Akhtar, M.A. Khan, M. Khan, M.I. Rashid, A.M. Asiri, S.B. Khan, Antibacterial PES-CA-Ag2O nanocomposite supported Cu nanoparticles membrane toward ultrafiltration, BSA rejection and reduction of nitrophenol, Journal of Molecular Liquids, 230 (2017) 616-624.
[99] J. Martinez, A. Ortiz, I. Ortiz, State-of-the-art and perspectives of the catalytic and electrocatalytic reduction of aqueous nitrates, Applied Catalysis B: Environmental, 207 (2017) 42-59.
[100] W. Qing, X. Li, S. Shao, X. Shi, J. Wang, Y. Feng, W. Zhang, W. Zhang, Polymeric catalytically active membranes for reaction-separation coupling: A review, Journal of Membrane Science, (2019).
[101] D. Bastani, N. Esmaeili, M. Asadollahi, Polymeric mixed matrix membranes containing zeolites as a filler for gas separation applications: A review, Journal of Industrial and Engineering Chemistry, 19 (2013) 375-393.
[102] N. Abdullah, R. Gohari, N. Yusof, A. Ismail, J. Juhana, W. Lau, T. Matsuura, Polysulfone/hydrous ferric oxide ultrafiltration mixed matrix membrane: preparation, characterization and its adsorptive removal of lead (II) from aqueous solution, Chemical Engineering Journal, 289 (2016) 28-37.
[103] M.K. Joshi, A.P. Tiwari, H.R. Pant, B.K. Shrestha, H.J. Kim, C.H. Park, C.S. Kim, In situ generation of cellulose nanocrystals in polycaprolactone nanofibers: effects on crystallinity, mechanical strength, biocompatibility, and biomimetic mineralization, ACS applied materials & interfaces, 7 (2015) 19672-19683.

[104] X. Li, A. Sotto, J. Li, B. Van der Bruggen, Progress and perspectives for synthesis of sustainable antifouling composite membranes containing in situ generated nanoparticles, Journal of Membrane Science, 524 (2017) 502-528.
[105] Y. Hu, Z. Lü, C. Wei, S. Yu, M. Liu, C. Gao, Separation and antifouling properties of hydrolyzed PAN hybrid membranes prepared via in-situ sol-gel SiO2 nanoparticles growth, Journal of Membrane Science, 545 (2018) 250-258.
[106] S. Hernandez, A. Saad, L. Ormsbee, D. Bhattacharyya, Nanocomposite and responsive membranes for water treatment, Emerging Membrane Technology For Sustainable Water Treatment; Hankins, NP, Singh, R., Eds, (2016) 389-431.
[107] R. Pang, X. Li, J. Li, Z. Lu, X. Sun, L. Wang, Preparation and characterization of ZrO2/PES hybrid ultrafiltration membrane with uniform ZrO2 nanoparticles, Desalination, 332 (2014) 60-66.
[108] R. Pang, J. Li, K. Wei, X. Sun, J. Shen, W. Han, L. Wang, In situ preparation of Al-containing PVDF ultrafiltration membrane via sol–gel process, Journal of colloid and interface science, 364 (2011) 373-378.
[109] J. Zhu, Y. Zhang, M. Tian, J. Liu, Fabrication of a mixed matrix membrane with in situ synthesized quaternized polyethylenimine nanoparticles for dye purification and reuse, ACS Sustainable Chemistry & Engineering, 3 (2015) 690-701.
[110] J.-H. Jiang, L.-P. Zhu, H.-T. Zhang, B.-K. Zhu, Y.-Y. Xu, Improved hydrodynamic permeability and antifouling properties of poly (vinylidene fluoride) membranes using polydopamine nanoparticles as additives, Journal of membrane science, 457 (2014) 73-81.
[111] L.Y. Ng, A.W. Mohammad, C.P. Leo, N. Hilal, Polymeric membranes incorporated with metal/metal oxide nanoparticles: a comprehensive review, Desalination, 308 (2013) 15-33.
[112] J. Kim, B. Van der Bruggen, The use of nanoparticles in polymeric and ceramic membrane structures: review of manufacturing procedures and performance improvement for water treatment, Environmental Pollution, 158 (2010) 2335-2349.
[113] K. Zodrow, L. Brunet, S. Mahendra, D. Li, A. Zhang, Q. Li, P.J. Alvarez, Polysulfone ultrafiltration membranes impregnated with silver nanoparticles show improved biofouling resistance and virus removal, Water research, 43 (2009) 715-723.
[114] M.-m. Cheng, L.-j. Huang, Y.-x. Wang, J.-g. Tang, Y. Wang, Y.-c. Zhao, G.-f. Liu, Y. Zhang, M.J. Kipper, S.R. Wickramasinghe, Reduced graphene oxide–gold nanoparticle membrane for water purification, Separation Science and Technology, 54 (2019) 1079-1085.
[115] X. Wang, M. Zhu, H. Liu, J. Ma, F. Li, Modification of Pd–Fe nanoparticles for catalytic dechlorination of 2, 4-dichlorophenol, Science of the Total Environment, 449 (2013) 157-167.
[116] N. Chitpong, S. Husson, Nanofiber ion-exchange membranes for the rapid uptake and recovery of heavy metals from water, Membranes, 6 (2016) 59.
[117] N. Chitpong, S.M. Husson, Polyacid functionalized cellulose nanofiber membranes for removal of heavy metals from impaired waters, Journal of Membrane Science, 523 (2017) 418-429.
[118] M.A. Shannon, P.W. Bohn, M. Elimelech, J.G. Georgiadis, B.J. Marinas, A.M. Mayes, Science and technology for water purification in the coming decades, Nature, 452 (2008) 301-310.

[119] J. Jiang, L. Zhu, L. Zhu, B. Zhu, Y. Xu, Surface characteristics of a self-polymerized dopamine coating deposited on hydrophobic polymer films, Langmuir, 27 (2011) 14180-14187.
[120] L. Setiawan, R. Wang, K. Li, A.G. Fane, Fabrication of novel poly (amide–imide) forward osmosis hollow fiber membranes with a positively charged nanofiltration-like selective layer, Journal of Membrane Science, 369 (2011) 196-205.
[121] N. Luo, M.J. Stewart, D.E. Hirt, S.M. Husson, D.W. Schwark, Surface modification of ethylene-co-acrylic acid copolymer films: Addition of amide groups by covalently bonded amino acid intermediates, Journal of applied polymer science, 92 (2004) 1688-1694.
[122] J. Jiang, P. Zhang, L. Zhu, B. Zhu, Y. Xu, Improving antifouling ability and hemocompatibility of poly (vinylidene fluoride) membranes by polydopamine-mediated ATRP, Journal of Materials Chemistry B, 3 (2015) 7698-7706.
[123] J. Yin, B. Deng, Polymer-matrix nanocomposite membranes for water treatment, Journal of Membrane Science, 479 (2015) 256-275.
[124] H. Bai, X. Zan, J. Juay, D.D. Sun, Hierarchical heteroarchitectures functionalized membrane for high efficient water purification, Journal of Membrane Science, 475 (2015) 245-251.
[125] Z. Xia, H. Liu, S. Wang, Z. Meng, N. Ren, Preparation and dechlorination of a poly (vinylidene difluoride)-grafted acrylic acid film immobilized with Pd/Fe bimetallic nanoparticles for monochloroacetic acid, Chemical engineering journal, 200 (2012) 214-223.
[126] Y.H. Lin, H.H. Tseng, M.Y. Wey, M.D. Lin, Characteristics, morphology, and stabilization mechanism of PAA250K-stabilized bimetal nanoparticles, Colloids and Surfaces A: Physicochemical and Engineering Aspects, 349 (2009) 137-144.
[127] K. Hu, J.M. Dickson, Modelling of the pore structure variation with pH for pore-filled pH-sensitive poly (vinylidene fluoride)–poly (acrylic acid) membranes, Journal of Membrane Science, 321 (2008) 162-171.
[128] K. Hu, J.M. Dickson, Development and characterization of poly (vinylidene fluoride)–poly (acrylic acid) pore-filled pH-sensitive membranes, Journal of Membrane Science, 301 (2007) 19-28.
[129] A. Aher, J. Papp, A. Colburn, H. Wan, E. Hatakeyama, P. Prakash, B. Weaver, D. Bhattacharyya, Naphthenic acids removal from high TDS produced water by persulfate mediated iron oxide functionalized catalytic membrane, and by nanofiltration, Chemical Engineering Journal, 327 (2017) 573-583.
[130] K.D. Grieger, A. Fjordbøge, N.B. Hartmann, E. Eriksson, P.L. Bjerg, A. Baun, Environmental benefits and risks of zero-valent iron nanoparticles (nZVI) for in situ remediation: risk mitigation or trade-off?, Journal of Contaminant Hydrology, 118 (2010) 165-183.
[131] M. Auffan, W. Achouak, J. Rose, M.-A. Roncato, C. Chanéac, D.T. Waite, A. Masion, J.C. Woicik, M.R. Wiesner, J.-Y. Bottero, Relation between the redox state of iron-based nanoparticles and their cytotoxicity toward Escherichia coli, Environmental science & technology, 42 (2008) 6730-6735.
[132] T. Phenrat, T.C. Long, G.V. Lowry, B. Veronesi, Partial oxidation ("aging") and surface modification decrease the toxicity of nanosized zerovalent iron, Environmental science & technology, 43 (2008) 195-200.

[133] Y. Gu, B. Wang, F. He, M.J. Bradley, P.G. Tratnyek, Mechanochemically sulfidated microscale zero valent iron: pathways, kinetics, mechanism, and efficiency of trichloroethylene dechlorination, Environmental science & technology, 51 (2017) 12653-12662.
[134] S.R.C. Rajajayavel, S. Ghoshal, Enhanced reductive dechlorination of trichloroethylene by sulfidated nanoscale zerovalent iron, Water research, 78 (2015) 144-153.
[135] L. Qin, I.A. Mergos, H. Verweij, Obtaining accurate cross-section images of supported polymeric and inorganic membrane structures, Journal of Membrane Science, 476 (2015) 194-199.
[136] L. Ling, X. Huang, M. Li, W.-x. Zhang, Mapping the reactions in a single zero-valent iron nanoparticle, Environmental science & technology, 51 (2017) 14293-14300.
[137] R.J. Kriek, F. Mahlamvana, Dependency on chloride concentration and 'in-sphere'oxidation of H2O for the effective TiO2-photocatalysed electron transfer from H2O to [PdCln (H2O) 4− n] 2− n (n= 0–4) in the absence of an added sacrificial reducing agent, Applied Catalysis A: General, 423 (2012) 28-33.
[138] Y. Yin, R.M. Rioux, C.K. Erdonmez, S. Hughes, G.A. Somorjai, A.P. Alivisatos, Formation of hollow nanocrystals through the nanoscale Kirkendall effect, Science, 304 (2004) 711-714.
[139] M. Burke, R. Madix, Hydrogen on Pd (100)-S: The effect of sulfur on precursor mediated adsorption and desorption, Surface Science, 237 (1990) 1-19.
[140] W. Xu, Z. Li, S. Shi, J. Qi, S. Cai, Y. Yu, D.M. O'Carroll, F. He, Carboxymethyl cellulose stabilized and sulfidated nanoscale zero-valent iron: Characterization and trichloroethene dechlorination, Applied Catalysis B: Environmental, 262 (2020) 118303.
[141] J. Oudar, Sulfur adsorption and poisoning of metallic catalysts, Catalysis Reviews—Science and Engmeering, 22 (1980) 171-195.
[142] Y. Lan, E.C. Butler, Iron-sulfide-associated products formed during reductive dechlorination of carbon tetrachloride, Environmental science & technology, 50 (2016) 5489-5497.
[143] T. Satapanajaru, P.J. Shea, S.D. Comfort, Y. Roh, Green rust and iron oxide formation influences metolachlor dechlorination during zerovalent iron treatment, Environmental science & technology, 37 (2003) 5219-5227.
[144] J. Fan, Z. Zhao, Z. Ding, J. Liu, Synthesis of different crystallographic FeOOH catalysts for peroxymonosulfate activation towards organic matter degradation, RSC advances, 8 (2018) 7269-7279.
[145] I. Obaidat, C. Nayek, K. Manna, G. Bhattacharjee, I. Al-Omari, A. Gismelseed, Investigating exchange bias and coercivity in Fe3O4–γ-Fe2O3 core–shell nanoparticles of fixed core diameter and variable shell thicknesses, Nanomaterials, 7 (2017) 415.
[146] Y. Su, A.S. Adeleye, A.A. Keller, Y. Huang, C. Dai, X. Zhou, Y. Zhang, Magnetic sulfide-modified nanoscale zerovalent iron (S-nZVI) for dissolved metal ion removal, Water research, 74 (2015) 47-57.
[147] Y. Su, A.S. Adeleye, Y. Huang, X. Zhou, A.A. Keller, Y. Zhang, Direct synthesis of novel and reactive sulfide-modified nano iron through nanoparticle seeding for improved cadmium-contaminated water treatment, Scientific reports, 6 (2016) 24358.

[148] H.Y. Jeong, Y.-S. Han, S.W. Park, K.F. Hayes, Aerobic oxidation of mackinawite (FeS) and its environmental implication for arsenic mobilization, Geochimica et Cosmochimica Acta, 74 (2010) 3182-3198.
[149] A. Schippers, W. Sand, Bacterial leaching of metal sulfides proceeds by two indirect mechanisms via thiosulfate or via polysulfides and sulfur, Appl. Environ. Microbiol., 65 (1999) 319-321.
[150] C.O. Moses, D.K. Nordstrom, J.S. Herman, A.L. Mills, Aqueous pyrite oxidation by dissolved oxygen and by ferric iron, Geochimica et Cosmochimica Acta, 51 (1987) 1561-1571.
[151] A. Chandra, A.R. Gerson, The mechanisms of pyrite oxidation and leaching: a fundamental perspective, Surface Science Reports, 65 (2010) 293-315.
[152] D.S. Han, B. Batchelor, A. Abdel-Wahab, XPS analysis of sorption of selenium (IV) and selenium (VI) to mackinawite (FeS), Environmental Progress & Sustainable Energy, 32 (2013) 84-93.
[153] C. Wu, J. Tu, W. Liu, J. Zhang, S. Chu, G. Lu, Z. Lin, Z. Dang, The double influence mechanism of pH on arsenic removal by nano zero valent iron: electrostatic interactions and the corrosion of Fe 0, Environmental Science: Nano, 4 (2017) 1544-1552.
[154] R.K. Petla, S. Vivekanandhan, M. Misra, A.K. Mohanty, N. Satyanarayana, Soybean (Glycine max) leaf extract based green synthesis of palladium nanoparticles, Journal of Biomaterials and Nanobiotechnology, 3 (2012) 14-19.
[155] X. Jin, H. Chen, Q. Yang, Y. Hu, Z. Yang, Dechlorination of Carbon Tetrachloride by Sulfide-Modified Nanoscale Zerovalent Iron, Environmental Engineering Science, 35 (2018) 560-567.
[156] J.C. Ríos-Hurtado, E.M. Múzquiz-Ramos, A. Zugasti-Cruz, D.A. Cortés-Hernández, Mechanosynthesis as a Simple Method to Obtain a Magnetic Composite (Activated Carbon/Fe3O4) for Hyperthermia Treatment, Journal of Biomaterials and Nanobiotechnology, 7 (2016) 19.
[157] X. Zhang, Y. Niu, X. Meng, Y. Li, J. Zhao, Structural evolution and characteristics of the phase transformations between α-Fe 2 O 3, Fe 3 O 4 and γ-Fe 2 O 3 nanoparticles under reducing and oxidizing atmospheres, CrystEngComm, 15 (2013) 8166-8172.
[158] L. Martinez, D. Leinen, F. Martin, M. Gabas, J. Ramos-Barrado, E. Quagliata, E. Dalchiele, Electrochemical growth of diverse iron oxide (Fe3O4, α-FeOOH, and γ-FeOOH) thin films by electrodeposition potential tuning, Journal of the Electrochemical Society, 154 (2007) D126-D133.
[159] L.F. Greenlee, J.D. Torrey, R.L. Amaro, J.M. Shaw, Kinetics of zero valent iron nanoparticle oxidation in oxygenated water, Environmental science & technology, 46 (2012) 12913-12920.
[160] M.O. Nutt, J.B. Hughes, M.S. Wong, Designing Pd-on-Au bimetallic nanoparticle catalysts for trichloroethene hydrodechlorination, Environmental science & technology, 39 (2005) 1346-1353.
[161] S. Wang, B. Yang, T. Zhang, G. Yu, S. Deng, J. Huang, Catalytic hydrodechlorination of 4-chlorophenol in an aqueous solution with Pd/Ni catalyst and formic acid, Industrial & Engineering Chemistry Research, 49 (2010) 4561-4565.
[162] B.P. Chaplin, M. Reinhard, W.F. Schneider, C. Schüth, J.R. Shapley, T.J. Strathmann, C.J. Werth, Critical review of Pd-based catalytic treatment of priority contaminants in water, Environmental science & technology, 46 (2012) 3655-3670.

[163] Y.-H. Tee, L. Bachas, D. Bhattacharyya, Degradation of trichloroethylene by iron-based bimetallic nanoparticles, The Journal of Physical Chemistry C, 113 (2009) 9454-9464.
[164] J. Su, S. Lin, Z. Chen, M. Megharaj, R. Naidu, Dechlorination of p-chlorophenol from aqueous solution using bentonite supported Fe/Pd nanoparticles: synthesis, characterization and kinetics, Desalination, 280 (2011) 167-173.
[165] M. Liu, R. Huang, C. Li, M. Che, R. Su, S. Li, J. Yu, W. Qi, Z. He, Continuous Rapid Dechlorination of p-Chlorophenol by Fe-Pd Nanoparticles Promoted by Procyanidin, Chemical Engineering Science, (2019).
[166] H. Haham, J. Grinblat, M.-T. Sougrati, L. Stievano, S. Margel, Engineering of air-stable Fe/C/Pd composite nanoparticles for environmental remediation applications, Journal of Magnetism and Magnetic Materials, 389 (2015) 82-89.
[167] W. Yan, A.A. Herzing, X.-q. Li, C.J. Kiely, W.-x. Zhang, Structural evolution of Pd-doped nanoscale zero-valent iron (nZVI) in aqueous media and implications for particle aging and reactivity, Environmental science & technology, 44 (2010) 4288-4294.
[168] S.J. Bransfield, D.M. Cwiertny, A.L. Roberts, D.H. Fairbrother, Influence of copper loading and surface coverage on the reactivity of granular iron toward 1, 1, 1-trichloroethane, Environmental science & technology, 40 (2006) 1485-1490.
[169] X. Wang, C. Chen, Y. Chang, H. Liu, Dechlorination of chlorinated methanes by Pd/Fe bimetallic nanoparticles, Journal of Hazardous Materials, 161 (2009) 815-823.
[170] G. Huang, M. Wang, Y. Hu, J. Cheng, S. Lv, K. Yang, Reductive degradation of 2, 2′, 4, 4′-tretrabromodiphenyl ether with PAC-Pd/Fe nanoparticles: effects of Pd loading, initial pH and HA, and degradation pathway, Chemical Engineering Journal, 334 (2018) 1252-1259.
[171] Y. Fang, S.R. Al-Abed, Correlation of 2-chlorobiphenyl dechlorination by Fe/Pd with iron corrosion at different pH, Environmental science & technology, 42 (2008) 6942-6948.
[172] J.-L. Chen, S.R. Al-Abed, J.A. Ryan, Z. Li, Effects of pH on dechlorination of trichloroethylene by zero-valent iron, Journal of hazardous materials, 83 (2001) 243-254.
[173] G.N. Jovanovic, P. Žnidaršič Plazl, P. Sakrittichai, K. Al-Khaldi, Dechlorination of p-chlorophenol in a microreactor with bimetallic Pd/Fe catalyst, Industrial & engineering chemistry research, 44 (2005) 5099-5106.
[174] H. Jia, C. Gu, H. Li, X. Fan, S. Li, C. Wang, Effect of groundwater geochemistry on pentachlorophenol remediation by smectite-templated nanosized Pd 0/Fe 0, Environmental Science and Pollution Research, 19 (2012) 3498-3505.
[175] Y. Fang, S.R. Al-Abed, Dechlorination kinetics of monochlorobiphenyls by Fe/Pd: Effects of solvent, temperature, and PCB concentration, Applied Catalysis B: Environmental, 78 (2008) 371-380.
[176] J. Xu, D. Bhattacharyya, Fe/Pd nanoparticle immobilization in microfiltration membrane pores: Synthesis, characterization, and application in the dechlorination of polychlorinated biphenyls, Industrial & engineering chemistry research, 46 (2007) 2348-2359.
[177] E.M. Zahran, D. Bhattacharyya, L.G. Bachas, Reactivity of Pd/Fe bimetallic nanotubes in dechlorination of coplanar polychlorinated biphenyls, Chemosphere, 91 (2013) 165-171.

[178] R. Narayanan, M.A. El-Sayed, Shape-dependent catalytic activity of platinum nanoparticles in colloidal solution, Nano letters, 4 (2004) 1343-1348.
[179] J.H. Pérez, B. López-Ruiz, E. López-Cabarcos, Synthesis and characterization of microparticles based on poly-methacrylic acid with glucose oxidase for biosensor applications, Talanta, 149 (2016) 310-318.
[180] H.-R. Lin, S.-P. Yu, C.-J. Kuo, H.-J. Kao, Y.-L. Lo, Y.-J. Lin, Pilocarpine-loaded chitosan-PAA nanosuspension for ophthalmic delivery, Journal of Biomaterials Science, Polymer Edition, 18 (2007) 205-221.
[181] M. Baburaj, C. Aravindakumar, S. Sreedhanya, A. Thomas, U.K. Aravind, Treatment of model textile effluents with PAA/CHI and PAA/PEI composite membranes, Desalination, 288 (2012) 72-79.
[182] B. Cheng, Z. Li, Q. Li, J. Ju, W. Kang, M. Naebe, Development of smart poly (vinylidene fluoride)-graft-poly (acrylic acid) tree-like nanofiber membrane for pH-responsive oil/water separation, Journal of membrane science, 534 (2017) 1-8.
[183] X.-X. Fan, R. Xie, Q. Zhao, X.-Y. Li, X.-J. Ju, W. Wang, Z. Liu, L.-Y. Chu, Dual pH-responsive smart gating membranes, Journal of Membrane Science, 555 (2018) 20-29.
[184] Y. Wang, J. Wang, Z. Yuan, H. Han, T. Li, L. Li, X. Guo, Chitosan cross-linked poly (acrylic acid) hydrogels: Drug release control and mechanism, Colloids and Surfaces B: Biointerfaces, 152 (2017) 252-259.
[185] H.H. Himstedt, H. Du, K.M. Marshall, S.R. Wickramasinghe, X. Qian, pH responsive nanofiltration membranes for sugar separations, Industrial & Engineering Chemistry Research, 52 (2013) 9259-9269.
[186] M.E. Davis, R.J. Davis, Fundamentals of chemical reaction engineering, International ed., McGraw-Hill, Boston, 2003.
[187] N.H. Chen, Process reactor design, Allyn and Bacon, Boston, 1983.
[188] D. Wu, Y. Liu, Z. Liu, L. Ma, Dechlorination of hexachloroethane in water using iron shavings and amended iron shavings: kinetics and pathways, Journal of Chemistry, 2014 (2014).
[189] R. Rodrigues, S.p. Betelu, S.f. Colombano, G. Masselot, T. Tzedakis, I. Ignatiadis, Reductive dechlorination of hexachlorobutadiene by a Pd/Fe microparticle suspension in dissolved lactic acid polymers: degradation mechanism and kinetics, Industrial & Engineering Chemistry Research, 56 (2017) 12092-12100.
[190] W.-x. Zhang, C.-B. Wang, H.-L. Lien, Treatment of chlorinated organic contaminants with nanoscale bimetallic particles, Catalysis today, 40 (1998) 387-395.
[191] S. Hernández, S. Lei, W. Rong, L. Ormsbee, D. Bhattacharyya, Functionalization of flat sheet and hollow fiber microfiltration membranes for water applications, ACS sustainable chemistry & engineering, 4 (2015) 907-918.
[192] J. Feng, T.-T. Lim, Iron-mediated reduction rates and pathways of halogenated methanes with nanoscale Pd/Fe: Analysis of linear free energy relationship, Chemosphere, 66 (2007) 1765-1774.
[193] F.N. Sayed, V. Polshettiwar, Facile and sustainable synthesis of shaped iron oxide nanoparticles: effect of iron precursor salts on the shapes of iron oxides, Scientific reports, 5 (2015) 9733.

VITA

Hongyi Wan is a chemical engineering PhD candidate specializing in water remediation using catalytic membranes (reductive/oxidative) and membrane adsorption processes. Collaborating with material engineers to develop a focused ion beam-scan electron microscope method for nanoparticle characterization at entire membrane pores. Built a pilot membrane unit in cooperation with civil engineer students and machinists. Collaborating with Arcadis U.S., Inc. for the groundwater remediation (chlorinated hydrocarbons, such as TCE) on a hazardous waste site. Six presentation awards on national conferences implies the importance of the research and communication skills.

Educations:

Aug 2014-Feb 2019 (Anticipated) PhD in Chemical Engineering University of Kentucky

Advisor: Dr. Dibakar Bhattacharyya (DB) GPA: 3.88/4.00

Aug 2010-June 2014 BS in Chemical Engineering Tianjin University, China

Awards:

Poster presentation: NAMS 2016, 2018 and 2019, ICOM 2017, NIEHS 2017

Oral presentation: AIChE 2017 (Rapid in Fire in Separation Division), KWRRI 2019

Outstanding Graduate Student Award, Department of Chemical and Material Engineering

Publications:

Wan, H., Islam, M. S., Qian, D., Ormsbee, L., & Bhattacharyya, D. (2020). Reductive Degradation of CCl4 by Sulfidized Fe and Pd-Fe Nanoparticles: Kinetics, Longevity, and Morphology Aspects. *Chemical Engineering Journal*, submitted Jan 2020.

Wan, H., Islam, M. S., Briot, N. J., Schnobrich, M., Pacholik, L., Ormsbee, L., & Bhattacharyya, D. (2019). Pd/Fe nanoparticle integrated PMAA-PVDF membranes for chloro-organic remediation from synthetic and site groundwater. *Journal of Membrane Science, 594*, 117454.

Wan, H., Briot, N. J., Saad, A., Ormsbee, L., & Bhattacharyya, D. (2017). Pore functionalized PVDF membranes with in-situ synthesized metal nanoparticles: Material characterization, and toxic organic degradation. *Journal of membrane science, 530*, 147-157.

Saad, A., Mills, R., Wan, H., Mottaleb, MA., Ormsbee, L., & Bhattacharyya, D. (2020). Thermo-responsive adsorption-desorption of perfluoroorganics from water using PNIPAm hydrogels and pore functionalized membranes. *Journal of Membrane Science, 117821*

Islam, M. S., Hernández, S., Wan, H., Ormsbee, L., & Bhattacharyya, D. (2018). Role of membrane pore polymerization conditions for pH responsive behavior, catalytic metal nanoparticle synthesis, and PCB degradation. *Journal of Membrane Science, 555*, 348-361.

Aher, A., Papp, J., Colburn, A., Wan, H., Hatakeyama, E., Prakash, P., ... & Bhattacharyya, D. (2017). Naphthenic acids removal from high TDS produced water by persulfate mediated iron oxide functionalized catalytic membrane, and by nanofiltration. *Chemical Engineering Journal, 327*, 573-583.

Selected Conference Presentations:

Wan, H., Islam, S., Ormsbee, L., and Bhattacharyya, D. Bimetallic Nanoparticles Incorporated Poly(methacrylic acid) Membranes for Water Remediation: Synthesis, Advanced Characterization and Reactive Properties. North American Membrane Society 2019 Annual Meeting, Pittsburg, PA (May 2019, Poster. Best Poster Award)

Wan, H., Islam, M. S., Briot, N., Saad, A., Ormsbee, L. and Bhattacharyya, D. Bimetallic Nanoparticles Composite Poly(acrylic acid) Membrane for Water Remediation: Synthesis, Advance Characterization and Reactive Properties. North American Membrane Society 2018 Annual Meeting, Lexington, KY (June 2018, Poster. 2nd Place Poster Award)

Wan, H.; Briot, N.; Saad, A.; Ormsbee, L. and Bhattacharyya, D. Iron/Palladium Nanoparticle Functionalized Membrane for Chlorinated Contaminates Treatment. 2017 AIChE Annual Meeting, Minneapolis, MN; Second Place, TED-Sep talk (Oct 2017, Oral. 2nd Place Oral Award)

Wan, H.; Hernandez, S.; Briot, N.; Ormsbee, L. and Bhattacharyya, D. Understanding the role of Fe/Pd nanoparticles in functionalized membrane systems for PCB degradation. Superfund Research Program Annual Meeting 2017, Philadelphia, PA; (Dec 2017, Poster. Student Poster Award Winner)

Wan, H.; Briot, N.; Saad, A.; Ormsbee, L. and Bhattacharyya, D. Pore functionalized PVDF membranes with in-situ synthesized metal nanoparticles: material characterization, and toxic organic degradation. 2017 International Congress on Membranes and Membrane Processes, San Francisco, CA; (July 2017, Poster. Student Poster Winner)

Wan, H.; Gui, M.; Ormsbee, L. and Bhattacharyya, D. Iron Nanoparticle Functionalized Membrane for PCB Degradation from Water. NAMS 26th Annual Meeting, Bellevue, WA; (May 2016, Poster. Second Place Award).